Photoswitching Kinetics of Self-Assembled Azobenzene-Alkanethiols on Gold(111)

Dissertation

zur Erlangung des Grades eines

Doktors der Naturwissenschaften (Dr. rer. nat.)

am Fachbereich Physik der Freien Universität Berlin

vorgelegt von

Thomas Moldt

Berlin 2019

Abstract

In this work the photoisomerization of the azobenzene-alkanethiol Az11 in self-assembled monolayers (SAMs) is investigated. Azobenzene is a so-called molecular switch that changes its molecular structure reversibly between the stable *trans* and the metastable *cis* conformation. Besides the thermal *cis–trans* isomerization, conversion between these two states is possible by optical excitation with light of two different wavelengths: UV light and blue light predominantly trigger *trans–cis* and *cis–trans* isomerization, respectively.

When anchoring molecular switches to a surface, its properties can be reversibly changed by external stimuli. However, the switches need to be electronically decoupled from the substrate. This can for example be achieved by self-assembly of azobenzene-alkanethiols. In the resulting SAMs significant lateral interactions occur. This is in contrast to azobenzene in solution, where intermolecular interactions can be neglected. From literature it is known that the photoisomerization in such densely-packed SAMs is hindered. By diluting the azobenzene moieties on the surface with alkanethiol "spacer" molecules a significant isomerization is observed.

By X-ray photoelectron spectroscopy (XPS) it was verified that the concentration of impurities such as atomic sulfur or unbound thiols in the SAM is lower than approximately 3 %. Using near edge X-ray absorption fine structure spectroscopy (NEXAFS) we determined the average orientation of the azobenzene moieties: they are standing predominantly upright and are oriented more and more parallel to the surface if the density of azobenzenes in the SAM is decreased. By optical differential reflectance spectroscopy (DRS) we showed that strong excitonic coupling alters the absorption behavior of azobenzene: A blue-shifted excitonic band is formed. Its shift with respect to the monomer band is a function of the average distance between the azobenzene chromophores and their relative orientation.

By examining the kinetics of the photoisomerization of a diluted Az11 SAM using NEXAFS we showed that upon illumination with UV light at least 50 % of the *trans* isomers are converted to *cis*, which is far better than in densely-packed SAMs. The efficiency of photoisomerization is in line with values reported for mixed azobenzene-alkanethiol/alkanethiol SAMs and still orders of magnitude better than for azobenzenes directly adsorbed on gold. By examining the kinetics of the photoisomerization with DRS we could show that the blue-shifted excitonic band, despite its significant intensity, does not contribute to the isomerization process. Instead, the isomerization is driven by chromophores that are not part of the aggregate, e.g., regions of disorder in between different domains of molecular arrangements.

Kurzfassung

In dieser Arbeit wurde die Photoisomerisierung des Azobenzolalkanthiols Az11 in selbstorganisierten Monolagen (SAMs) untersucht. Azobenzol ist ein sogenannter molekularer Schalter, der seine Molekülstruktur reversibel zwischen der *trans*-Grundzustandskonfiguration und der metastabilen *cis*-Konfiguration ändert. Neben der thermischen Relaxation von *cis* nach *trans* kann die Isomerisierung auch durch Licht ausgelöst werden: Mit UV-Licht bzw. blauem Licht wird jeweils überwiegend die *trans–cis*- bzw. die *cis–trans*-Isomerisierung angeregt.

Durch Verankerung solcher molekularer Schalter auf einer Oberfläche können dessen Eigenschaften durch äußere Stimuli reproduzierbar geändert werden. Allerdings müssen die Schaltermoleküle dafür elektronisch vom Substrat entkoppelt sein. Dies kann beispielsweise in SAMs aus Azobenzolalkanthiolen erreicht werden. Allerdings treten in solchen Monolagen, im Gegensatz zu in Lösung befindlichem Azobenzol, signifikante intermolekulare Wechselwirkungen auf. Diese behindern dann die Photoisomerisierung. Bei durch „Abstandshaltermoleküle" verringerter Dichte der Azobenzole ist aber auch im SAM signifikante Photoisomerisierung zu beobachten.

Mittels Röntgenphotoelektronenspektroskopie (XPS) haben wir gezeigt, dass in den von uns präparierten SAMs die Konzentration von Verunreinigungen wie etwa atomarem oder ungebundenem Schwefel kleiner als etwa 3 % ist. Die mittlere Orientierung der Azobenzole haben wir mittels Röntgen-Nahkanten-Absorptions-Spektroskopie (NEXAFS) bestimmt: die Azobenzole stehen überwiegend aufrecht und sind bei abnehmender Azobenzoldichte zunehmend flacher orientiert. Die intermolekularen Wechselwirkungen wurden mittels optischer Differenzreflektionsspektroskopie (DRS) untersucht: Es wird ein Exzitonenband, das bezüglich der Absorptionsbande des Einzelmoleküls zu kürzeren Wellenlängen verschoben ist, beobachtet. Die spektrale Verschiebung ist abhängig vom mittleren Abstand der Azobenzol-Chromophore und ihrer Orientierung zueinander.

Wir haben die Photoisomerisierungskinetik von SAMs mit reduzierter Chromophordichte mittels NEXAFS und DRS untersucht. Unter UV-Licht werden mindestens 50 % der *trans*-Isomere zu *cis* umgesetzt, signifikant mehr als in dichtgepackten SAMs. Die Effizienz des Schaltprozesses ist vergleichbar mit der von verwandten Systemen und um Größenordnungen besser als bei direkt auf der Oberfläche adsorbiertem Azobenzol. Das blauverschobene Exzitonenband trägt trotz seiner hohen Intensität nicht zum Isomerisierungsprozess bei. Stattdessen wird die Isomerisierung durch Anregung von *trans*-Isomeren, die sich an Domänengrenzen oder anderen Fehlstellen befinden, getrieben.

Contents

Chapter 1

Introduction

There is an ever ongoing trend of miniaturization in the semiconductor industry in order to fit more and more transistors onto a chip. A smaller device size is not only a desirable goal in itself from the user's point of view but also allows to operate the electronics at lower voltages and currents [1], which results in higher efficiency. However, this top-down-approach is going to reach limits when aiming for actual nanometer-sized devices [2].

Therefore, so-called molecular switches and machines are an active field of research [5, 6]. Such molecules are nanometer-sized and modern chemistry can synthesize a huge variety of compounds for various possible applications [5]. Molecular switches in particular are molecules that change their structure reversibly by external stimuli such as light, electric energy, or chemical energy [4]. Light-responsive molecular switches are attractive in particular because light allows a clean, quick and remote operation without the need for direct contact to the material [4]. This may pave the way into the field of molecular electronics, i.e., the assembly of molecular switches into logic gates [2].

If molecular switches are brought onto the surface of a material, surface properties such as polarity and chemical reactivity can be changed reversibly [7]. This is exemplified in an experiment where a surface was functionalized with azobenzene, a light-sensitive molecular switch. By illumination with light, the polarity of the surface can be gradually changed, which allows to move an
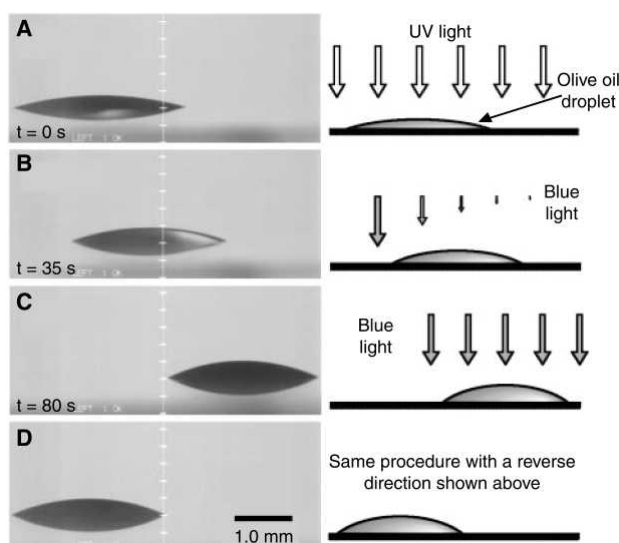
Figure 1.1: Light-driven motion of an olive-oil droplet on a silica plate covered with a monolayer of photoresponsive molecular switches. Illumination with light triggers a conformational change of the molecule, which changes the polarity of the surface. Taken from [3].
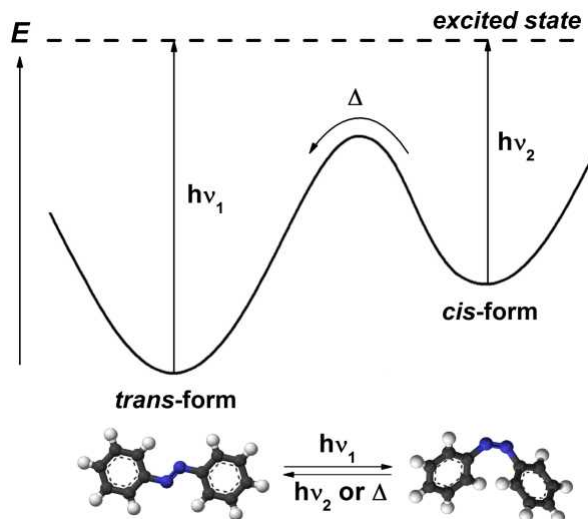
9

Figure 1.2: Schematic of the isomerization processes in azobenzene. Taken from [4].

oil droplet across the surface (see Fig. 1.1).

Azobenzene represents the most commonly used and investigated molecular switch [4, 8–10]. It is a molecule that exists in two conformations, the stable *trans* state and the metastable *cis* state (see Fig. 1.2). Conversion between these two conformations can be driven by optical excitation: whereas light of energy $h\nu_1$ excites preferably the *trans* isomer, which predominantly drives isomerization to the *cis* isomer, the opposite process can be driven by an optical excitation of the *cis* isomer using light of energy $h\nu_2$, and by thermal isomerization.

In the earliest attempts to functionalize surfaces with azobenzene, the molecule was evaporated directly onto a metal surface, however it turned out that the photoisomerization is strongly quenched due to interaction with the substrate [11, 12]. Therefore, some decoupling needs to be provided between the switch and the surface. One attempt was to separate the flat-lying azobenzene from the substrate with bulky endgroups, however, the photoisomerization efficiency was orders of magnitude less than azobenzene in solution [13].

A different approach to accomplish distance between the chromophore and the substrate is molecular self-assembly. Self-assembled monolayers (SAMs) are ordered 2D arrangements of molecules on a solid surface [14, 15]. The azobenzene moieties are oriented predominantly upright and electronically decoupled from the surface. On noble metal surfaces azobenzene-bearing SAMs can for example be fabricated using azobenzene-functionalized alkyl chains [10] or biphenyl-azo-biphenyls [16, 17] with a thiol (-SH) head group, which covalently binds to the surface.

Whereas SAMs of the biphenyl-azo-biphenyl type show pronounced photo-isomerization [16, 17], the isomerization is inhibited in azobenzene-alkanethiolate SAMs [18, 19]. The literature commonly attributes this to a lack of free volume for the azobenzene to isomerize [10, 18]. This is illustrated in Fig. 1.3a. Additionally, pronounced excitonic coupling between the chromophores is observed: The excited states of the molecule are delocalized across the surface. Instead of a single excited state an exciton band is formed, with its width
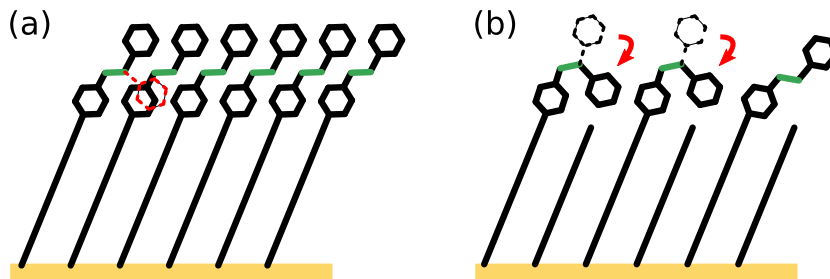
Figure 1.3: Schematic of SAMs of azobenzene-alkanethiols on gold. (a) Isomerization is inhibited in a densely-packed SAM because there is too little space between the chromophores. (b) Isomerization can occur in SAMs with reduced density of chromophores.

depending on the distance between the chromophores. This effect may also hinder the isomerization [18]. To overcome this problem, the chromophore–chromophore distance needs to be increased. This can for example be accomplished by introducing additional "spacer" molecules into the SAM (Fig. 1.3b). One way to achieve this is to prepare SAMs from molecules consisting of an azobenzene-terminated and an unfunctionalized alkanethiol counterpart. This allows to form a SAM with a 50 % dilution of azobenzene [20]. The density of chromophores on the surface can be adjusted freely by preparing SAMs from a mixture of two different thiols, an azobenzene-terminated thiol and a simple alkanethiol [10]. The photoisomerization in such SAMs was demonstrated several times, e.g., [21–23].

In the present work we studied how various properties of the SAM change with the chromophore density: We examined the chemical composition of the SAMs and the average orientation of the chromophores with respect to the surface. The orientation and the density of chromophores is interconnected with the optical properties: The absorption profile of the SAM in the UV/vis range is very different from the absorption spectrum of the single azobenzene-containing molecule due to the aforementioned excitonic coupling. The S_2 transition, which is crucial for the *trans–cis* isomerization, changes into an excitonic band, with its width changing with the chromophore density. We could show that the ability to photoisomerize increases with decreasing chromophore density. By examining the kinetics of the isomerization we determined the efficiency of photoisomerization and we studied the influence of the environment and the excitation wavelength on the isomerization.

This thesis is organized as follows: In Chap. 2, an introduction to azobenzene, to the method of molecular self-assembly and, the optical properties of azobenzene-containing SAMs is given. In Chap. 3 the experimental methods used in this work are introduced. Chap. 4, 5, and 6 present experimental findings on the chemical composition as well as the structural and optical properties of SAMs. Chap. 7 finally examines the photoisomerization and thermal isomerization of azobenzene in SAMs. The results of this thesis are summarized in Chap. 8. Details on methods and materials used in this work are given in Chap. 9.

Chapter 2

Azobenzene in Self-Assembled Monolayers

Azobenzene is one of the most widely studied molecular switches [24]. A molecular switch is a molecule that isomerizes reversibly between two conformations upon excitation by external stimuli such as light, electric potentials, or pH value [4]. In azobenzene as photoactive molecular switch the conversion between the two conformations is triggered by light of two different wavelengths.

Many applications of molecular switches require to anchor them onto a surface [7]. Molecular self-assembly is a relatively simple method to achieve this goal. With specially tailored molecules it is possible to fabricate a well-ordered molecular film of exactly one monolayer. Such molecular layers are called self-assembled monolayers (SAMs) [14].

We examine azobenzene-containing SAMs, therefore we are in particular interested in their optical properties. The optical properties of molecular layers can be described on the microscopic level and on the macroscopic level. On the microscopic level the optical properties of molecular layers are governed by the optical transition dipole moments (TDMs) of the molecules. In close-packed systems such as SAMs the TDMs interact with each other, which can lead to spectral shifts or even the splitting of absorption lines. On the macroscopic level, the properties of molecular layers can be described in terms of the Fresnel equations, which determine the reflection and transmission of electromagnetic waves at interfaces, and in terms of the complex dielectric function $\epsilon(\omega)$, which governs the dispersion and the absorption of light with frequency ω in a medium.

2.1 Azobenzene as a Molecular Switch

2.1.1 The Two Conformers of Azobenzene

Molecular Structure Azobenzene is an organic molecule that exists in two different conformations: the thermodynamically stable *trans* (E) form and the metastable *cis* (Z) form (see Fig. 2.1). In the *trans* form the phenyl rings are on opposite sides of the azo (N=N) group and the molecule is planar. In the *cis* form the phenyl rings are on the same side of the azo group and the phenyl rings are twisted against each other, i.e., *cis*-azobenzene is not planar.
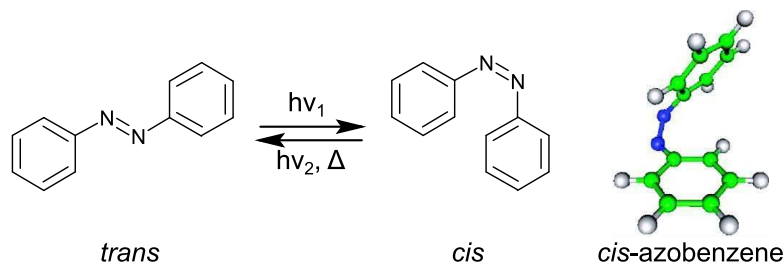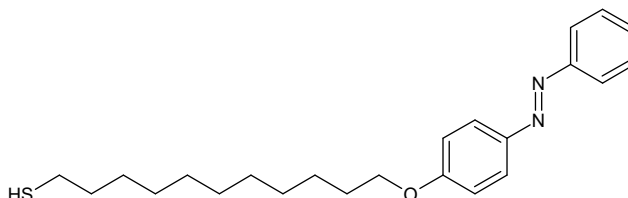
13

Figure 2.1: *trans* and *cis* isomers of azobenzene. Image of 3D structure taken from [25].

Figure 2.2: Chemical structure of the azobenzene derivative 11-(4-(phenyldiazenyl)-phenoxy)undecane-1-thiol (Az11) used in this work.

Electronic Properties and Absorbance Spectra Azobenzenes exhibit three absorption peaks in the UV/vis spectral range. Assignments of these peaks to optical transitions were made according to [26, 27]. The absorbance spectra will be described using the azobenzene derivative Az11 (see Fig. 2.2) used in this work. Spectra of both the *trans* and *cis* isomer are shown in Fig 2.3. *trans*-Az11 is characterized by the following absorption peaks: First, at about 450 nm the very weak S_1 band is observed, which is assigned to the $n\pi^\star$ excitation. It is forbidden in the inversion-symmetric *trans* form of azobenzene and only weakly allowed due to molecular vibrations [28]. In *trans*-Az11 the S_1 band is more intense because of the asymmetrical substitution. Second, we observe the very intense S_2 band at about 350 nm. It is assigned to the $\pi\pi^\star$ transition. Third, the S_3 band, assigned to higher $\pi\pi^\star$ excitations. Compared with *trans*-Az11, *cis*-Az11 exhibits differences in all three absorption bands: The intensity of the S_1 band is much higher since the inversion symmetry is broken. The S_2 band is much weaker than in *trans*-Az11 and shifted to shorter wavelengths. The S_3 band has approximately the same intensity in the *trans* and *cis* isomer but in the *cis* conformation the band is slightly shifted to longer wavelengths.

Photoisomerization Aside from the thermal isomerization from the meta-stable *cis* to the *trans* ground state, conversion between the two isomers is also possible by optical excitation. This process is then called photoisomerization. Figure 2.4 shows photoisomerization experiments with UV light (365 nm) and blue light (455 nm). If a sample of *trans*-Az11 in solution is illuminated with UV light until no change in the spectrum is observed any more, a photostationary state (PSS), which contains predominantly, but not exclusively, *cis* isomers, is obtained. Thus, the spectrum of the 365 nm-PSS is distinct from the spectrum of the pure *cis* isomer. A full conversion is not possible because for any excitation wavelength not only the *trans* but also the *cis* isomer is excited and for both excited isomers there is a certain probability of isomerization to the other respective isomer. For illumination with 365 nm light the conversion to the *cis* isomer is almost complete since its absorbance is very
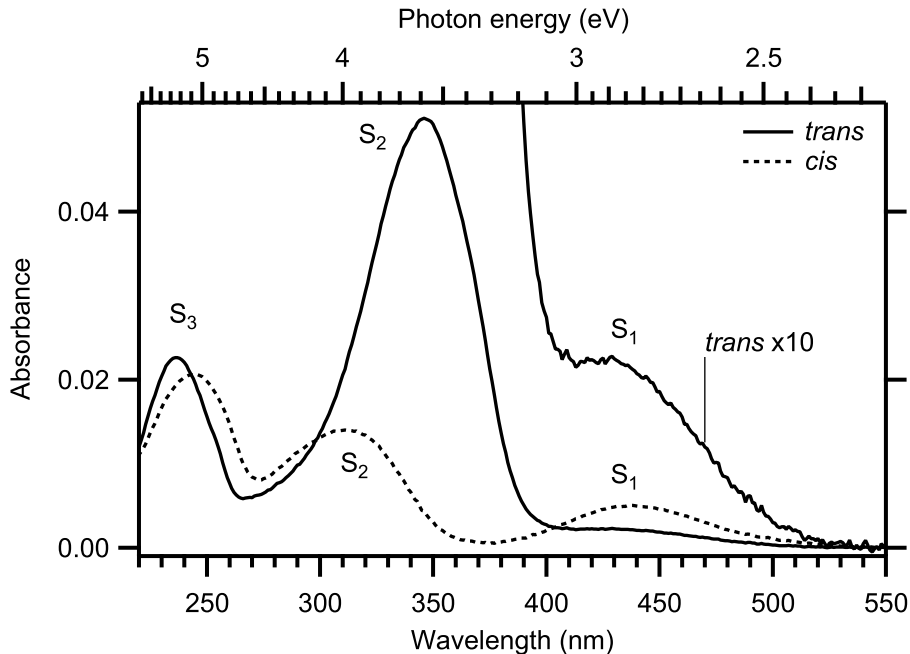
Figure 2.3: Absorbance spectra of the *trans* and *cis* isomer of the azobenzene derivative Az11.

marginal at this wavelength. A pure sample of *cis* isomers can be obtained by separating the *cis* isomer chromatographically (see for example [29, Sec. 7.5]). For this work the spectrum of the *cis* isomer was estimated as described in Sec. A.1.2. Analogously to the illumination with UV light, a PSS is also observed for illumination with blue light (455 nm). The PSS comprises about 75 % *trans* isomers (see Sec. 7.1.1). A full conversion to *trans* is only observed by thermal isomerization.

The efficiency of photoisomerization is described by two quantities: First, the absorption cross-section σ^{abs} of the respective isomer at the wavelength of illumination, and second, the photoisomerization quantum-yield Φ. The absorption cross-section σ^{abs} is a measure for the probability of absorbing an incident photon of certain wavelength, and the photoisomerization quantum-yield is the probability that isomerization occurs after optical excitation of the molecule. The quantity $\sigma^{\mathrm{ph}} = \sigma^{\mathrm{abs}}\Phi$ is then called the *photoisomerization cross-section* (details can be found in Sec. 2.1.2).

Isomerization Mechanisms The isomerization of azobenzene proceeds on the order of picoseconds [9], which is the timescale of molecular vibrations. Two main pathways are proposed: torsion and inversion (exemplarily shown for *cis–trans* isomerization in Fig. 2.5). In the case of torsion the two phenyl rings rotate against each other around the N=N bond, with the CNNC dihedral angle changing from about 0° (*cis*) to about 180° (*trans*). In the case of inversion one of the phenyl rings rotates in-plane, increasing the NNC angle from about 120° (*cis*) to about 240° (*trans*).

A scheme of the potential energy surfaces of the S_0, S_1, and S_2 states along the inversion and torsion pathways is shown in Fig. 2.6. The ground state S_0 of the *cis* form is higher in energy than the ground state of the *trans* form by about 0.6 eV, with an energy barrier between the two isomers in both the
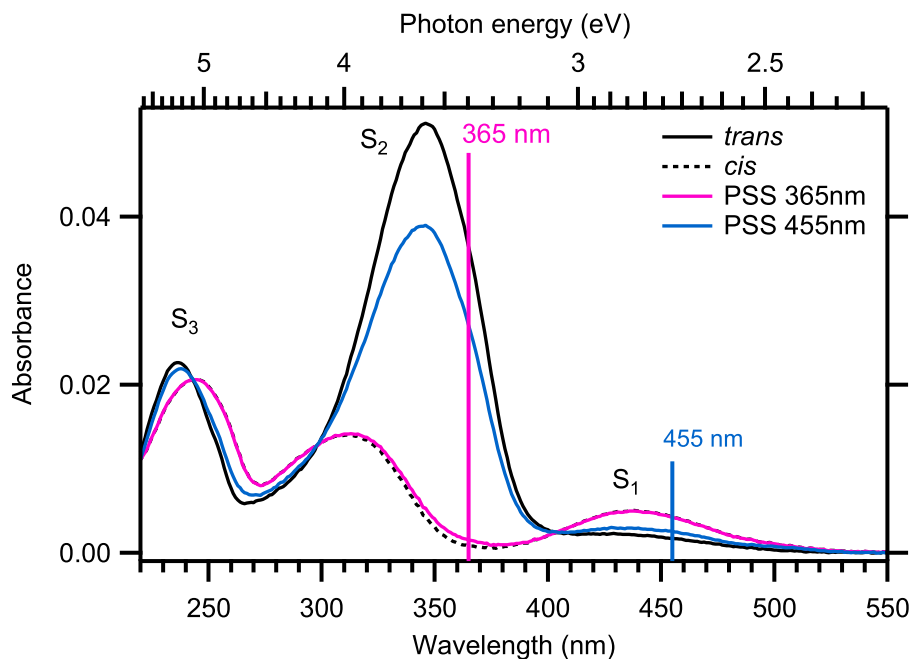
Figure 2.4: Absorbance spectra of Az11 in the photostationary states (PSSs) for illumination with UV light (365 nm) and blue light (455 nm) in comparison with the spectra of the pure isomers.
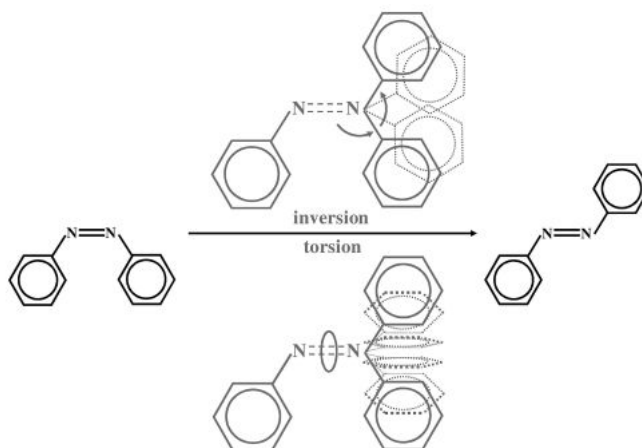
Figure 2.5: The torsion and inversion pathways in azo-benzene. Taken from [27].

inversion and torsion pathways. Therefore, there is some probability for the *cis* isomer to relax to the *trans* isomer thermally. The barrier in the inversion pathway is lower, which indicates that inversion is the preferred pathway for thermal isomerization. Experimentally, an activation energy of about 1 eV has been found [31, 32].

Most literature finds that the photoisomerization of both isomers mainly proceeds along the torsion coordinate, but inversion or other pathways have been proposed, too [9].

2.1.2 Isomerization Kinetics

After summarizing the properties of a single azobenzene molecule we now derive the isomerization kinetics of azobenzene in first order, i.e., how the number of *trans* and *cis* isomers changes in time in an ensemble of noninteracting mole-
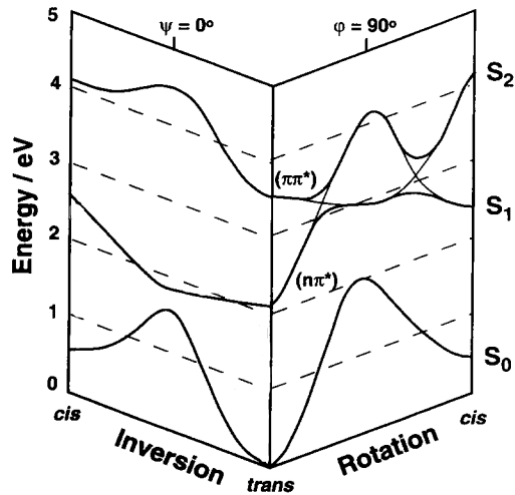
Figure 2.6: Scheme of the potential energy surfaces of both azobenzene isomers along the inversion and torsion (rotation) pathways. Taken from [30].

cules with the assumption of no interaction between the molecules and a linear optical response.

Differential Equation We consider the equilibrium reaction between the *trans* and *cis* isomer of azobenzene with a *trans–cis* isomerization rate k_t and a *cis–trans* isomerization rate k_c:

$$\text{trans} \underset{k_c}{\overset{k_t}{\rightleftharpoons}} \text{cis}$$
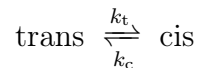
We assume the total number of molecules N,

$$N = N_c + N_t, \tag{2.1}$$

to be constant, whereas N_c and N_t are the numbers of *cis* and *trans* molecules, respectively. We then define the *mole fractions* of *cis* and *trans* molecules as a function of time t as

$$\chi_c(t) = \frac{N_c(t)}{N} \quad \text{and} \quad \chi_t(t) = \frac{N_t(t)}{N}, \tag{2.2}$$

respectively. From (2.1) it follows that $\chi_c(t) + \chi_t(t) = 1$.

We assume first-order kinetics, i.e., the change in the mole fraction of an isomer is proportional to the mole fraction itself. The differential equation in $\chi_c(t)$ is then:

$$\begin{aligned} \frac{d\chi_c}{dt} &= -k_c\,\chi_c(t) + k_t\,\chi_t(t) \\ &= -k_c\,\chi_c(t) + k_t\,[1 - \chi_c(t)] \\ &= -\,(k_c + k_t)\,\chi_c(t) + k_t \end{aligned} \tag{2.3}$$

Photoexcitation drives both *trans–cis* and *cis–trans* isomerization. Also, since the *cis* state is higher in energy than the *trans* state (see Fig. 2.6), thermal *cis–trans* isomerization needs to be considered. Therefore, the rate constant for *trans–cis* isomerization consists solely of the *photon-induced* rate constant k_t^{ph}, whereas the rate constant for the reverse reaction consists of a photon-induced

rate constant $k_{\mathrm{c}}^{\mathrm{ph}}$ and the temperature-dependent *the*rmal isomerization rate-constant $k_{\mathrm{c}}^{\mathrm{th}}$:

$$k_{\mathrm{t}} = k_{\mathrm{t}}^{\mathrm{ph}} \tag{2.4}$$

$$k_{\mathrm{c}} = k_{\mathrm{c}}^{\mathrm{ph}} + k_{\mathrm{c}}^{\mathrm{th}} \tag{2.5}$$

Thus, the differential equation (2.3) becomes

$$\frac{\mathrm{d}\chi_{\mathrm{c}}}{\mathrm{d}t} = -\tilde{k}\,\chi_{\mathrm{c}}(t) + k_{\mathrm{t}}^{\mathrm{ph}}, \tag{2.6}$$

with the effective rate constant

$$\tilde{k} = k_{\mathrm{c}}^{\mathrm{ph}} + k_{\mathrm{c}}^{\mathrm{th}} + k_{\mathrm{t}}^{\mathrm{ph}} \tag{2.7}$$

The inhomogeneous differential equation (2.6) can be solved by finding the general solution to the homogeneous equation and then using a *variation of constants* ansatz to find a solution to the inhomogeneous differential equation. The general solution of the homogeneous differential equation (second summand set to zero) is

$$\chi_{\mathrm{c}}^{\mathrm{H}}(t) = A\,e^{-\tilde{k}t}, \tag{2.8}$$

with a free constant A. For the inhomogeneous equation we make a variation of constants ansatz:

$$\chi_{\mathrm{c}}(t) = A(t)\,e^{-\tilde{k}t} \tag{2.9}$$

When applying this ansatz into (2.6) and integrating the resulting equation we obtain the following expression for $A(t)$:

$$A(t) = \frac{k_{\mathrm{t}}^{\mathrm{ph}}}{\tilde{k}}\,e^{\tilde{k}t} + C, \tag{2.10}$$

with an integration constant C. By applying this equation into (2.9) we obtain

$$\chi_{\mathrm{c}}(t) = \frac{k_{\mathrm{t}}^{\mathrm{ph}}}{\tilde{k}} + Ce^{-\tilde{k}t} \tag{2.11}$$

By using the initial condition $\chi_{\mathrm{c}}(0) \equiv \chi_{\mathrm{c},0}$ to determine C, we finally obtain the following result:

$$\chi_{\mathrm{c}}(t) = \frac{k_{\mathrm{t}}^{\mathrm{ph}}}{\tilde{k}} + \left(\chi_{\mathrm{c},0} - \frac{k_{\mathrm{t}}^{\mathrm{ph}}}{\tilde{k}}\right)e^{-\tilde{k}t} \tag{2.12}$$

This solution to the differential equation (2.6) is an exponential function with an effective rate constant $\tilde{k} = k_{\mathrm{c}}^{\mathrm{ph}} + k_{\mathrm{c}}^{\mathrm{th}} + k_{\mathrm{t}}^{\mathrm{ph}}$, an amplitude $\chi_{\mathrm{c},0} - k_{\mathrm{t}}^{\mathrm{ph}}/\tilde{k}$, and an offset $k_{\mathrm{t}}^{\mathrm{ph}}/\tilde{k}$. For $t \to \infty$ the photostationary state (PSS) is reached:

$$\chi_{\mathrm{c,PSS}} \equiv \lim_{t\to\infty} \chi_{\mathrm{c}}(t) = \frac{k_{\mathrm{t}}^{\mathrm{ph}}}{\tilde{k}} \tag{2.13}$$

We find that the PSS is independent from the initial condition $\chi_{\mathrm{c},0}$, i.e., when performing a photoisomerization experiment the same PSS should be observed regardless of the number of *trans* and *cis* isomers at $t = 0$.

Isomerization in the Dark   In the dark, when k_t^{ph} and k_c^{ph} are zero, (2.12) reduces to

$$\chi_c^{dark}(t) = \chi_{c,0}\, e^{-k_c^{th}t}.\tag{2.14}$$

As expected, the fraction of *cis* molecules decreases exponentially in time, with the thermal *cis–trans* isomerization rate-constant k_c^{th}. For $t \to \infty$ the number of *cis* isomers approaches zero. This is equivalent to saying that the *cis* isomer is metastable.

Photoisomerization Cross-Sections   In the limit of linear optics, the rate constant for photoisomerization in either direction is proportional to the incident photon flux J: $k^{ph} = \sigma^{ph} J$. The photoisomerization cross-section σ^{ph} is a measure for the probability of an isomerization process to occur due to an incoming photon. The *trans–cis* isomerization cross-section σ_t^{ph} and the *cis–trans* isomerization cross-section σ_c^{ph} are then defined by

$$\sigma_t^{ph} = \frac{k_t^{ph}}{J}; \quad \sigma_c^{ph} = \frac{k_c^{ph}}{J}\tag{2.15}$$

The isomerization rate-constants k_t^{ph} and k_c^{ph} often cannot be determined directly, but the calculation is possible if the effective rate constant $\tilde{k}$ and the fraction $\chi_{c,PSS}$ of *cis* isomers are known. By rearranging (2.13) we obtain:

$$k_t^{ph} = \tilde{k}\, \chi_{c,PSS}\tag{2.16}$$

In order to obtain an expression for k_c^{ph}, we rearrange (2.7):

$$k_c^{ph} = \tilde{k} - k_c^{th} - k_t^{ph} \overset{(2.16)}{=} \tilde{k}\,(1 - \chi_{c,PSS}) - k_c^{th} = \tilde{k}\,\chi_{t,PSS} - k_c^{th}\tag{2.17}$$

In order to determine the photoisomerization rate-constant k_c^{ph} of the *cis* isomer, the thermal isomerization rate constant k_c^{th} needs to be known as well. Using (2.16) and (2.17), the cross-sections (2.15) can be written as

$$\sigma_t^{ph} = \frac{\tilde{k}\,\chi_{c,PSS}}{J}\tag{2.18}$$

$$\sigma_c^{ph} = \frac{\tilde{k}\,(1 - \chi_{c,PSS}) - k_c^{th}}{J}.\tag{2.19}$$

Effective Photoisomerization Cross-Section   If the isomerization rate-constants k_t^{ph} and k_c^{ph} cannot be determined, the effective isomerization cross-section

$$\tilde{\sigma} = \frac{\tilde{k}}{J}\tag{2.20}$$

is often calculated instead. It only characterizes how fast the system approaches the PSS, regardless which processes contribute. The effective isomerization cross-section depends on the experimental conditions, i.e., photon flux and sample temperature, as it contains both flux-dependent photoisomerization and temperature-dependent thermal isomerization. In particular, $\tilde{\sigma}$ becomes meaningless if the thermal isomerization rate-constant k_c^{th} is on the same order of magnitude as or even bigger than the two photoisomerization rate-constants k_t^{ph} and k_c^{ph}.

If the thermal isomerization rate-constant $k_{\mathrm{c}}^{\mathrm{th}}$ is known, the effective isomerization cross-section (2.20) can be corrected for the thermal isomerization:

$$\tilde{\sigma}^{\text{no therm.}} = \frac{\tilde{k} - k_{\mathrm{c}}^{\mathrm{th}}}{J} \overset{(2.7)}{=} \frac{k_{\mathrm{t}}^{\mathrm{ph}} + k_{\mathrm{c}}^{\mathrm{ph}}}{J} \overset{(2.15)}{=} \sigma_{\mathrm{t}}^{\mathrm{ph}} + \sigma_{\mathrm{c}}^{\mathrm{ph}}. \tag{2.21}$$

$\tilde{\sigma}^{\text{no therm.}}$ is then independent from photon flux.

Using (2.15) and (2.20) we can also derive another expression for the fraction of cis isomers in a PSS (Eq. 2.13):

$$\chi_{\mathrm{c,PSS}} = \frac{k_{\mathrm{t}}^{\mathrm{ph}}}{\tilde{k}} = \frac{\sigma_{\mathrm{t}}^{\mathrm{ph}}}{\tilde{\sigma}} \tag{2.22}$$

Or, if the thermal isomerization can be neglected:

$$\chi_{\mathrm{c,PSS}}^{\text{no therm.}} = \frac{\sigma_{\mathrm{t}}^{\mathrm{ph}}}{\sigma_{\mathrm{t}}^{\mathrm{ph}} + \sigma_{\mathrm{c}}^{\mathrm{ph}}}. \tag{2.23}$$

Photoisomerization Quantum Yields   The photoisomerization quantum-yield Φ is the probability for a chromophore to isomerize after absorption of a photon. It is the ratio of the photoisomerization cross-section σ^{ph} (2.15) and the absorption cross-section σ^{abs} (3.13):

$$\Phi_{\mathrm{t}} = \frac{\sigma_{\mathrm{t}}^{\mathrm{ph}}}{\sigma_{\mathrm{t}}^{\mathrm{abs}}}; \quad \Phi_{\mathrm{c}} = \frac{\sigma_{\mathrm{c}}^{\mathrm{ph}}}{\sigma_{\mathrm{c}}^{\mathrm{abs}}} \tag{2.24}$$

For non-interacting molecules a photoisomerization quantum-yield Φ can be 1 at most because a $\Phi > 1$ would mean that the excitation of one molecule would lead to the isomerization of more than one molecule.

2.2   Self-Assembled Monolayers (SAMs)

Self-assembly is the spontaneous formation of nanometer-sized units from molecular building blocks. Self-assembled monolayers (SAMs) in particular are ordered arrangements of molecules on a solid surface [14, 15]. The key properties of SAMs are: (1) The whole surface will be covered and exactly one monolayer is formed. (2) In the self-assembly process both the binding of the molecule to the surface and intermolecular forces are decisive for what surface structure is established. (3) The molecules that form the monolayer typically consist of three parts (see Fig. 2.7): A head group that binds to the substrate, an alkyl chain that provides intermolecular forces leading to well-ordered monolayers, and a functional terminal group that may alter various surface properties. In this work we examine alkanethiol SAMs on gold. Here, a thiol (-SH) head group binds covalently to a gold substrate, forming the gold thiolate bond [15, 33].

Mechanism of SAM Formation   The formation of thiol SAMs on gold is taking place in two steps: first, adsorption of the molecules on the surface, and second, a crystallization process. The binding to the surface is driven by the
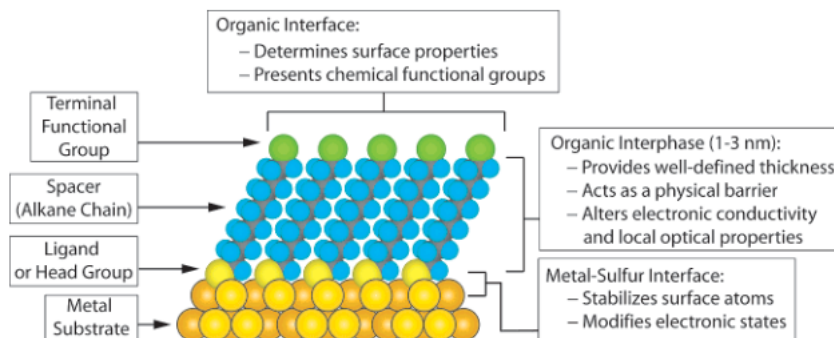
Figure 2.7: Scheme of an ideal, single-crystalline SAM of alkanethiolates supported on a gold (111) surface. The anatomy and characteristics of the SAM are highlighted. Taken from [33].

chemical reaction of the sulfur head group with the gold surface, forming the strong gold thiolate bond ($44\,\mathrm{kcal\,mol^{-1}} \equiv 1.9\,\mathrm{eV}$) [34]:

$$\mathrm{Au} + \mathrm{HS(CH_2)_n X} \quad \xrightarrow{-1/2\,\mathrm{H_2}} \quad \mathrm{Au - S(CH_2)_n X} \qquad (2.25)$$
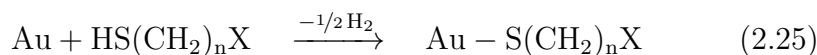
Disulfides, which are often present in the adsorption solution due to oxidation, lead to the same gold thiolate species as thiols:

$$\mathrm{Au} + {}^{1}\!/_{2}\,\mathrm{X(CH_2)_n SS(CH_2)_n X} \quad \longrightarrow \quad \mathrm{Au - S(CH_2)_n X} \qquad (2.26)$$
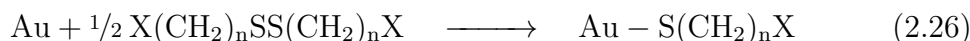
In the second step the order in the molecular layer increases on a timescale of a day by diffusion or exchange. Atomic force microscopy (AFM) and scanning tunneling microscopy (STM) reveals that such SAMs can exhibit a very high degree of order with domain sizes on the order of $100\,\mathrm{nm^2}$ [15].

The Sulfur–Gold Bond An important criterion for the quality of the SAM is that all sulfur atoms are in fact covalently bound to the surface, i.e., all sulfur is present as thiolate. Residual unbound thiol or disulfide would be indicative of problems with the rinsing of the sample after immersion in the adsorption solution. Other possible byproducts are atomic sulfur or sulfur in other oxidative states. The different species of sulfur can be identified and quantified with X-ray photoelectron spectroscopy (XPS). Such measurements were performed for selected samples and indeed we could show that with a detection sensitivity of approximately $3\,\%$ only the thiolate species was present (see Sec. 4.2).

Preparation of SAMs Thiol SAMs on gold are usually prepared by immersing the gold substrate into a dilute solution of the thiols (concentration of $\approx 1\,\mathrm{mM} = 10^{-3}\,\mathrm{mol\,l^{-1}}$, typically the solvent is ethanol) for 12-18 hours [33]. Gold with the (111) surface, which exhibits the well-known herringbone reconstruction [35, 36], is often used as substrate, either as gold single crystal or as a gold film on silicon, glass or mica [14, 33]. Gold on mica forms the (111) face with large terraces on the order of $100\,\mathrm{nm}$ in width and is therefore considered a "pseudo-single crystal" [33].

Single-Component Azobenzene-Containing SAMs   It has been shown that the photoisomerization of azobenzenes physisorbed on gold is strongly quenched [11, 12]. Therefore, the azobenzene moiety needs to be sufficiently distanced from the surface. One approach is the use of alkyl chains between the sulfur head group and the azobenzene moiety [18, 37], which is also used in this work. Atomic force microscopy (AFM) and scanning tunneling microscopy (STM) on SAMs of such molecules revealed a densely packed crystalline structure. Specifically, herringbone structures with two differently oriented molecules per unit cell were found [38, 39].

However, in single-component azobenzene-alkanethiol SAMs no or no significant photoisomerization is observed [18, 19]. This may either be due to steric hindrance, i.e., not enough space for photoisomerization, or due to excitonic coupling. Excitonic coupling is the effect that in molecular crystals the optical excitation that should drive the photoisomerization, is in fact delocalized across the SAM and cannot be efficiently localized on one molecule. This effect is explained in more detail in Sec. 2.3.1. Both steric hindrance and excitonic coupling are effects that increase with increased packing density. Therefore, disentangling these two effects experimentally seems difficult. Molecular dynamics simulations of an azobenzene dimer in a close-packed environment indicate that at least in this model system the inhibited *trans–cis* photoisomerization after $\pi\pi^\star$ excitation is rather due to steric hindrance than excitonic coupling [40].

Mixed SAMs   Since photoisomerization in densely packed azobenzene SAMs is inhibited, the chromophore density on the surface needs to be decreased. One approach is the preparation of a "mixed SAM", i.e., a SAM which consists of azobenzene-alkanethiolates (as switches) and alkanethiolates (as spacers). This of course requires that the two molecules largely mix statistically, i.e., no phase segregation occurs. One approach to obtain such mixed SAMs is using an asymmetrical disulfide of an azobenzene-alkanethiol and a simple alkanethiol. Upon adsorption on the surface the S–S bond breaks, leaving behind two thiolates [20]. Photoisomerization in such SAMs was observed indeed [20, 41, 42]. This method, however, only allows to prepare SAMs with a 1:1 mixing ratio. A more flexible approach is the formation of a SAM from a solution of mixed thiols [10]. It allows to freely adjust the concentration of the azobenzene-containing thiolate on the surface. The photoisomerization of such mixed SAMs of azobenzene-functionalized thiols and alkanethiols has been shown several times [21–23, 43, 44].

However, in some cases the two thiols separated into domains of only one species [45, 46] or one species was even fully displaced from the surface [47]. This is indicative of preferential adsorption of one species, attributable to stronger interactions between the same kind of molecules than between different molecules. In particular, phase segregation may occur if the azobenzene moieties strongly interact with each other. In mixed SAMs of an azobenzene-alkanethiol and a simple alkanethiol we could show near-statistical mixing and pronounced photoisomerization [48]. Here we assume that the long alkyl chains present in both molecules limit the preferential adsorption of the azobenzene-bearing thiol.

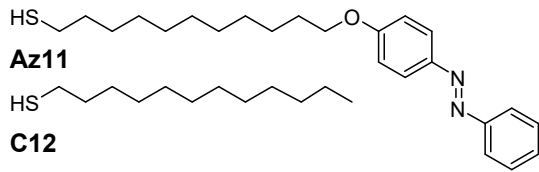In coadsorption experiments the composition of the adsorption solutions is

Figure 2.8: The thiols used in this work: 11-(4-(phenyldiazenyl)-phenoxy)undecane-1-thiol (Az11) and 1-dodecanethiol (C12).

described in terms of mole fractions. Consider a mixture of two thiols A and B. The mole fraction χ_A is then the number of molecules of species A divided by the total number of molecules:

$$\chi_A = \frac{N_A}{N_A + N_B} = \frac{c_A}{c_A + c_B}, \tag{2.27}$$

with c_A and c_B being the concentrations of the respective species in the adsorption solution.

This definition of the mole fraction can be used for both the fraction of species A in adsorption solution (χ_A^{sol}) and on the surface (χ_A^{surf}). If both thiols have the same footprint on the surface, i.e., the total number of molecules in the SAM is constant, a 1:1 exchange reaction is happening:

$$A^{sol} + B^{surf} \rightleftharpoons A^{surf} + B^{sol} \tag{2.28}$$
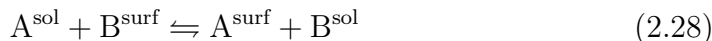
Mixed SAMs Examined in this Work In this work we prepared mixed SAMs of the azobenzene compound Az11 and the alkanethiol spacer C12 (see Fig. 2.8). The footprints of the two molecules are different: $0.242\,\mathrm{nm}^2$ and $0.217\,\mathrm{nm}^2$ are observed for the azobenzene-alkanethiol[1] and the spacer [49], respectively. Therefore, the total number of molecules on the surface changes during the exchange reaction. The amount of Az11 in a mixed SAM can still be quantified using the *relative coverage* Θ of Az11. This quantity is defined as the ratio of the number of Az11 molecules in a mixed SAM and the number of Az11 molecules in a single-component Az11 SAM:

$$\Theta(Az11) = \frac{N_{Az11}^{\text{mixed SAM}}}{N_{Az11}^{\text{pure Az11 SAM}}} \tag{2.29}$$

As shown in Sec. 4.3.2, the quantity $\Theta(Az11)$ can be determined by X-ray photoelectron spectroscopy (XPS).

2.3   Optical Properties of SAMs

In this section we review the optical properties of SAMs. We cover two aspects: the microscopic and the macroscopic properties.

Microscopically, the SAM is a molecular crystal, where the transition dipole moment (TDM) of an optical transition in a molecule and the interaction between the TDMs of neighboring molecules play an important role. Optical transitions in molecular crystals are described according to the theory of molecular excitons. It predicts the formation of one or several exciton bands,

---

[1] Footprints of Az11 and Az6 [38, 39]; Az6 is similar to Az11 but with an alkyl chain of 6 instead of 11 carbon atoms.

which can result in the shifting or splitting of absorption bands compared to the monomer.

Macroscopically, the propagation of electromagnetic waves in media is described by the Maxwell equations. At an interface to a medium with different refractive index, reflection and transmission occur according to the Fresnel equations. In this work we consider a system consisting of the environment, a thin film (the SAM), and the substrate. For this system, the reflection and transmission coefficients of an incident electromagnetic wave can be derived.

2.3.1 Molecular Excitons

The term "exciton" stands for a pair of an electron and a hole being bound to each other by Coulomb force. They occur for example by absorption of a photon. Excitons can be classified in terms of the dielectric constant of the surrounding medium and their binding energy (see for example [50, Sec. 11.11]): Wannier excitons are present in inorganic semiconductors, which have high dielectric constant. They extend across several lattice sites and typically have a binding energy below $0.1\,\mathrm{eV}$. Frenkel excitons on the other hand occur in materials with low dielectric constant such as molecular and ionic crystals and are localized at one lattice site. They have binding energies of up to $1\,\mathrm{eV}$. A SAM is a molecular crystal in two dimensions, therefore excitons in SAMs are Frenkel excitons.

In molecular crystals the wave functions of the frontier orbitals in adjacent molecules do not overlap significantly. Therefore the molecules interact mainly via van der Waals forces. Nevertheless, the excited states of the molecules in a crystal interact with each other. Depending on the oscillator strength of the optical excitation and the intermolecular distance, the exciton that was created by the photon absorption may be localized at a certain lattice site or be delocalized across several lattice sites. This effect is called excitonic coupling and was described mathematically by A. S. Davydov [51].

In the case of very weak coupling [52] the exciton is localized on a single molecule. Yet, the exciton may "hop" to a neighboring molecule. This is called Förster transfer [53]: The molecular exciton at one lattice site decays into a virtual photon, which is then absorbed by a neighboring molecule. The rate of exciton transfer inbetween molecules is proportional to $1/r^6$, with r being the intermolecular distance.

In the cases of weak to strong coupling Davydov's theory of molecular excitons is appropriate. The excited states of neighboring molecules are coupled to each other. The excited state of the crystal is then an excitonic band with as many states as the number of molecules in the crystal. The width of this exciton band is a measure of the strength of the excitonic coupling. The width of the exciton band is inversely proportional to the cube $(1/r^3)$ of the intermolecular distance r, decreases with the TDM of the monomer excitation, and depends also on the relative orientation of the TDMs of the monomers. Which of the states in the excitonic band can actually be occupied by dipole excitation, depends on the number of molecules per unit cell and on the relative orientations of the molecules. The optical properties of excitons can be understood in terms of a vector model for the TDMs, namely for the simple cases of molecular dimers and linear chains of molecules [54]:
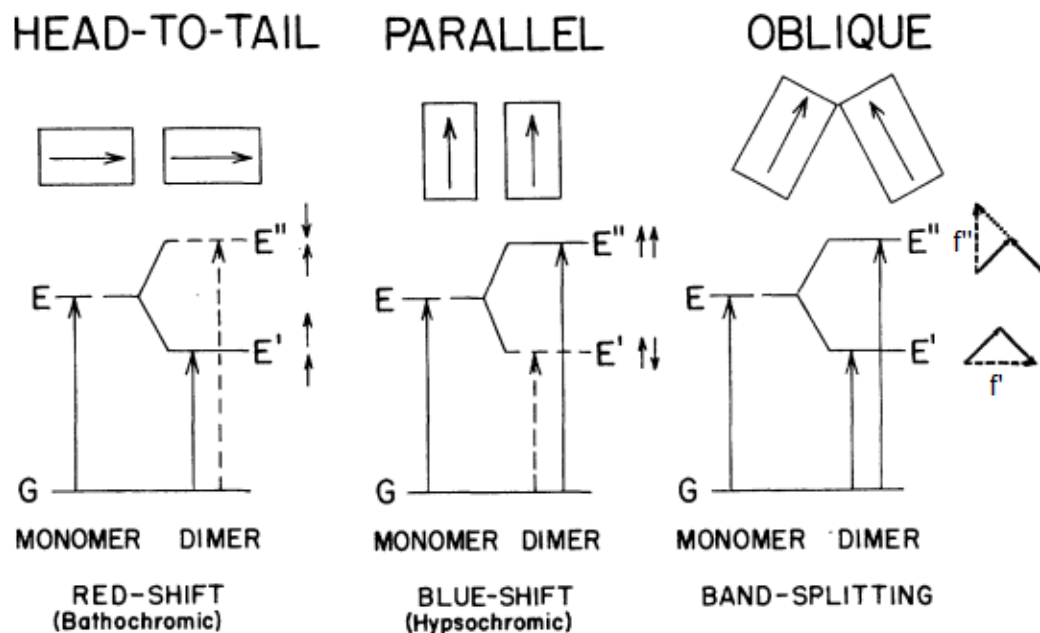
Figure 2.9: Exciton band structure in molecular dimers with various geometrical arrangements of transition dipole moments (TDMs). Transitions with nonzero (zero) TDM and the corresponding bright (dark) excited states are drawn with solid (dashed) lines. Solid (dashed) vertical arrows correspond to transitions with nonzero (zero) TDM. Taken from [54].

Molecular Dimers   Initially we consider a monomer with electronic ground state G and excited state E and an optical excitation between these two states (Fig. 2.9). The spectral properties of the dimer depend on the relative orientation of the TDMs of the two monomers: They may be arranged head-to-tail, parallel, or at an oblique angle. For each arrangement an energy level diagram is shown, with the energy levels of the monomer on the left side and the levels of the dimer on the right side. The interaction of two molecules leads to a splitting of the excited state E into two levels, E' and E". The two energy levels correspond to different phase relations of the TDMs of the monomers:

In the case of a head-to-tail arrangement of the TDMs (left), an in-phase dipole relation of TDMs corresponds to a state E' of the dimer with lower energy than the state E of the monomer due to the attractive electrostatic interaction between the TDMs. The TDM of the dimer is the vector sum of the TDMs of the monomers, resulting in a TDM of two times the TDM of the monomer. The out-of-phase dipole arrangement of the TDMs corresponds to a state E" with higher energy due to repulsive electrostatic interaction. The TDM of the dimer then adds to zero. This means that the state E" cannot be excited optically. Spectroscopically, this results in a red-shift (bathochromic shift) of the optical transition of the dimer with respect to the monomer.

For the dimer with parallel orientation of TDMs (middle), an in-phase dipole relation of the TDMs corresponds to a state E" of the dimer that is higher in energy than the state E and nonzero TDM, whereas the out-of-phase dipole arrangement of the TDMs corresponds to a state E' with lower energy and a TDM that adds to zero. This means that the state E' cannot be excited optically and a blue-shift (hypsochromic shift) of the optical transition of the
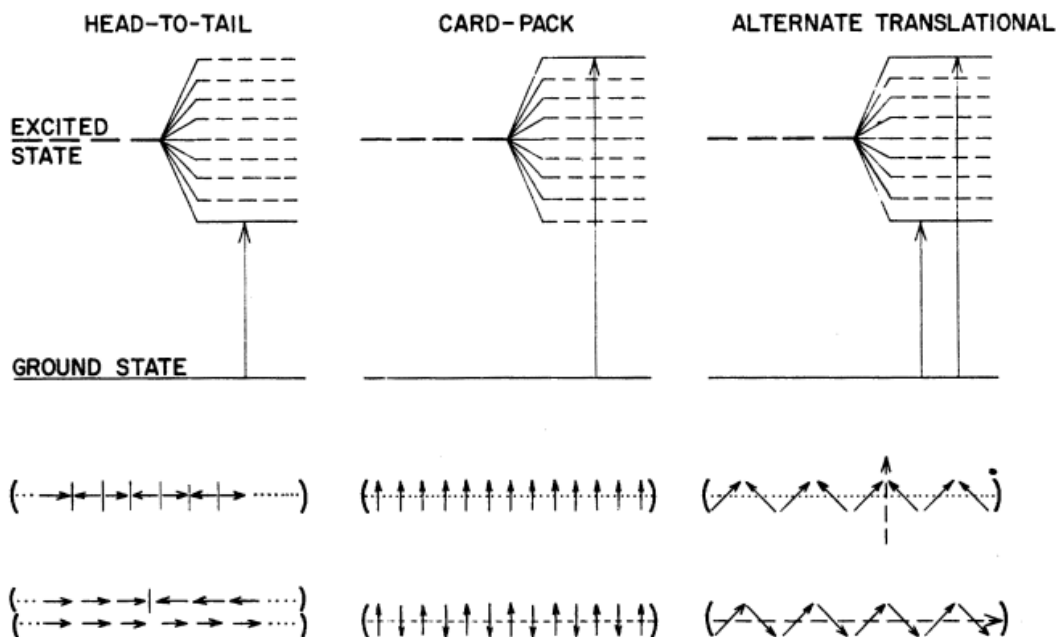
Figure 2.10: Exciton band structure in molecular chains with various geometrical arrangements of molecular TDMs. Top: energy diagrams with bright (solid) and dark (dashed) states and optically allowed transitions (vertical arrows). Bottom: respective phase relations of TDMs. Taken from [54].

dimer with respect to the monomer is observed.

In the case of oblique arrangement of the molecules (right) both the in-phase and out-of-phase dipole relation lead to a nonzero TDM of the dimer: the in-phase dipole relation corresponds to a state E" higher in energy than E and a vertical TDM and the out-of-phase dipole relation corresponds to a state E' lower in energy and horizontal TDM. Thus, a band splitting is observed.

Molecular Chains The spectroscopic properties of a linear chain of molecules can be interpreted analogously. The cases of head-to-tail, card-pack and alternate translational arrangements are illustrated in Fig. 2.10.

For the head-to-tail arrangement (left), also called *J-aggregate*, the case of all TDMs in phase (bottom vector array) corresponds to a nonzero TDM and the minimum energy of the exciton band. The dipole phase arrangement with one node (the array above) corresponds to the state next higher in energy but with a TDM vector sum of zero. With arrangements of increasing number of nodes the exciton-state energy increases, up to the arrangement with maximum exciton-state energy and also a TDM of zero (top vector array). Therefore, a red-shift with respect to the monomer transition is observed.

The card-pack arrangement (*H-aggregate*, middle panel of Fig. 2.10) is analogous, with the arrangement of in-phase TDMs, corresponding to the highest state in the exciton band, being the only with nonzero net TDM. Therefore, the card-pack arrangement exhibits a blue-shift with respect to the monomer transition.

The third case, the alternate translational arrangement of TDMs (right), has two molecules per unit cell and the arrangements with maximum and minimum exciton-state energy have both a nonzero TDM. An exciton band
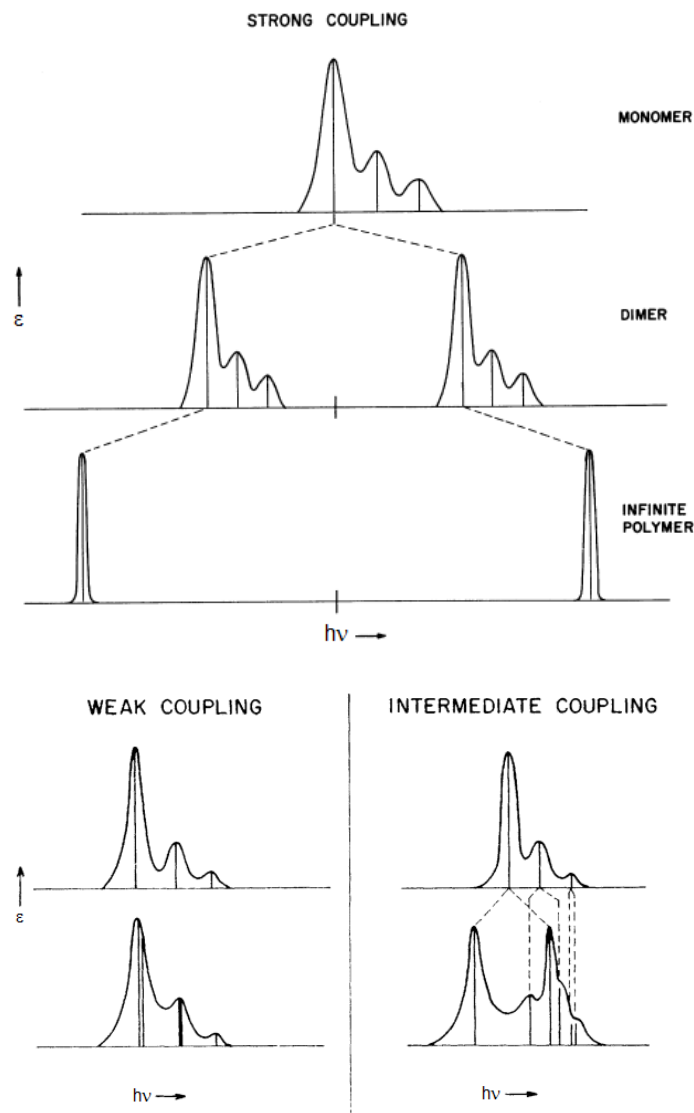
Figure 2.11: Absorption coefficient ε vs photon energy $h\nu$ in molecular arrangements of different excitonic coupling strengths: Strong coupling (top), intermediate coupling (bottom left), weak coupling (bottom right). Taken from [54].

splitting with a low-energy and a high-energy component (a J-band and an H-band) is observed. This case is described in more detail in [55].

Strength of Excitonic Coupling The model for exciton band formation outlined in the previous section considers only purely electronic transitions in a perfect crystalline ensemble. Optical excitations in molecules however involve also excitation of molecular vibrations, so-called vibronic excitations. The strength of the excitonic coupling can be classified in terms of the width of the exciton band in comparison with the width of the vibrational progression of an optical transition [54, 56]. Strong coupling means that the exciton splitting or shift is much bigger than the spacing of Franck-Condon components (top panel of Fig. 2.11). In a dimer the whole Franck-Condon envelope is subject to the exciton shift or splitting. In an infinite polymer the vibrational components vanish. The excitation is delocalized across so many molecules that every molecule has approximately the same electronic structure as the ground state.

Thus, only the 0-0 mode is allowed according to the Franck-Condon principle [54]. Weak coupling denotes the opposite case of an exciton splitting smaller than the energy of the predominant vibration quantum, which means that every vibronic transition is subject to excitonic coupling individually (bottom left panel). For an intermediate coupling strength, the excitonic shift is in the same order of magnitude as the vibration energies, which results in a complicated band structure (bottom right panel).

The Role of Disorder As explained above, in a molecular crystal with one or two molecules per unit cell, one or two states in the exciton band are optically allowed. However, this is only true for a perfectly ordered crystal. Besides vibrations, also defects break the symmetry of the system and thereby lead to other states in the exciton band to become optically allowed as well [51]. Defects may for example be vacancies, molecules with deviating orientation, or disordered zones between two different crystal domains.

2.3.2 Optical Reflectance at Thin Molecular Layers

In this subsection we deduce the reflectance of a thin film on a substrate. We are interested in the reflectance since we use a metal, which is opaque in the UV/vis spectral range. The reflectance and the transmittance of an electromagnetic wave at an interface between two media are governed by the Fresnel equations, which are reviewed shortly. A thin film on a substrate is then a system with two interfaces: environment/film and film/substrate. The part of the impinging electromagnetic wave that crosses the first interface is subject to multiple reflections within the film before being reflected into the substrate or the outer medium. In this subsection an expression for the reflectance of the thin film, taking the multiple reflections into account, is derived.

2.3.2.1 Reflection and Transmission of a Plane Wave at an Interface

The reflection and transmission of a plane wave at an interface between two media is described by the Fresnel equations, see for example Born and Wolf [57, p. 38] or Mayer [58, p. 134]. A plane wave can be written by a harmonic oscillation of its electric field vector $\vec{E}$:

$$\vec{E}(\vec{r}, t) = \vec{E_0}\, e^{i\left(\vec{k}\cdot\vec{r} - \omega t\right)}, \tag{2.30}$$

with amplitude $\vec{E_0}$, angular frequency ω, and wave vector $\vec{k} = k\hat{s}$ (wavenumber k and unit vector $\hat{s}$ in direction of wave propagation). The wavenumber can be written as $k = 2\pi/\lambda = n\omega/c_0$, with wavelength λ, refractive index n, and light velocity c_0 in vacuum.

Initially we consider a plane wave propagating through a medium with refractive index n_1 and impinging onto the interface to a medium with refractive index n_2 at an angle of incidence θ_1 (Fig. 2.12). The incoming (i) beam is then split into a reflected (r) beam and a transmitted (t) beam. The plane defined by the direction $\hat{s}_i$ of the incoming wave and the normal $\hat{z}$ to the interface is called the *plane of incidence*. The reflected and transmitted beams also lie in this plane. The reflected wave propagates at an angle of refraction $\theta_1' = \theta_1$,
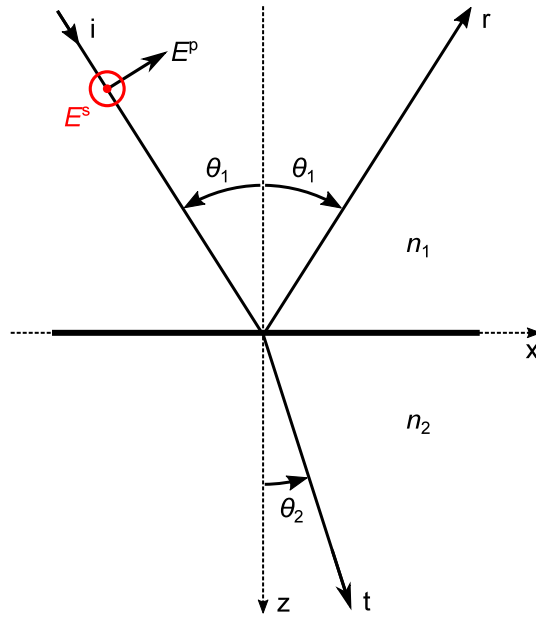
Figure 2.12: Reflection and transmission of a plane wave at an interface of two media: An incident (i) wave is split into the reflected (r) and the transmitted (t) wave. E^p and E^s are the components of the electric field vectors parallel and perpendicular to the plane of incidence, respectively.

and the transmitted wave propagates at an angle of refraction θ_2. The angle θ_2 can be determined according to Snell's law:

$$\frac{\sin\theta_2}{\sin\theta_1} = \frac{n_1}{n_2} \tag{2.31}$$

In the following we consider the components E_x^p and E_x^s of $\vec{E}_{0\mathrm{x}}$ parallel (p) and perpendicular (s)[2] to the plane of incidence, with x standing for the beams i, r and t. We then define the ratio r of reflected and incident amplitude and the ratio t of transmitted and incoming amplitude for p- and s-polarized light, respectively:

$$r^\mathrm{p} = \frac{E_\mathrm{r}^\mathrm{p}}{E_\mathrm{i}^\mathrm{p}}; \quad r^\mathrm{s} = \frac{E_\mathrm{r}^\mathrm{s}}{E_\mathrm{i}^\mathrm{s}}; \quad t^\mathrm{p} = \frac{E_\mathrm{t}^\mathrm{p}}{E_\mathrm{i}^\mathrm{p}}; \quad t^\mathrm{s} = \frac{E_\mathrm{t}^\mathrm{s}}{E_\mathrm{i}^\mathrm{s}} \tag{2.32}$$

Making use of the Maxwell equations, the *Fresnel equations* relate r and t to the angle of incidence θ_1, the angle of refraction θ_2, and the refractive indices n_1 and n_2 of the two media:

$$
\begin{aligned}
r^\mathrm{p} &= \frac{n_2\cos\theta_1 - n_1\cos\theta_2}{n_2\cos\theta_1 + n_1\cos\theta_2} \\[1em]
r^\mathrm{s} &= \frac{n_1\cos\theta_1 - n_2\cos\theta_2}{n_1\cos\theta_1 + n_2\cos\theta_2} \\[1em]
t^\mathrm{p} &= \frac{2n_1\cos\theta_1}{n_2\cos\theta_1 + n_1\cos\theta_2} \\[1em]
t^\mathrm{s} &= \frac{2n_1\cos\theta_1}{n_1\cos\theta_1 + n_2\cos\theta_2}
\end{aligned}
\tag{2.33}
$$

---

[2] originating from German *senkrecht*

The z component of the wave vector k in the media $j = 1, 2$ can be written as:

$$k_{z,j} = \frac{2\pi}{\lambda} n_j \cos \theta_j \qquad (2.34)$$

Using this relation, the Fresnel equations become[3]

$$
\begin{aligned}
r^{\mathrm{P}} &= \frac{n_2^2 k_{z,1} - n_1^2 k_{z,2}}{n_2^2 k_{z,1} + n_1^2 k_{z,2}} \\[2mm]
r^{\mathrm{s}} &= \frac{k_{z,1} - k_{z,2}}{k_{z,1} + k_{z,2}} \\[2mm]
t^{\mathrm{P}} &= \frac{2 k_{z,2}}{\frac{n_2}{n_1} k_{z,1} + \frac{n_1}{n_2} k_{z,2}} \\[2mm]
t^{\mathrm{s}} &= \frac{k_{z,2}}{k_{z,2} + k_{z,1}}
\end{aligned}
\qquad (2.35)
$$

By using $\sin^2 + \cos^2 = 1$ and applying Snell's law (2.31), the angle of refraction θ_2 can be eliminated in (2.34):

$$k_{z,j} = \frac{2\pi}{\lambda} \sqrt{n_j^2 \left(1 - \sin^2 \theta_j\right)} = \frac{2\pi}{\lambda} \sqrt{n_j^2 - n_1^2 \sin^2 \theta_1}, \qquad (2.36)$$

It can be seen that if swapping the media 1 and 2 in (2.33) and thereby replacing r by r' and t by t', the following relations hold for both polarizations:

$$r' = -r \qquad (2.37)$$

$$t' = \frac{n_2}{n_1} \frac{\cos \theta_2}{\cos \theta_1} t \qquad (2.38)$$

Using (2.35), it can also be shown that

$$r^2 + tt' = 1 \qquad (2.39)$$

for both polarizations. In the case of non-absorbing media, i.e., real refractive indexes n_1 and n_2, and as long as there is no total reflection,[4] the coefficients (2.33) are real, too. This means, the phase shifts occurring for the reflected and transmitted beams are zero or π if the coefficients are positive or negative, respectively. The Fresnel equations are also valid in case of absorbing media, i.e., when assuming complex refractive indexes $\tilde{n} = n + i\kappa$. The Fresnel coefficients then become complex, too, i.e., phase shifts between incident and reflected/transmitted beam occur.

Finally, we want to look at the intensities $I_{\mathrm{i}} = |E_{\mathrm{i}}|^2$, $I_{\mathrm{r}} = |E_{\mathrm{r}}|^2$ and $I_{\mathrm{t}} = |E_{\mathrm{t}}|^2$ of incident, reflected and transmitted light. The reflectance $R = I_{\mathrm{r}}/I_{\mathrm{i}}$ and the transmittance $T = I_{\mathrm{t}}/I_{\mathrm{i}}$ of light at the interface between the two media can then be expressed as a function of the coefficients (2.33) for s- and p-polarized light, respectively:

$$R = |r|^2; \quad T = |tt'| = \left| \frac{n_2}{n_1} \frac{\cos \theta_2}{\cos \theta_1} \right| |t|^2 \qquad (2.40)$$

---

[3] This notation is used for example in [59].

[4] Total reflection occurs if light propagates from a denser into a lighter medium ($n_1 > n_2$) and Snell's law (2.31) does not return a real value for the angle of refraction θ_2 [57, p. 47].
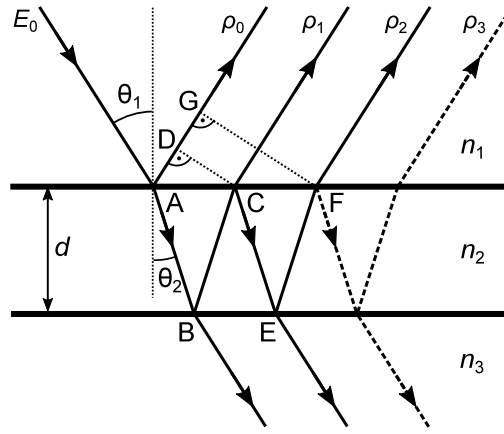
Figure 2.13: Multiple reflections and transmission in a thin layer.

In the case of non-absorbing media r and t are real, i.e., $R = r^2$ and $T = tt'$ hold. From (2.39) then follows $R + T = 1$, i.e., the interface itself does not absorb.

2.3.2.2 Reflection Coefficient of a Thin Film on a Substrate

The reflection of light at a thin layer on a substrate was for example derived by H. Mayer [58, p. 151]. Consider a beam impinging on a thin layer on a substrate, with electric field amplitude $E_0 = Ae^{-i\omega t}$. The reflected beam E_R is a sum of the beams reflected at the first interface, and after 1, 2,... internal reflections within the film of thickness d (see Fig. 2.13):

$$E_R = \sum_{m=0}^{\infty} \rho_m = \sum_{m=0}^{\infty} B_m e^{-i(\omega t - \delta_m)}, \qquad (2.41)$$

with δ_m being the phase shift of the m-th reflected beam with respect to the beam ρ_0. The phase shift is the product of the wavenumber $k_0 = \frac{2\pi}{\lambda}$ in vacuum and the difference of the optical path lengths of the beams ρ_m and ρ_0. The difference in optical path length of ρ_1 and ρ_0 is [60, Sec. 9.4.1]:

$$\Delta L = n_2(\overline{AB} + \overline{BC}) - n_1\overline{AD} \qquad (2.42)$$

with

$$\overline{AB} = \overline{BC} = \frac{d}{\cos\theta_2} \qquad (2.43)$$

and

$$\overline{AD} = \overline{AC}\sin\theta_1 = 2d\tan\theta_2\sin\theta_1 = 2d\tan\theta_2\frac{n_2}{n_1}\sin\theta_2 \qquad (2.44)$$

In the last step Snells' law (2.31) was used. The expression for ΔL now becomes

$$\begin{aligned}
\Delta L &= 2n_2d\left(\frac{1}{\cos\theta_2} - \tan\theta_2\sin\theta_2\right) \\
&= 2n_2d\frac{1}{\cos\theta_2}\left(1 - \sin^2\theta_2\right) \\
&= 2n_2d\cos\theta_2
\end{aligned} \qquad (2.45)$$

The corresponding phase shift δ is then

$$\delta = k_0 \Delta L = \frac{4\pi}{\lambda} n_2 d \cos \theta_2 \overset{(2.34)}{=} 2k_{z,2} d \tag{2.46}$$

From Fig. 2.13 it can be seen that the difference in path length of the 2nd, 3rd,... beam is then $2\Delta L$, $3\Delta L$ and so forth. Therefore the phase shift of the m-th beam is

$$\delta_m = m\delta \tag{2.47}$$

With this we can now calculate the reflection coefficient $r_{123} = E_R/E_0$ of the thin film:

$$
\begin{aligned}
r_{123} = \; & r_{12} \\
& + t_{12} r_{23} t_{21} e^{i\delta} \\
& + t_{12} r_{23} r_{21} r_{23} t_{21} e^{2i\delta} \\
& + t_{12} r_{23} r_{21}^2 r_{23}^2 t_{21} e^{3i\delta} \\
& + ...
\end{aligned}
\tag{2.48}
$$

This is a geometric series except for the first summand, therefore we obtain:[5]

$$
\begin{aligned}
r_{123} &= r_{12} + \sum_{k=0}^{\infty} t_{12} t_{21} r_{23} e^{i\delta} \left(r_{12} r_{23} e^{i\delta} \right)^k \\
&= r_{12} + \frac{t_{12} t_{21} r_{23} e^{i\delta}}{1 - r_{21} r_{23} e^{i\delta}}
\end{aligned}
\tag{2.49}
$$

By finding the common denominator and applying $r_{21} = -r_{12}$ and $r_{12}^2 + t_{12} t_{21} = 1$ (Eqs. 2.37 and 2.39) we finally get the following result:[6]

$$r_{123} = \frac{r_{12} + r_{23}\, e^{i\delta}}{1 + r_{12} r_{23}\, e^{i\delta}}, \quad \text{with } \delta = \frac{4\pi}{\lambda} n_2 d \cos \theta_2 = 2k_{z,2} d, \tag{2.50}$$

valid for s- and p-polarization. The reflectance of the film–substrate system is then given by $R_1 = |r_{123}|^2$.

2.3.2.3 Differential Reflectance

In the case of very thin films (in particular single molecular layers) the reflectance R_1 of the substrate/film system is dominated by the optical properties of the substrate. Or, in other words, the reflectance of the substrate, R_0, and the reflectance of the film-covered substrate are very similar. Therefore, the differential reflectance (DR) is determined [61]:

$$\mathrm{DR} \equiv \frac{\Delta R}{R} = \frac{R_1 - R_0}{R_0} \tag{2.51}$$

This way spectral features attributable to the substrate only are eliminated. DR spectroscopy is introduced in detail in Sec. 3.3.5.

---

[5] $\sum_{k=0}^{\infty} a_0 q^k = \frac{a_0}{1-q}$ for $|q| < 1$, which is fulfilled since the magnitude of reflection coefficients is always smaller than 1.

[6] The same equation can be obtained via a matrix formalism [57, Sec. 1.6].

The expression (2.50) for the reflection coefficient of a thin film can be used to simulate experimental DR spectra of thin films [59]. The reflectances are then given by $R_0 = |r_{13}|^2 = |r_{123}(d = 0)|^2$ and $R_1 = |r_{123}|^2$. The film is considered homogeneous, with complex refractive index $n_2 = \sqrt{\epsilon_2}$, with ϵ_2 being the dielectric function of the film. The dielectric function can modeled according to a classical model, assuming harmonic oscillators with respective resonance frequency ω_j, oscillator strength f_j and damping γ_j [62, Sec. 7.5]:

$$
\begin{aligned}
\epsilon_2(\omega) &= \epsilon_{\text{const}} + \frac{N_e e^2}{\epsilon_0 m_e} \sum_j \frac{f_j}{\omega_j^2 - \omega^2 - i\omega\gamma_j}, \\
&= \epsilon_{\text{const}} + \frac{N_e e^2}{\epsilon_0 m_e} \sum_j \frac{f_j \left(\omega_j^2 - \omega^2\right)}{\gamma_j^2 \omega^2 + \left(\omega_j^2 - \omega^2\right)^2} \\
&+ i \frac{N_e e^2}{\epsilon_0 m_e} \sum_j \frac{\gamma_0 f_j \omega}{\gamma_j^2 \omega^2 + \left(\omega_j^2 - \omega^2\right)^2}
\end{aligned}
\tag{2.52}
$$

with a constant offset $\epsilon_{\text{const}} \geq 1$, number N_e of electrons per unit volume, electron charge e, electron mass m_e and vacuum permittivity ϵ_0. ϵ_{const} originates from resonances at frequencies far above the spectral window considered in this work (if all resonances were included, ϵ_{const} would be 1).

Chapter 3

Experimental Techniques

In this thesis different complementary methods to examine molecular switches in SAMs were used. The core-level techniques X-ray photoelectron spectroscopy (XPS) and near edge X-ray absorption fine structure (NEXAFS) spectroscopy allow us to study chemical composition and structure of SAMs. Ultraviolet-visible (UV/vis) spectroscopy examines optical properties of molecular switches in solution and in SAMs, i.e., deals with excitations of valence electrons.

3.1 X-ray Photoelectron Spectroscopy (XPS)

In XPS, also called electron spectroscopy for chemical analysis (ESCA), core electrons are emitted after absorption of X-ray light of constant photon energy. The number of photoelectrons is then measured as a function of electron energy. This allows to determine the binding energy of the emitted core electrons. An overview over the usage of XPS for the examination of molecular layers can be found in [63]. The chemical sensitivity of XPS is based on the fact that the binding energy of a core electron is influenced by valence electrons. Therefore, XPS can be used to examine the chemical environment of a specific element. Such an analysis is quantitative since the photoemission cross-section for core electrons is independent of the chemical environment. This means that the number of photoelectrons is proportional to the amount of a certain species.

3.1.1 Electron Energy Referencing

The kinetic energy $E_{\mathrm{kin}}^{\mathrm{s}}$ of photoelectrons in front of the sample is given by

$$E_{\mathrm{kin}}^{\mathrm{s}} = h\nu - E_{\mathrm{bind}} - \Phi_{\mathrm{s}}, \tag{3.1}$$

with photon energy $h\nu$, binding energy E_{bind} and work function Φ_{s} of the sample. Sample and analyzer are connected to the same ground, therefore their Fermi levels are aligned, however their work functions are usually different (see Fig. 3.1). In a photoemission experiment one measures the kinetic energy $E_{\mathrm{kin}}^{\mathrm{a}}$ of photoelectrons with respect to the analyzer:

$$E_{\mathrm{kin}}^{\mathrm{a}} = h\nu - E_{\mathrm{bind}} - \Phi_{\mathrm{a}}, \tag{3.2}$$
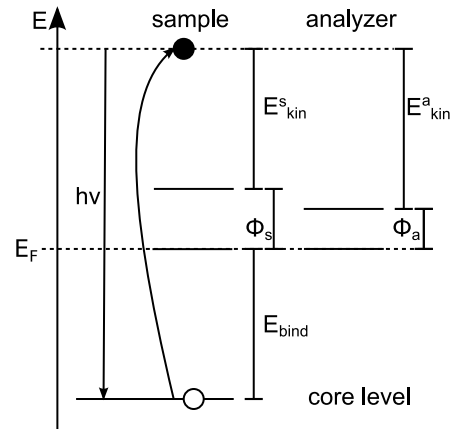
Figure 3.1: Energy levels for a conductor in photoemission spectroscopy. Adopted from [29].

Figure 3.2: Geometry used for XPS measurements: View from the side. The X-rays impinge on the sample in grazing incidence from the right and are vertically polarized. Thus, the electric field is nearly perpendicular to the sample surface. The electrons are detected in near-normal emission from the top. Exact angles are given in Fig. 3.7. Taken from [29].
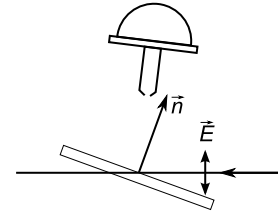
with known work function Φ_a of the analyzer. In practice, the binding energy of core levels is determined from the difference to a reference level with known binding energy $E_{\text{bind}}^{\text{ref}}$:

$$E_{\text{bind}} = E_{\text{bind}}^{\text{ref}} + E_{\text{kin}}^{\text{ref}} - E_{\text{kin}} \tag{3.3}$$

In this work the bulk component of the Au $4f_{7/2}$ level of the gold substrate, at a binding energy of 83.95 eV [64], was used as reference.

3.1.2 Setup and Principle of Measurement

All measurements were performed at an undulator beamline of the Bessy II synchrotron facility (Helmholtz-Zentrum Berlin). An overview of the generation of X-ray light in undulators can be found in [65, p. 16]. The measurement geometry is shown in Fig. 3.2. It is chosen because of the following considerations: (a) Photoelectrons are emitted in the direction of the electric field of the X-ray light, and the electron analyzer should be in the direction of the emitted photoelectrons. (b) The interaction of the photoelectrons with the layer should be minimized, therefore, (near-)normal emission of the photoelectrons with respect to the sample is desired.

Details to the experimental procedures are given in Sec. 9.4.1.

3.1.3 Description of XP Spectra

Peak Structure   In this work we examined photoemission from the C 1s, N 1s, O 1s, S 2p and Au 4f levels. In XPS the final state is an atom with a core hole. Its spin is $s = 1/2$, which couples to the orbital angular momentum l according to L-S coupling. In L-S coupling we obtain the total angular momentum $j = l \pm s$ $(j > 0)$ with $2j + 1$ degenerate states. In the case of a 1s level $(l = 0)$ a singlet with $j = 1/2$ is observed. A 2p level $(l = 1)$ is split into two states: $j = 3/2$ with 4-fold degeneracy and $j = 1/2$ with 2-fold
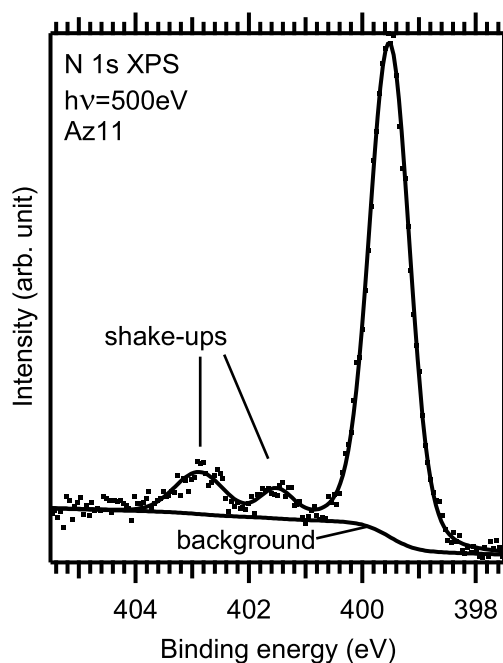
Figure 3.3: N 1s XP spectrum of an Az11 SAM on gold. The spectrum was normalized to background on the low-energy side. A single Voigt profile was used for the main peak and two Gaussian profiles were used for the shake-ups. The background was modeled with a sum of a Shirley type and a linear background as described in the text.

degeneracy. Thus, XPS at the S 2p level results in a doublet with amplitude ratio $2p_{3/2} : 2p_{1/2} = 2 : 1$. Analogously, in measurements of the Au 4f level ($l = 3$) one obtains a doublet of Au $4f_{7/2}$ and Au $4f_{5/2}$, with a peak amplitude ratio of $4 : 3$.

Satellite Peaks An excitation of a valence electron may happen simultaneously with the photoemission process. Thus, the energy of the photoelectron is reduced and in the vicinity of the direct photoemission peak a satellite peak with apparent higher binding energy is observed. Such satellite peaks are called shake-ups.

Peak Shape The shape of photoemission peaks depends on many factors. From the finite lifetime of the core hole a Lorentzian line shape is expected. However, inhomogeneous broadening and instrumental effects such as the resolution of the electron analyzer lead to a broadening of the peak described by the convolution of the Lorentzian with a Gaussian. This convolution is called a Voigt profile and has no analytical solution. Instead of executing the convolution numerically for every peak fit, an approximation of the Voigt profile was used in this work (details see Sec. 9.4.1).

Background The photoelectrons may lose energy by excitation of phonons or formation of electron-hole pairs. This leads to quasi-continuous energy losses, i.e., the background increases stepwise underneath the peaks. Shirley [66] developed a model to describe such a background. He used a background proportional to the integral over the peak starting at a binding energy below the onset of the peak. There the background is determined in an iterative method using the measured data directly. In contrast, in our data analysis we integrated the peak model function, which allows to determine the Shirley proportionality factor and the peak parameters in one fit (for details see Sec. 9.4.1).

Additionally, we observe a linear background which can be attributed to secondary electrons released by photoemission processes with binding energies lower than the current peak.

3.1.4 Radiation Damage

X-ray exposure leads to radiation damage in organic samples. This can be reduced by reducing the sample temperature [67]. Therefore, all measurements were performed at temperatures of about $100\,\mathrm{K}$ by cooling with liquid nitrogen.

Also, the UHV chamber was placed at a position where the X-ray spot size on the sample was approximately $1 \times 2\,\mathrm{mm}^2$. In order to minimize X-ray beam damage further, a new spot was chosen for each measurement and the X-ray beam was blocked in between measurements.

3.2 Near Edge X-ray Absorption Fine Structure (NEXAFS) Spectroscopy
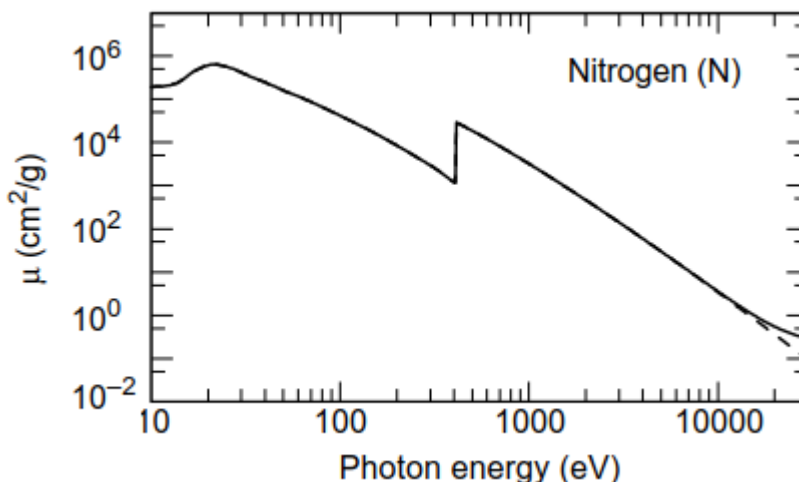
Figure 3.4: Mass absorption coefficient μ of atomic nitrogen as a function of photon energy. Taken from [68, Sec. 1.6].

In X-ray absorption spectroscopy the absorption of X-ray light is measured as a function of the photon energy. Fig. 3.4 shows the mass absorption coefficient μ of nitrogen. At about $400\,\mathrm{eV}$ the ionization potential of the 1s electrons is reached, therefore photoemission from the 1s level becomes possible, leading to a sharp increase of the X-ray absorption. This feature is called the *absorption edge*. In near edge X-ray absorption fine structure (NEXAFS) spectroscopy the X-ray absorption is measured in the vicinity of the absorption edge. The principles of NEXAFS spectroscopy are described in [69]. In NEXAFS, resonant excitations from core levels into unoccupied molecular states below and above the absorption edge are examined.
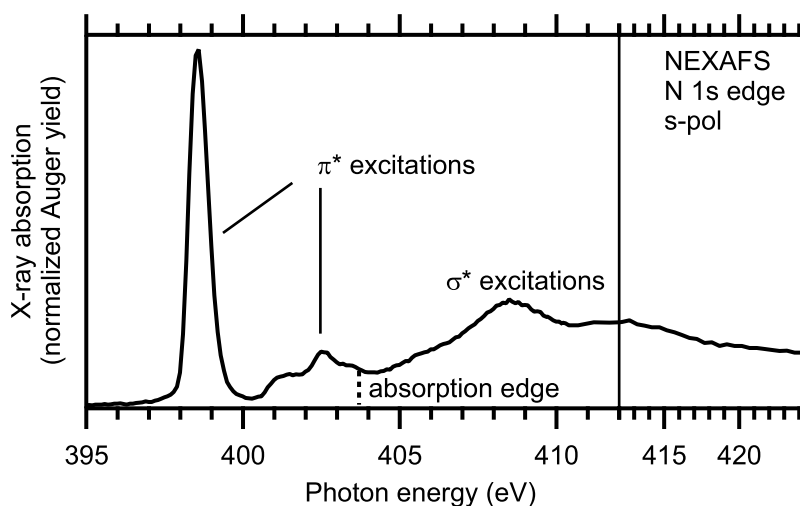
Figure 3.5: N 1s NEXAFS spectrum of a 100 % Az11 SAM. Position of the absorption edge according to the N 1s XPS binding energy of 399.5 eV (Fig. 3.3) plus the work function of the sample of 4.2 eV [70].

3.2.1 Spectral Features

Fig. 3.5 shows a NEXAFS spectrum of an Az11 SAM. The N 1s absorption edge is only weakly visible at a photon energy of about 403.7 eV. Instead, the spectrum is dominated by absorption peaks corresponding to resonant transitions from N 1s into unoccupied molecular states, namely $\pi^\star$ states below the absorption edge and $\sigma^\star$ states above the absorption edge. These spectral features are named after excitations into the respective orbitals:

π **Orbitals**   possess a nodal plane and are antisymmetric with respect to this plane. The π bonds in double and triple bonds and aromatic systems are formed from the p orbitals of the involved atoms. In aromatic systems these π orbitals are delocalized. The corresponding anti-bonding orbitals are called $\pi^\star$ orbitals. Typically, the energetically lowest $\pi^\star$ states represent bound excited states and are thus observed below the absorption edge.

σ **Orbitals**   are symmetric with respect to a symmetry plane through the bond axis and possess no nodal plane. In organic molecules the single bonds and the first bonds of multiple bonds are σ bonds. The σ states are typically lower in energy than π states and the corresponding anti-bonding $\sigma^\star$ states are lying at higher energies than their $\pi^\star$ counterparts. Since in most cases $\sigma^\star$ orbitals do not form bound states anymore, $\sigma^\star$ states usually lie above the absorption edge. They overlap with free electron states and are called shape resonances. The name refers to the model that the core electron leaving the molecule is subject to multiple scattering at the potential walls [69, Sec. 4.2.4].

3.2.2 Auger Yield

X-ray absorption can be measured via the electrons emitted in the decay process of the core hole. Auger decays represent the dominant core-hole decay processes in light atoms such as carbon and nitrogen. A schematic of the

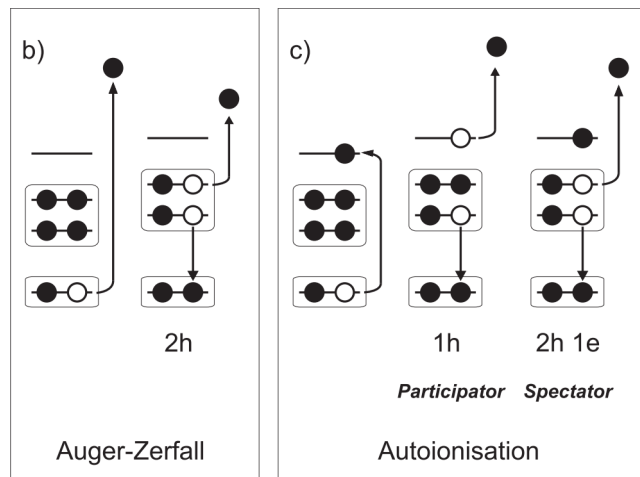**Figure 3.6:** Auger decay in carbon. *Left: normal Auger decay, i.e., following direct photoemission:* An X-ray photon is absorbed and a 1s electron is emitted, i.e., excited into an unbound state. An atom with 1 core hole remains. An electron from the valence orbitals fills the hole and the energy is transferred to a second valence electron, the Auger electron. The Auger electron is emitted. The kinetic energy of the Auger electron is independent of the photon energy initially used to create the core hole. *Right: Auger decay following resonant excitation, i.e., autoionization:* An X-ray photon is absorbed and excites a 1s electron into an unoccupied molecular state. The core hole is then filled by a valence electron. The energy is either transferred to the excited electron (participator decay) or another valence electron (spectator decay). Both the spectator and the participator electron have a higher energy than the Auger electron and shift in photon energy (Figure from [65]).

Auger process and the related autoionization process is shown in Fig. 3.6. In this work we measure the yield of Auger electrons, i.e., the *Auger yield*, which is assumed to be proportional to the X-ray absorption cross-section σ_{abs}.

3.2.3   Setup and Principle of Measurement

For NEXAFS measurements we used the same setup as in XPS (see Sec. 3.1.2), but in another detection geometry, as shown in Fig. 3.7. The X-rays were horizontally polarized, with the electron analyzer being oriented perpendicular to the X-ray polarization. This minimizes the contribution of directly photoemitted electrons to the measured signal since these are predominantly emitted in direction of the electric field. The polarization of the X-rays with respect to the sample is changed by rotating the sample. Typically, measurements in s-polarization, p-polarization and at an intermediate polarization, the magic angle (see Sec. 3.2.7), were performed. The electron analyzer was set to a pass energy of 50 eV, i.e., an energy window of 5 eV was available to measure a significant portion of the KLL Auger electron peak[1] but parts of the spectator and the participator channel are neglected.

   NEXAFS spectra were recorded by scanning the photon energy stepwise. After each datapoint a photodiode is moved into the beam path. The diode current measured is then a measure of the X-ray photon flux and this mea-

---

[1]   Nominal kinetic energies of 259 eV and 377 eV for the C 1s and N 1s edges, respectively, details see Sec. 9.4.2.
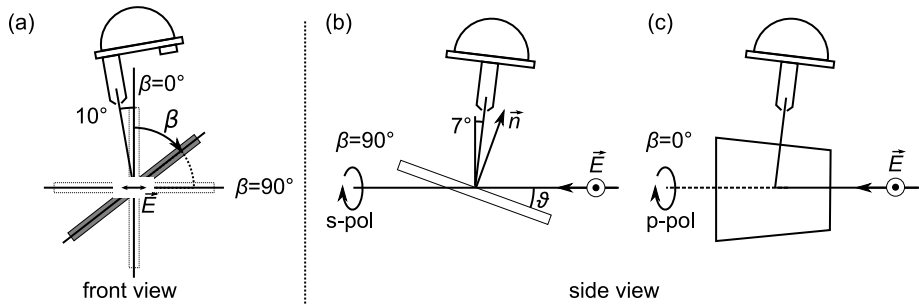
Figure 3.7: NEXAFS measurement geometry: (a) *View onto the sample in direction of the X-ray beam.* The sample can be rotated around the direction of incidence. β denotes the sample rotation. The emitted Auger electrons are detected in a direction nearly perpendicular to the X-ray polarization, minimizing the contribution of photoelectrons to the signal. (b, c) *View from the side.* (b) *sample orientation for s-polarized measurements:* The sample plane is tilted by $\vartheta=20°$ with respect to the direction of incidence in order to create a spot on the sample. The paper plane is the plane of incidence. (c) *sample orientation for p-polarized measurements:* The sample is rotated by 90° compared to (b). Now the plane of incidence is perpendicular to the paper plane and thus the radiation is p-polarized. The analyzer is rotated by 10° out of the paper plane (see (a)) so that electrons can be detected from the top in this geometry. For some measurements an angle β of 10° was used in order to facilitate electron detection further. Yet, the radiation is predominantly p-polarized, with a small s-polarized component. Hence, the spectra are denoted p-pol. Figure taken from [29].

surement is needed for the normalization of spectra (see Sec. 3.2.4). The diode also acts as a beam block while the undulator and the monochromator of the beamline are moved to the next photon energy. This minimizes the X-ray exposure of the sample.

NEXAFS Kinetics were recorded by measuring the Auger yield in time at a constant photon energy. The sample was exposed to X-ray light for 1 s in 5.5 s intervals in order to reduce the X-ray exposure of the sample.

As discussed in Sec. 3.1.4, cooling the sample reduces X-ray beam damage. Thus, most[2] measurements were performed at temperatures of about 100 K by cooling with liquid nitrogen. Additionally a fresh spot on the sample was chosen for every measurement.

3.2.4 Normalization and Background Correction

The X-ray photon flux of the beamline varies with the photon energy and time. Therefore the spectrum is divided by the photodiode current, which is proportional to the X-ray photon flux. In the spectral region lower in energy than the first resonant transitions, no Auger electrons are created, thus the spectrum is normalized to zero in this region. At photon energies above the $\sigma^\star$ resonances the X-ray absorption is dominated by excitation of electrons from 1s states into continuum states. As the 1s orbitals are isotropic, we also expect no polarization dependence of absorption in this energy range and the spectrum is normalized to 1 in this region.

---

[2] All, except noted otherwise.

3.2.5   X-ray Flux at the C 1s Edge

The X-ray flux at the C 1s edge is strongly reduced due to elemental carbon building up on the X-ray optics in the beamline. This is due to radiolysis of CO present in the vacuum system. Since we normalize the spectra to the X-ray flux, this should not play a role. However, the light is not entirely monochromatic and contains 2nd and 3rd harmonics, which leads to secondary electrons which are falsely detected. Since the fundamental is so low in intensity these secondary electrons contribute significantly to the electron signal. This contribution is estimated by recording an electron spectrum with the same analyzer settings as in NEXAFS measurements, for a photon energy near the carbon edge. In these spectra the Fermi edge of the gold substrate is visible and any electron signal above Fermi edge then stems from photoemission by higher harmonics. This signal is then compared with the signal in the Auger detection window (details see [29]). The false light also contributes to the diode current but this effect is smaller and can be neglected.

3.2.6   Photon Energy Calibration

The monochromators of synchrotron beamlines need to be calibrated regularly. This is done by recording NEXAFS spectra of reference samples with known core-level transitions and applying a linear correction. C 1s NEXAFS spectra were calibrated according to the 1s→$\pi^\star$ excitation in highly oriented pyrolytic graphite (HOPG), see Fig. 3.8a. This excitation is found at a photon energy of 285.38 ± 0.05 eV [71]. N 1s NEXAFS spectra were calibrated according to the $\pi^\star$ transition of nitrogen gas (N_2), see Fig 3.8b. The transition is split into several vibronic components. The maximum of the 0-0 mode of the $\pi^\star$ transition lies at 400.87 eV [72]. The energy corrections in C 1s and N 1s spectra were well below 1 eV (details see Sec. 9.4.2).

3.2.7   Determination of Molecular Orientation

The determination of molecular orientations of adsorbed molecules from the angular dependence of resonant core excitations has been developed by Stöhr and Outka [69, 73]. A sketch of the relevant angles in NEXAFS is shown in Fig. 3.9. We consider the transition dipole moment $\vec{\mu}$ of a core excitation. α is the polar angle of $\vec{\mu}$ and ϕ is its azimuthal angle. ϑ is the angle of incidence of the impinging X-ray light and β is the angle between the electric field vector $\vec{E}$ of the X-ray light and the plane of incidence. Both are controlled in the experiment (cf. Fig. 3.7). After integration over the azimuthal angle ϕ, the NEXAFS intensity $I(\beta)$ can be written as [29]:

$$I(\beta) \propto \sin^2 \alpha \ \left(1 - 3\cos^2 \vartheta \cos^2 \beta\right) + 2\cos^2 \vartheta \cos^2 \beta \qquad (3.4)$$

However, this equation is valid only if the synchrotron radiation is entirely polarized, which is usually not the case. Therefore, we have to take the limited degree of polarization into account: The electrical field vector can be decomposed into a component with the desired horizontal polarization E_h and a component with the perpendicular (vertical) polarization E_v. The degree of
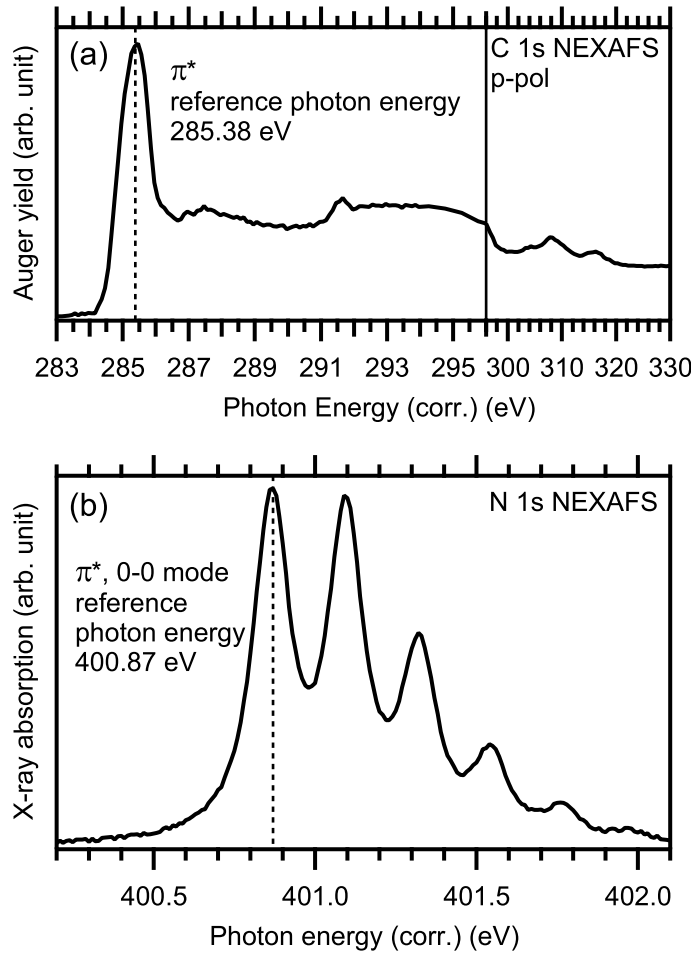
Figure 3.8: Reference measurements for photon energy calibration of NEXAFS spectra. (a): C 1s spectrum of highly oriented pyrolitic graphite (HOPG) used for calibration of C 1s NEXAFS spectra. (b): N 1s spectrum of nitrogen (N_2) in the gase phase used for calibration of N 1s NEXAFS spectra. The latter measurement was performed by Willy Mahler, Bessy II Synchrotron Radiation Facility, Berlin, Germany.

polarization P is defined as the ratio of the *intensity* with the desired polarization to the total intensity:

$$P = \frac{E_h^2}{E_h^2 + E_v^2} \tag{3.5}$$

$I(\beta)$ is the absorbed intensity for perfectly polarized light. We obtain for the absorbed intensity $I(\beta, P)$ with light with a degree of polarization P.

$$I(\beta, P) = PI(\beta) + (1 - P)I(\beta - 90°) \tag{3.6}$$

With the proportionality constant C we obtain:

$$I(\beta, P) = C\left[P\left(\sin^2\alpha\left(1 - 3\cos^2\beta\cos^2\vartheta\right) + 2\cos^2\beta\cos^2\vartheta\right)\right.$$
$$\left. + (1 - P)\left(\sin^2\alpha\left(1 - 3\sin^2\beta\cos^2\vartheta\right) + 2\sin^2\beta\cos^2\vartheta\right)\right] \tag{3.7}$$

Experimental Routine For the determination of the orientational angle α we performed NEXAFS measurements of SAMs at three different sample rotations: $\beta = 0$ or $10°$, $\beta = 90°$, and at an intermediate angle, the so-called magic
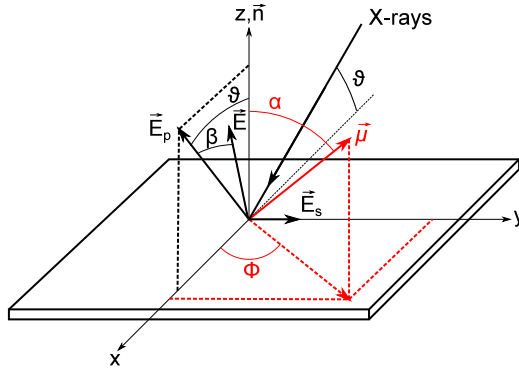
Figure 3.9: Definition of the angles used to calculate the molecular orientation: The coordinate system is the sample coordinate system. The surface normal $\vec{n}$ is the z-axis. The X-rays impinge in the (x, z) plane. ϑ is the angle between the incidence direction and the x-axis. $\vec{E}$ is the electric field vector of the linearly polarized radiation. β is the angle by which $\vec{E}$ is rotated out of the incidence plane (x, z). β and ϑ are the same as in Fig. 3.7. $\vec{E}$ can be decomposed into a component parallel to the incidence plane $\vec{E}_p$ and a component perpendicular to the incidence plane $\vec{E}_s$. ϑ is also the polar angle of $\vec{E}_p$. $\vec{\mu}$ is the transition dipole moment of the resonant excitation. α is its polar angle, i.e., the angle between $\vec{\mu}$ and the surface normal. This angle is to be determined by NEXAFS. ϕ is the orbital vector's azimuthal angle. Adopted from [29].

angle (see next paragraph). The normalized spectra were then integrated in an interval across the $\pi^\star$ states, resulting in absorption intensities $I(\beta, P)$. Eq. 3.7 was then fitted to the values $I(\beta, P)$, with C and α as free parameters. We assumed a degree of polarization of $P = 0.96$.

Magic Angle   We look for a sample rotation β for which the absorbed intensity (3.4) is independent from the molecular orientation α. This is the case for

$$\left(1 - 3\cos^2\vartheta\cos^2\beta\right) = 0 \tag{3.8}$$

For our setup with $\vartheta = 20°$ we obtain a *magic angle* $\beta_{\mathrm{magic}} = 52.1°$.

3.3   Ultraviolet-visible (UV/vis) Spectroscopy

3.3.1   Fundamentals

In UV/vis spectroscopy the absorption of ultraviolet-visible light by a sample is examined as a function of the wavelength λ. Consider a plane wave

$$E(x, t) = E_0 e^{i(kx - \omega t)} \tag{3.9}$$

propagating in a medium along the x axis. The wavenumber k is given by $k = \tilde{n}\omega/c_0$, with the complex refractive index $\tilde{n} = n + i\kappa$ of the medium, and the speed of light in vacuum, c_0. Thus, (3.9) can be written as

$$E(x, t) = E_0 e^{i\left(\frac{n\omega}{c_0}x - \omega t\right)} e^{-\frac{\kappa\omega}{c_0}x} \tag{3.10}$$

The intensity of the light is given by

$$I(x) = |E(x,t)|^2 = |E_0|^2 e^{-\frac{2\kappa\omega}{c_0}x} \tag{3.11}$$

$$\equiv I_0 \, e^{-\alpha x}, \text{ with } \alpha = \frac{2\kappa\omega}{c_0} = \frac{4\pi\kappa}{\lambda}. \tag{3.12}$$

Starting from an initial value I_0, the intensity I of light decreases exponentially with path length x through the medium. α is called the attenuation coefficient. If the medium consists of n_p particles per unit volume, each with an *absorption cross-section* σ^{abs} in cm^2, the attenuation coefficient is given by

$$\alpha(\lambda) = n_p \, \sigma^{abs}(\lambda) \tag{3.13}$$

If the absorbing medium is a solution of molecules with concentration c_{sol} (in moles per liter), the attenuation coefficient is given by

$$\alpha(\lambda) = c_{sol} \, \varepsilon^*(\lambda). \tag{3.14}$$

$\varepsilon^*(\lambda)$ is the molar extinction coefficient[3], which is characteristic for the respective substance. Using this definition, the transmittance T of the sample is

$$T \equiv \frac{I}{I_0} = \exp\left[-c_{sol} \, \varepsilon^*(\lambda) \, x\right] \tag{3.15}$$

In chemistry, the absorbance A is defined as the negative *decadic* logarithm of the transmittance T:

$$A \equiv -\lg(T) = -\frac{\ln(T)}{\ln(10)} \tag{3.16}$$

With (3.15) we obtain

$$\begin{aligned} A &= \frac{\varepsilon^*(\lambda)}{\ln(10)} \, c_{sol} \, x \\ &= \varepsilon(\lambda) \, c_{sol} \, x, \end{aligned} \tag{3.17}$$

with $\varepsilon(\lambda) = \varepsilon^*(\lambda)/\ln(10) \approx 0.434 \, \varepsilon^*(\lambda)$ being the (decadic) molar attenuation coefficient. Eq. (3.17) is the so-called Lambert-Beer law [74] and constitutes the foundation of UV/vis spectroscopy: Knowing the absorbance A allows the determination of the sample concentration c if the molar attenuation coefficient ε is known and vice versa.

The Lambert-Beer law is only valid if:

- the substance to be determined is homogeneous

- the concentration of the substance is low (usually below $0.01 \, \text{mol/l}$), so that interactions between the substance atoms or molecules can be neglected

- the atoms or molecules are not influenced by the light, i.e., no optical pumping or saturation occurs

---

[3] Not to be confused with the dielectric function ϵ in electrodynamics and optics.

- the incident radiation consists of parallel rays, each traversing the same length in the absorbing medium

- the light is monochromatic, i.e., the spectral width is small compared with the width of the absorption bands to be examined

The Lambert-Beer law only describes the propagation of light in a medium and does not take reflections at the interfaces of the sample into account: First, part of the incident intensity is reflected at the first interface, and second, multiple reflections within the sample may play a role. For absorbance spectroscopy of solutions this problem can be overcome if the absorbance of the solvent is subtracted from the absorbance of the solution (see Sec 3.3.4): If the concentration of the solution is low, the difference in refractive index of solvent and solution are negligible and distortions due to reflections at the interfaces cancel out.

Last but not least we make a connection from the imaginary part κ of the complex refractive index $\tilde{n}$ of a material to the decadic molar attenuation coefficient ε determined in an absorbance measurement. The attenuation coefficient (3.12) is given by

$$\alpha(\lambda) = \frac{4\pi\kappa}{\lambda} \overset{(3.14)}{=} c_{\text{sol}} \ln(10)\, \varepsilon(\lambda) \tag{3.18}$$

Thus:

$$\kappa(\lambda) = \frac{c_{\text{sol}} \ln(10)}{4\pi} \varepsilon(\lambda)\lambda \tag{3.19}$$

This relation is later used when comparing the optical properties of Az11 solutions and Az11 SAMs (cf. Sec. 6.2).

3.3.2   Setup

In this work UV/vis spectroscopy was performed using a PerkinElmer Lambda 850 spectrometer. This device exhibits three design principles which are crucial in particular for the examination of photoswitches: First, white light is monochromatized *before* it illuminates the sample and the wavelength λ is scanned by rotating the monochromator grating. This design allows us to examine the temporal evolution of the differential reflectance of photoresponsive samples at certain wavelengths. (In an alternative design white light illuminates the sample and the transmitted light is then spectrally dispersed by a monochromator and recorded by a charge-coupled device (CCD) sensor. In this case the photon flux on a photoresponsive sample would be too high to perform time-resolved measurements with good signal-to-noise ratio.) Second, the monochromatized light is split into two beams, the sample beam and the reference beam. The intensity ratio of both beams is then alternatingly measured by a single photomultiplier. This way light intensity variations in time are eliminated, which is a prerequisite for kinetics measurements. Third, a double monochromator is used. This greatly reduces stray light.[4]

A schematic beam path of the spectrometer is shown in Fig. 3.10. White light in the visible/near-infrared range up to 900 nm is created by a tungsten

---

[4]   The ratio of stray light intensity to desired light intensity of a double monochromator is the product of the respective ratios of the two individual monochromators.
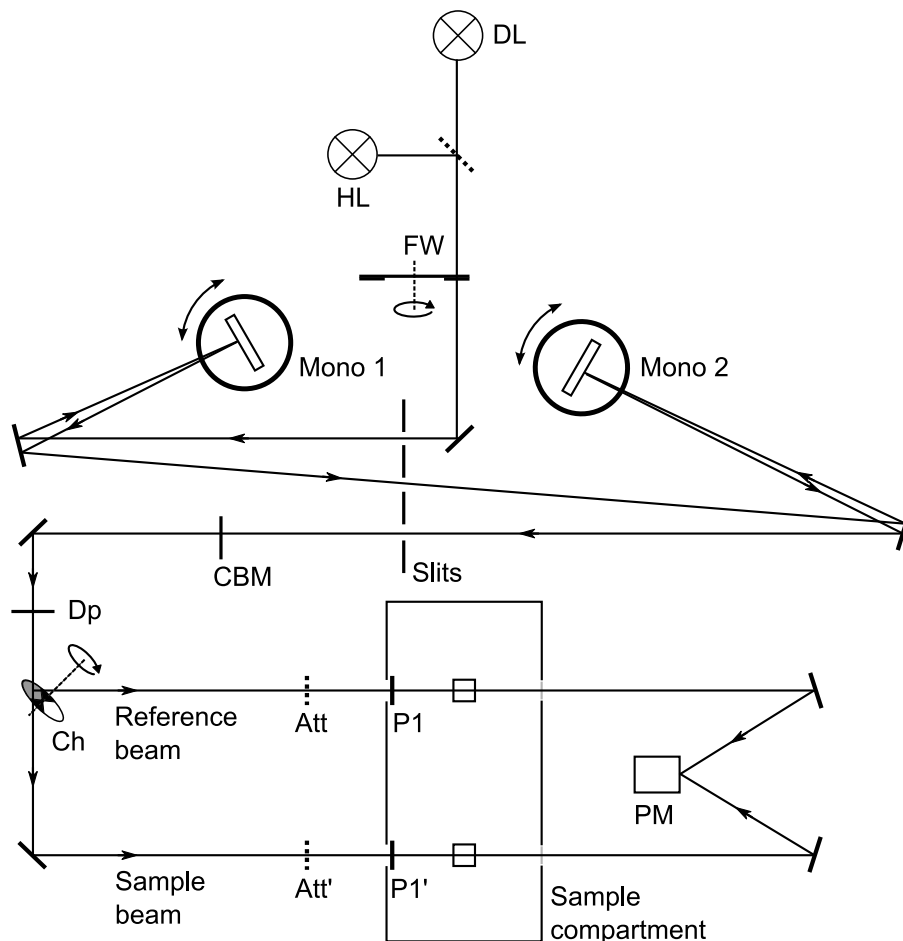
Figure 3.10: Schematic beam path of the Lambda 850 spectrometer. Halogen lamp HL, deuterium lamp DL, filter wheel FW, double monochromator, common beam mask CBM, depolarizer Dp, chopper wheel Ch, optional attenuators Att and Att', optional coupled pair of linear polarizers P1 and P1', photomultiplier PM. The chopper wheel has one mirror segment, one open segment and two dark segments.

halogen lamp (HL) and UV light with wavelengths down to 175 nm is created by a deuterium arc lamp (DL).[5] In our experiments the light source is switched at 319.2 nm. The white light is passed onto the double monochromator, which consists of two blazed reflective holographic gratings each mounted onto a rotating table. Here the exit slit of the first monochromator serves as the entrance slit of the second monochromator. The slits can be set to a spectral resolution between 0.05 and 5 nm. A filter wheel in front of the entrance slit of the first monochromator inserts an appropriate optical filter into the beam path depending on the wavelength to be produced, in order to filter out higher orders of the diffraction pattern. The monochromatized light then passes the common beam mask (CBM), which can be used to cut the light beam vertically according to sample size. We used the full vertical extension of the beam of about 13 millimeters. Because of the polarization-dependent reflectance of the optics in the beam path the originally unpolarized light is partially linearly polarized. A depolarizer[6] (Dp) is inserted into the beam path to randomize

---

[5] Air absorbs light of wavelengths below 200 nm, therefore the instrument is equipped with an installation to purge the beam path with a protective gas such as argon or nitrogen.

[6] An introduction to depolarizers can be found in [75].

the linear polarization across the cross section of the beam. The chopper wheel
(Ch) splits the beam into two beams, the sample beam and the reference beam.
The chopper wheel has four sections: a reflective section, an open section and
two dark sections in between, so that the light is alternately directed into
the sample and reference beam path. The dark sections serve to measure the
background noise of the detector (cf. Sec. 3.3.3). Both beams pass through an
attenuator stage (Att and Att', respectively) where each beam can optionally
be attenuated using a neutral-density filter (transmission of 10 or 1 %). They
can be used to reduce the light intensity ratio of sample and reference beam if
a highly absorbing sample is placed in one of the beam paths (cf. next section).
For polarization-dependent measurements, a coupled pair of linear polarizers[7]
(P1 and P1') can be inserted into the two beam paths in front of the sample
compartment. By default the sample compartment is equipped with an optics
board with one cell holder in the sample and reference beam, respectively. For
DR measurements we replaced this optics board with a custom-made one (cf.
Sec. 3.3.5). After passing the sample compartment both beams are reflected
onto the same photomultiplier (PM).

3.3.3 Measurement Principle

The current signal measured by the photomultiplier is converted to a voltage
signal, amplified, and passed onto an 8-bit analog-to-digital converter (ADC).
Because of this relatively low ADC resolution, the amplification of the analog
signal is variable: The input signal is repeatedly doubled until it is larger
than a reference value. Amplification factors between $2^1 = 2$ and $2^6 = 64$ are
possible. The amplified signal is converted to a digital value and then divided
by the amplification factor. This algorithm is performed separately for sample
and reference beam.

The thus gained signal intensities I_S and I_R in the sample and reference
beam are subtracted by their respective dark signals $I_{S,dark}$ and $I_{R,dark}$, and
the absorbance

$$A = -\lg(T) = -\lg\left(\frac{I_S - I_{S,dark}}{I_R - I_{R,dark}}\right) \tag{3.20}$$

is stored as the measurement result. Because of the limited dynamic range of
the ADC the intensity ratio between sample and reference should not exceed
about 2 orders of magnitude. This can be achieved by placing an appropriate
sample in the reference beam (see below) or by using the attenuators Att and
Att' (cf. Fig. 3.10).

When recording a spectrum, the rotation of the monochromator gratings
is synchronized with the rotation period of the chopper wheel, which is 20 ms.
In a typical wavelength scan (steps of ≤ 10 nm) the monochromator requires
20 ms to move to the next requested wavelength so that the minimum cycle
time is 40 ms. For longer integration times the measurements of several cycles
are averaged before moving to the next wavelength.

---

[7] The polarizer unit uses two Glan-Taylor prisms [75] which are rotated by a stepper motor.

3.3.4 Absorbance Spectroscopy

Because of the double beam setup it is in principle possible to determine the absorbance of a dye by placing a cell with the dye dissolved in a solvent in the sample beam and a cell with just the solvent in the reference beam. However, in such a measurement the obtained spectrum would unavoidably be distorted by minor differences in the alignment of the sample and reference beam. Therefore, the more practical method is to perform two separate measurements: First, a cell with just the solvent is placed in the sample beam and optionally another cell with the solvent is placed in the reference beam in case of solvents with strong absorption bands.[8] This *baseline* measurement yields the absorbance A_0. Second, the solvent in the sample beam is replaced by the dye solution, yielding the absorbance A_1. The absorbance of the dye is then

$$A_{\mathrm{dye}} = A_1 - A_0. \tag{3.21}$$

This way all differences in the sample and reference beam cancel out. Preferably, the *same* cell is used for the measurement of solvent and solution. Details of how absorbance spectroscopy was performed in this work are given in Sec. 9.3.

3.3.5 Differential Reflectance (DR) Spectroscopy

Differential reflectance (DR) spectroscopy is an optical technique in particular suitable for thin molecular films. This is because optical spectroscopy in general is non-destructive, can be applied *in situ* during film growth and because of the excitonic nature of the optical excitations in the film optical spectroscopy yields information on structural properties as well [61]. Often the substrate is opaque and therefore reflectance measurements are chosen over transmittance measurements. In the case of very thin films it is often difficult to make out the optical properties of the film since the reflectance is dominated by the substrate. Therefore, the reflectance R_1 of the film-covered substrate is compared with the reflectance R_0 of the uncovered surface [61, 76]:

$$\mathrm{DR} \equiv \frac{\Delta R}{R} = \frac{R_1 - R_0}{R_0} \tag{3.22}$$

It can be shown that for near-normal incidence and thin films ($d \ll \lambda$) the DR is approximately proportional to film thickness and the dielectric function of the absorbing material.

In this work we perform DR spectroscopy under an oblique angle of incidence which means that s- and p-polarized measurements let us gain insight into orientations of optical transition dipole moments (TDMs).

Experimental setup For DR measurements the sample compartment of the UV/vis spectrometer is equipped with a custom-made optics breadboard. A scheme of the setup is shown in Fig. 3.11. Sample and reference beam pass through the linear polarizers, P1 and P1', respectively. While the reference

---

[8] The attenuators (Att or Att', cf. Fig. 3.10) could also be used instead, but they have the disadvantage of attenuating the reference beam uniformly across the spectrum.
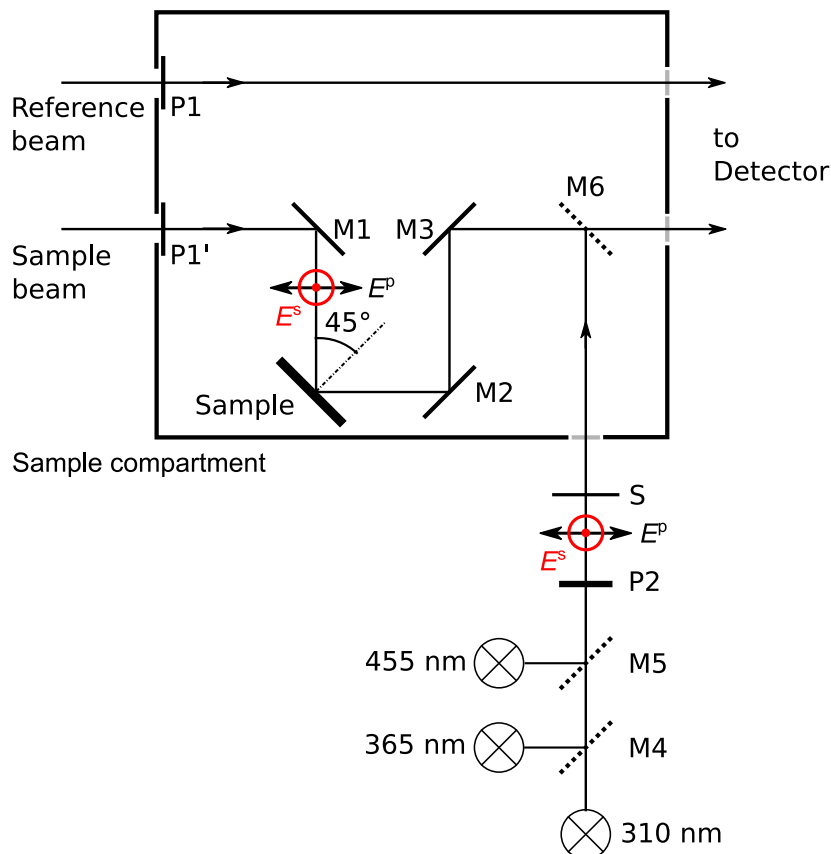
Figure 3.11: Scheme of the homebuilt Differential Reflectance (DR) spectroscopy setup. It consists of aluminum mirrors M1–M6, linear polarizers P1, P1' and P2, a motorized shutter S and three LED lamps (Thorlabs, cf. Tab. 9.3) with collimating lenses. The mirrors M4–M6 can be moved into or out of the beam path using motorized flip mounts. The linear polarizers P1, P1' and P2 can be set to s- or p-polarization. The angle of incidence on the sample is 45°.

beam is then passed directly through the sample compartment, the sample beam is guided across an aluminum mirror, the sample, and two more aluminum mirrors, with all angles of incidence being 45°.

For illuminating the sample with external light we used three different LEDs, each equipped with a collimating lens. The LEDs have central wavelengths of 455, 365, and 310 nm, respectively (for spectral characteristics see Tab. 9.3). The mirrors M4 and M5, installed onto motorized flip mounts, allow us to select a certain light source. The linear polarizer P2 is used to polarize the light: A motorized flip mount selects one of two wire grid polarizers (in horizontal or vertical orientation) for the light to pass through.

The mirror M6, installed on a motorized flip mount, allows to perform DR measurements and illumination with external light sequentially: If moved out of the sample beam path, the reflectance can be measured. If moved into the sample beam path, the path to the detector is blocked and the external light can illuminate the sample: The shutter S is opened and the external light hits the sample under an angle of incidence of 45°, i.e., at the same angle of incidence as the light used to measure the reflectance, but in opposite

direction.[9] S is closed before moving M6 into measurement position again.

The flip mounts and the shutter are controlled via transistor-transistor logic (TTL) signals with the two signal levels 'high' (2.6–5 V) and 'low' (0–0.8 V). The flipping of a mount is triggered by a high–low or low–high TTL signal change and the position of a flip mount is detected by a reed switch. The shutter is open (closed) if a high (low) signal is applied to its input. The intensity of the LED lamps is proportional to an analog input signal between 0 and 5 V, which is applied to the driver of each LED. The analog and digital signals are generated and detected by a Labjack U6 data acquisition device.

Measurement Principle In analogy to absorbance measurements, the measured quantity in a reflectance measurement is $= -\lg(I/I_0)$. Hereby I is the intensity in the sample beam after passing the three mirrors and the sample, whereas I_0 is the intensity of the reference beam which does not pass any additional optics (cf. Fig. 3.11). Therefore, I can be written as

$$I = I_0 \, R_{\mathrm{M}}^3 \, R_{\mathrm{Samp}}, \tag{3.23}$$

with R_{M} and R_{Samp} being the reflectance of one mirror and the sample, respectively. Thus, we obtain

$$-\lg\left(\frac{I}{I_0}\right) = -\lg\left(R_{\mathrm{M}}^3 \, R_{\mathrm{Samp}}\right). \tag{3.24}$$

In analogy to absorbance spectroscopy we also perform two measurements in DR spectroscopy: the baseline measurement with the bare gold substrate in the sample beam, and the sample measurement with the same sample after formation of the organic layer. Using R_1 as reflectance of the gold sample with SAM and R_0 as the reflectance of the bare gold sample, we can define the differential reflectance $-\Delta \lg(R)$:

$$\begin{aligned} -\Delta \lg(R) &= -\left[\lg\left(R_{\mathrm{M}}^3 \, R_1\right) - \lg\left(R_{\mathrm{M}}^3 \, R_0\right)\right] \\ &= -\left[\lg\left(R_1\right) - \lg\left(R_0\right)\right] \end{aligned} \tag{3.25}$$

In this expression the reflectances of the mirrors cancel out and the quantity $-\Delta \lg(R)$ denotes the change in reflectance R of the gold layer due to the formation of the SAM on the surface. By Taylor expansion of (3.25) at R_0 (i.e., for small changes) we obtain

$$-\Delta \lg(R) \approx -\frac{R_1 - R_0}{R_0} \equiv -\frac{\Delta R}{R}, \tag{3.26}$$

which is identical to the definition (3.22) found in literature.

Reflectance Spectra of SAMs on Gold Fig. 3.12 shows an exemplary reflectance spectrum of a gold substrate, a reflectance spectrum of the gold substrate covered by an Az11 SAM, and the resulting differential reflectance spectrum. The reflectance spectra $-\lg(I/I_0)$ are dominated by the optical

---

[9] This design avoids exposing the PM to the external light, which is several orders of magnitude more intense than the light of the spectrometer lamps.
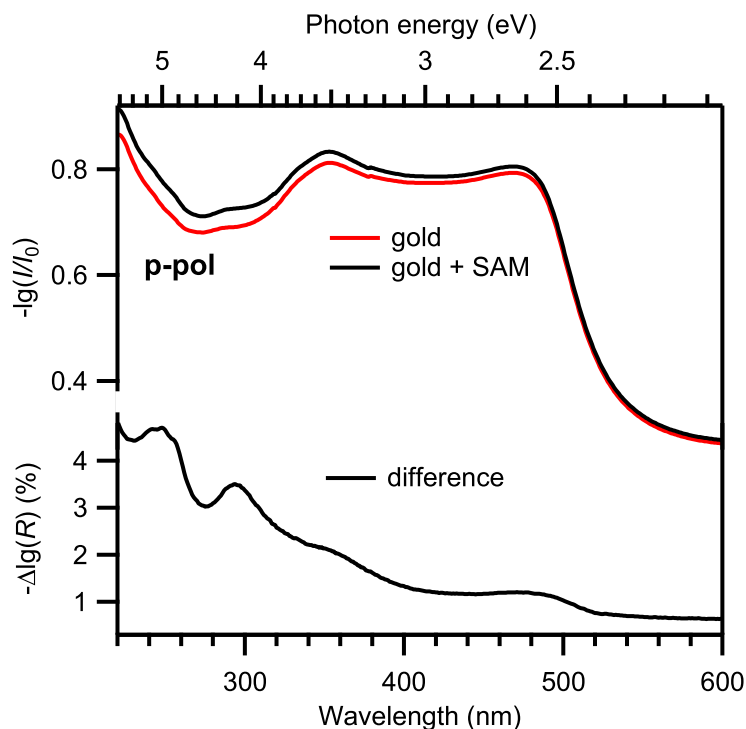
Figure 3.12: Reflectance spectra measured with p-polarized light: a gold/mica sample without and with an Az11 SAM (top), and the obtained DR spectrum (bottom).

properties of the gold sample since the reflectance of the aluminum mirrors used in the setup is between 75 and 90 % in the UV/vis spectral range.[10] The values $-\lg(I/I_0)$ of the SAM-covered gold are bigger than the ones of the bare gold substrate across the whole spectrum, which means that the formation of the SAM reduces the reflectance of the surface.[11] The steep increase in $-\lg(I/I_0)$ below $\approx 520\,\text{nm}$ (above $\approx 2.4\,\text{eV}$) originates from interband absorption from the d- into the sp-bands of gold.[12]

The differential reflectance $-\Delta\lg(R)$ is on the order of few percent only. This means that even subtle differences between different gold substrate pieces of the same batch play a role, i.e., DR spectra are only meaningful when obtained for the very same sample before and after SAM formation. The dominating features in the difference spectrum are the signal increase at 520 nm due to the aforementioned interband absorption of gold and peaks at about 300 nm, which originate from absorption bands of azobenzene (see Chap. 6).

---

[10] Mirror optimized for the UV spectral range, Art. No. G340 302 000, Qiopticq, https://www.qioptiq-shop.com.

[11] The sign of DR spectra depends on the optical properties of substrate *and* adlayer, and for some systems the sign may also change within the spectrum [61].

[12] See [77] and citations therein.

Chapter 4

Composition of *trans*-Az11 SAMs

In this work we examined the structure, optical properties and photoisomerization in SAMs of the azobenzene-functionalized alkanethiol Az11 and the simple alkanethiol C12 (Fig. 2.8). C12 is incorporated into the molecular layer since densely-packed SAMs of azobenzene-alkanethiols show little to no photoisomerization (see Sec. 2.2). The SAMs are prepared by coadsorption from a mixed solution of both thiols. The quality and the composition of the SAMs are examined by XPS: First, we verified the chemical purity of the thiolate–gold bond, i.e., we checked that no unbound thiol or other sulfur species are on the surface. Second, we determined the composition of the SAMs, i.e., the amount of Az11 on the surface in dependence on the mole fraction of Az11 in the incubation solution. Experimental details to the XPS measurements are given in Sec. 9.4.1.

4.1   Sample Preparation

In Sec. 2.2 a general overview to the preparation of SAMs is given. In this work single-component and mixed Az11/C12 SAMs were prepared in the following way: The gold substrates were immersed in a solution of the desired thiol(s) at room temperature for 20 hours in order to obtain a well-ordered SAM. Afterwards, the samples were rinsed with pure solvent and blown dry with nitrogen.

Two different kinds of substrates were used: samples of mica sheets with a thin layer of gold (thickness of 300 nm) and gold single crystals.[1] Both exhibit the (111) face with the herringbone surface reconstruction.

The adsorption solutions were prepared by dissolving the compounds Az11 and C12 in methanol, respectively, and mixing appropriate amounts of the solutions with additional solvent, attaining a total thiol concentration of 0.1 mM.

Details on the preparation are given in Sec. 9.2.

---

[1] Gold on mica was used for most of the experiments. Gold single crystals were used for photoisomerization experiments in vacuum because they have a better coupling to the cryostat than gold on mica.

Figure 4.1: Exemplary S 2p XP spectrum of a SAM on gold with unwanted impurities. The spectrum was normalized to the background on the low-energy side. The two Voigt doublets used in the fit are displayed on the bottom. The doublet at 162.0 eV (black line) is attributed to the alkylthiolate species, i.e., alkylthiols bound to gold. The doublet at 161.0 eV (red line), which makes up about 10 % of the total peak area, is unwanted and attributed to atomic sulfur. Typical spectra do not contain this peak doublet (see Fig. 4.2a). All peak parameters are given in Tab. B.1.
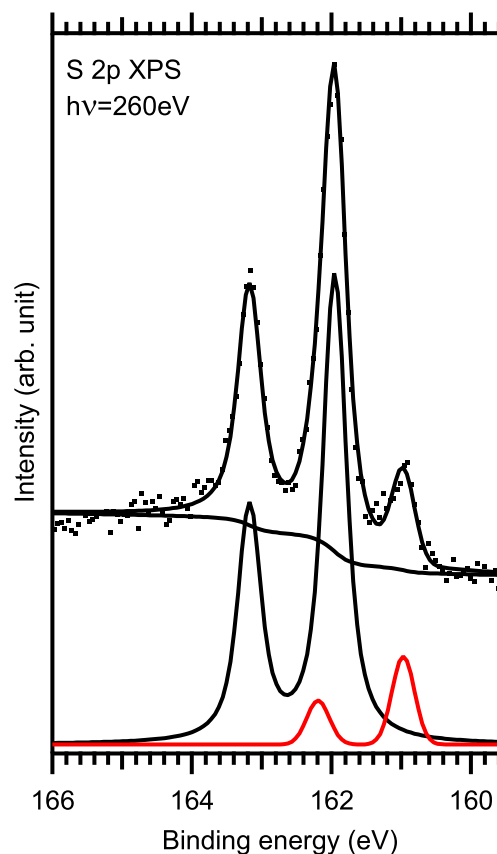
4.2 Chemical Purity of the Thiolate–Gold Bond

XPS can be used to quantitatively analyze different oxidative states of sulfur in SAMs. In a well-prepared SAM, the thiolate, i.e., the thiol bound covalently to gold, is the only species we expect to be present.

Fig. 4.1 shows S 2p XP spectra of an Az11 SAM on gold. As explained in Sec. 3.1.3, a doublet is expected for XPS on the 2p level. We observe two doublets: a doublet with a $2p_{3/2}$ peak at 162 eV and a smaller doublet with a $2p_{3/2}$ peak at 161 eV. The main doublet is attributed to the thiolate [78], i.e., the desired species. The smaller doublet at 161 eV is commonly assigned to atomic sulfur[2], or thiolates at different binding sites [80, 81]. A discussion on the assignment of the doublet at 161 eV can be found in [29, p. 18]. When comparing the area of the doublet at 161 eV with the sum of areas of both doublets, we find that about 10 % of the sulfur atoms is of the unwanted species. In other samples examined in this work no other S 2p doublet except the one attributed to the thiolate were present (see next section). A third doublet at 163–164 eV, which is commonly assigned to unbound thiol or disulfide [82], is not observed in our measurements.
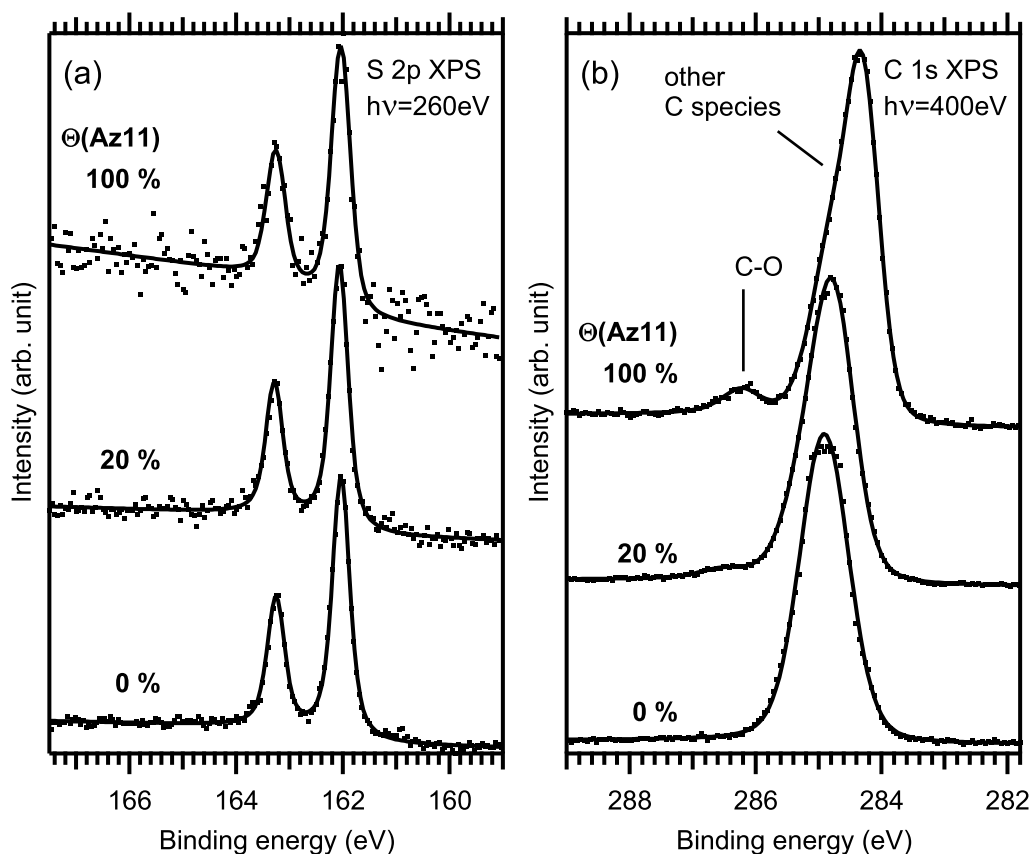
Figure 4.2: XP spectra of mixed Az11/C12 SAMs with different Az11 coverages Θ. (a): S 2p spectra, normalized to total peak area. Each spectrum was fitted with one doublet of Voigt peaks. (b): C 1s spectra, normalized to the background on the low-energy side. The 100 % and the 20 % Az11 SAM were fitted with three Voigt peaks and the 0 % Az11 (pure C12) SAM were fitted with one Voigt peak. All peak parameters are given in Tab. B.2. Assignments see text.

4.3 Composition of Mixed Az11/C12 SAMs

4.3.1 Signatures of Az11 and C12 in XP Spectra

In order to identify the signatures of Az11 and C12 in SAMs we performed XPS at the S 2p, C 1s, N 1s and O 1s edges. As shown in Sec. 2.2, the amount of Az11 in mixed Az11/C12 SAMs can be quantified in terms of the relative Az11 coverage Θ(Az11), which is the number of Az11 molecules in a mixed SAM divided by the number of Az11 molecules in a single-component Az11 SAM (Eq. 2.29). We examined samples with relative surface coverages Θ(Az11) of 100 %, 20 %, and 0 % (C12 only). The value Θ in the mixed SAM was estimated from the mole fraction of Az11 in its incubation solution according to a quantitative XPS analysis described in the next subsection (4.3.2).

S 2p Fig. 4.2a shows S 2p spectra. They all exhibit the one doublet assigned to the thiolate species. The concentration of impurities such as atomic sulfur or unbound thiols is lower than approximately 3 %. Because of the sulfur atom being at the very bottom of the molecular layer, the photoelectrons have

---

[2] See [79] and citations therein.
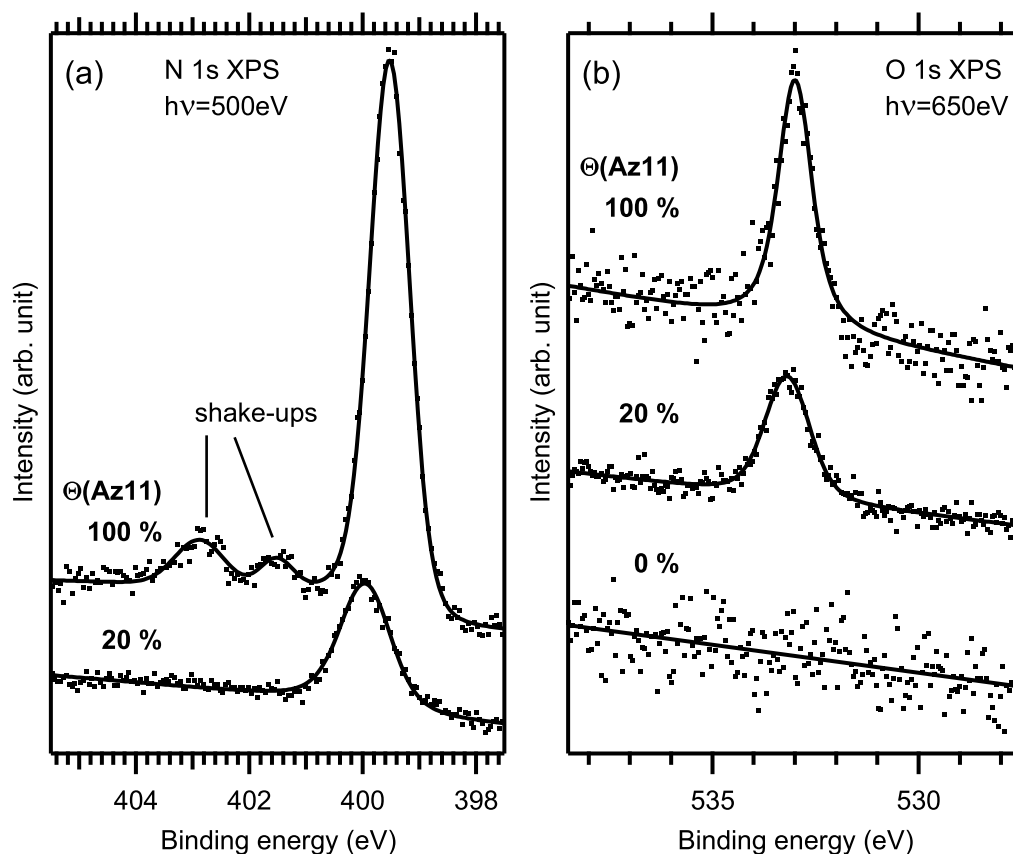
Figure 4.3: XP spectra of mixed Az11/C12 SAMs with different Az11 coverages Θ, normalized to the background on the low-energy side. (a): N 1s spectra. The spectrum and the analysis of the 100 % Az11 SAM is identical to Fig. 3.3. (b): O 1s spectra. All peak parameters are given in Tab. B.2.

to pass through the layer in order to be detected. Since the Az11 molecule is longer than the C12 molecule, the scattering of the S 2p photoelectrons is increasing with increasing Az11 content, leading to a decreasing signal-to-background ratio. Therefore, the S 2p spectra (which were all recorded with the same measurement time) were normalized to the total doublet area.

C 1s   The C 1s spectra (Fig. 4.2b) exhibit one main peak and a small peak on the high binding-energy side, which is only present in the Az11-containing SAMs and decreases in intensity with Az11 coverage. In the Az11-containing SAMs the main peak can be reproduced well with two Voigt peaks, where the lower binding-energy component is assigned to carbon in the phenyl rings and the higher binding-energy component is assigned to carbon in the alkyl chain and carbon bound to the N=N bridge. The small peak is attributed to carbon bound to oxygen and was fitted with one Voigt profile. Assignments were made according to [83]. The spectrum of the C12 SAM was fitted with one Voigt profile.

N 1s   In Fig. 4.3a N 1s spectra are shown. Since in *trans*-Az11 the two nitrogen atoms are (nearly) equivalent, the spectra are well-described by a single Voigt peak. For the 100 % Az11 SAM we observe two shake-ups. The peak area decreases in intensity with decreasing Az11 content as expected.

Figure 4.4: Relative Az11 coverage Θ in Az11/C12 SAMs versus mole fraction χ^{sol} of Az11 in incubation solution. The dashed line represents ideal mixing. Data points above the line indicate preferential adsorption of Az11. Adopted from [48].
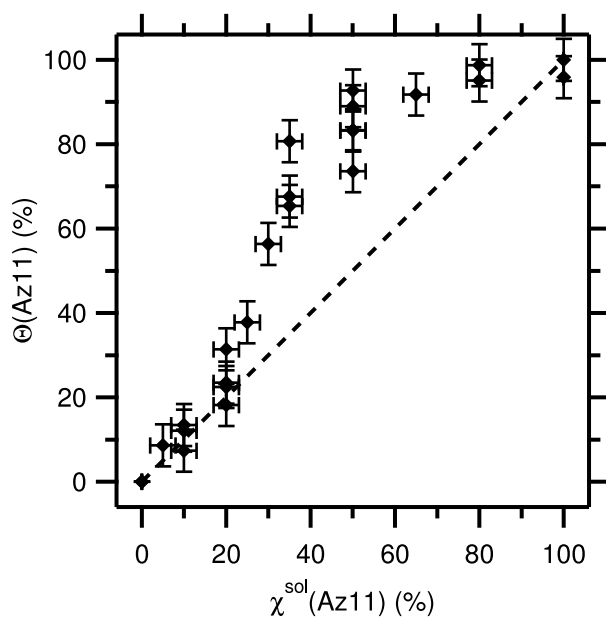
The difference in N 1s binding energy in the 100 and 20 % Az11 SAM is not coincidental: In a series of measurements it was found that the N 1s peak continuously shifts to higher binding energy for decreasing Az11 content, which indicates a nearly statistical mixing of Az11 and C12 on the surface [48].

O 1s O 1s spectra are shown in Fig. 4.3b. Since Az11 has only one oxygen atom, the O 1s spectra of azobenzene-containing SAMs could be fitted with a single Voigt profile. A decrease of signal for decreasing Az11 coverage is observed and the pure C12 SAM does not contain any oxygen as expected.

4.3.2   Quantifying the Amount of Az11

In order to determine the relative Az11 coverage $\Theta(\text{Az11})$ in mixed Az11/C12 SAMs in dependence on the mole fraction $\chi^{\text{sol}}_{\text{Az11}}$ of Az11 in the incubation solution, my colleague D. Przyrembel performed and analyzed N 1s XPS measurements of mixed Az11/C12 SAMs [48]. Since nitrogen is only present in Az11, the N 1s peak area in XP spectra is proportional to the number of Az11 molecules in the SAM. Therefore, the N 1s peak area of a mixed Az11/C12 SAM divided by the N 1s peak area of a single-component Az11 SAM then gives $\Theta(\text{Az11})$. The C12 molecule has no unique chemical signature and its amount on the surface cannot be determined independently.

The resulting relative Az11 coverage Θ as a function of the mole fraction $\chi^{\text{sol}}_{\text{Az11}}$ of Az11 in the incubation solution is shown in Fig. 4.4. For $\chi^{\text{sol}}_{\text{Az11}}$ below approx. 20 %, Θ is proportional to $\chi^{\text{sol}}_{\text{Az11}}$. For higher $\chi^{\text{sol}}_{\text{Az11}}$, Az11 is adsorbed preferably. This indicates that the interaction of an Az11 molecule with another Az11 molecule is bigger than the interaction of an Az11 molecule with a C12 molecule. The van der Waals interaction of C12 with neighboring C12 or Az11 should be very similar because the length of the aliphatic chains is nearly the same. In contrast, two neighboring Az11 molecules should interact more strongly due to additional π–π interactions of the chromophores. This likely leads to the observed preferential adsorption of Az11. However, a full

displacement of C12 by Az11 is not observed. The following effects counteract the preferential adsorption of Az11: Since C12 has a smaller footprint than Az11, exchanging C12 for Az11 results in a gain of total adsorption energy. Also, the displacement of one species by the other lowers the entropy and is therefore not favored.

4.4   Conclusions

Using XPS, we analyzed the chemical composition of Az11 SAMs. Sulfur XP spectra demonstrate that only the thiolate species is present, i.e., the concentration of impurities such as atomic sulfur or unbound thiols is lower than approximately 3 %. XP spectra at the C 1s, N 1s and O 1s levels illustrate how the chemical composition changes with varying amounts of Az11 in the SAM. A quantitative analysis of N 1s XPS finally allowed us to examine how the amount of Az11 in the SAM depends on the mole fraction of Az11 in the incubation solution. A preferential adsorption of Az11 is observed, likely due to strong van der Waals interactions between the azobenzene moieties. But yet, Az11 and C12 mix nearly statistical in the SAM.

Chapter 5

Structure of *trans*-Az11 SAMs

In the previous chapter we examined the chemical structure of mixed Az11/C12 SAMs. In this chapter we discuss in how far the orientation of the *trans*-azobenzene chromophores within the SAMs depends on their concentration. This is done by NEXAFS at the C 1s and the N 1s edges. We use the polarization contrast in the 1s→$\pi^\star$ (LUMO) excitation to determine the orientation of the phenyl rings of the chromophore (see Sec. 3.2.7).

5.1 C 1s NEXAFS Spectra

Fig. 5.1 shows C1s NEXAFS spectra of SAMs with varying Az11 coverage Θ. First we look at the single-component C12-SAM (0 % Az11). The prominent peaks at 287.8 eV and 293.0 eV are commonly interpreted as $\sigma^\star$(C-H) and $\sigma^\star$(C-C) resonances in the alkyl chain, respectively [67, 84]. Additionally we observe a sharp peak at 286.7 eV in the spectra measured with p-polarized light, this may be attributed to the CH_3 group of the C12 molecule.[1] For SAMs containing Az11, additional absorption structures appear at photon energies of 284 to 286 eV. They are core excitations into $\pi^\star$ states of the aromatic rings, namely the LUMO, LUMO+1 and LUMO+2 states [18].

The intensities of the $\pi^\star$ excitations for the different SAMs vary greatly with the Az11 coverage Θ: Overall, the intensity of the $\pi^\star$ core excitations increases with the Az11 coverage since the $\pi^\star$ core excitations stem from the phenyl rings of the azobenzene moieties. But we also observe changes in the intensity ratios between spectra measured with s- or p-polarized X-ray light: In the case of the SAM with low Az11 coverage (15 %), the $\pi^\star$ excitations measured with p-polarized light have a much higher intensity than the ones measured with s-polarized light. In the case of the 80 % Az11 SAM the intensity is the same for all X-ray polarizations and for the pure Az11 SAM the peak intensity measured with s-polarized light is now significantly higher than the one measured with p-polarized light. This is a clear indication that the orientation of the $\pi^\star$ orbital changes upon increasing the density of chromophores. This will be quantified in Sec. 5.3.

When looking at the $\sigma^\star$ resonances, we find that they are very intense in

---

[1] In two-photon photoelectron spectroscopy (2PPE) experiments on a C12 SAM, a delocalized state was observed at the SAM–vacuum interface [85], maybe this corresponds to the peak observed in NEXAFS.

Figure 5.1: C 1s NEXAFS spectra of SAMs with varying Az11 coverage Θ for p-polarized light, and light polarized along the magic angle. The peaks at $288.0\,\text{eV}$ and $293.0\,\text{eV}$ are commonly interpreted as $\sigma^\star(\text{C-H})$ and $\sigma^\star(\text{C-C})$ resonances, respectively. The sharp feature (†) at $286.8\,\text{eV}$, visible in the p-polarized spectra of low-Θ-SAMs, is believed to originate from the CH_3 group of the C12 molecule (see text). For SAMs containing Az11, the first absorption structures already appear at photon energies of 284 to $286\,\text{eV}$, they are assigned to $\pi^\star$ orbitals. Figure adopted from [48, Supporting Information].
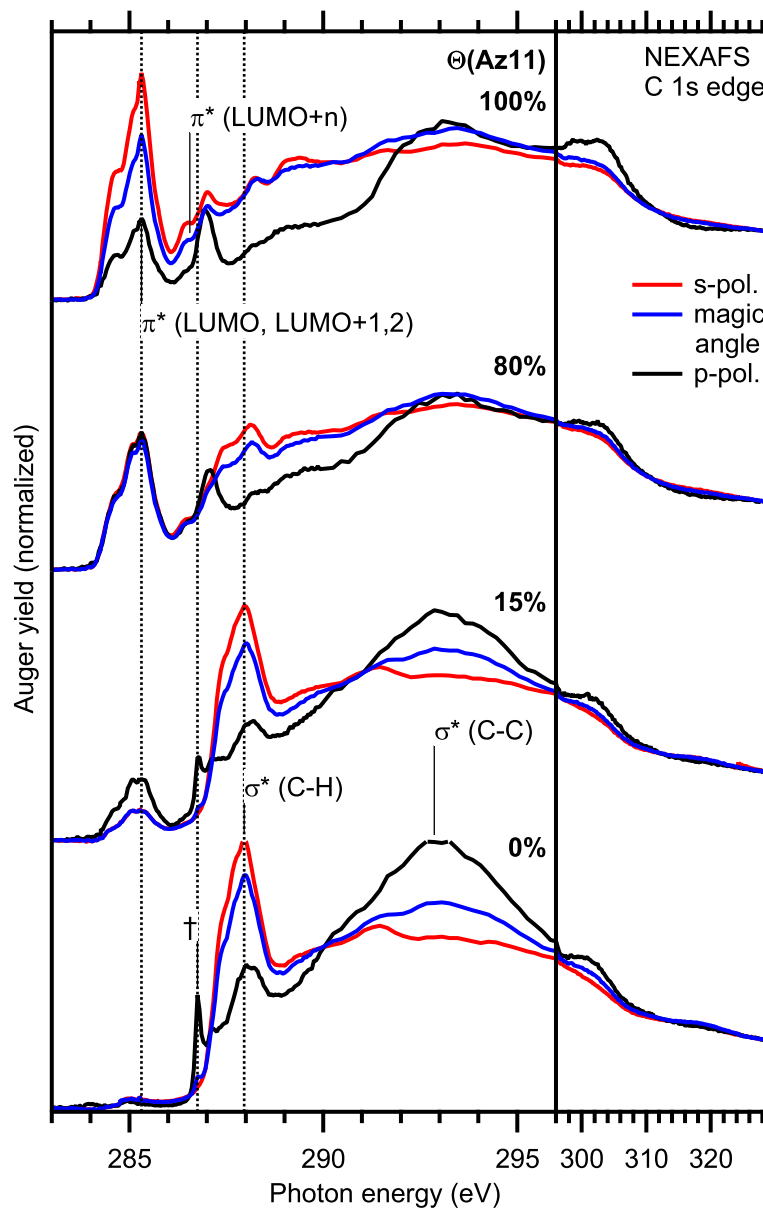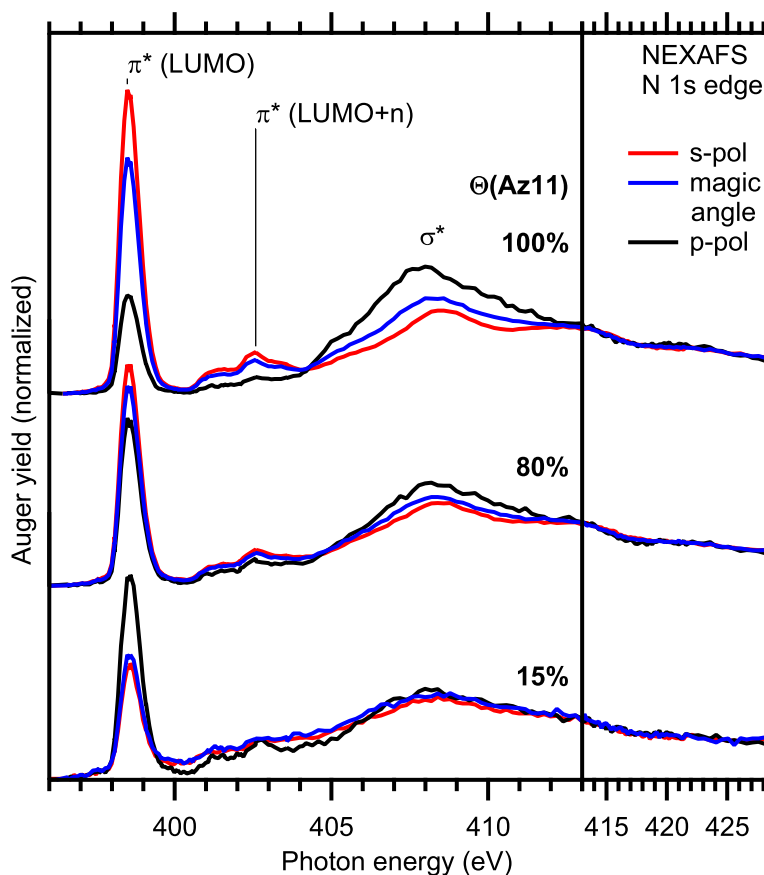
Figure 5.2: N1s NEXAFS of SAMs with varying Az11 coverage Θ, for s- and p-polarized light, and light polarized along the magic angle. The peak at about $398\,\mathrm{eV}$ originates from the excitation into the $\pi^\star$ (LUMO) orbital, whereas the peaks in the [400,403] eV range are assigned to excitations into higher unoccupied $\pi^\star$ orbitals. The broad feature around $407\,\mathrm{eV}$ is a $\sigma^\star$ resonance. Figure adopted from [48].

case of the C12 SAM but decreased in intensity for higher Az11 coverages. This effect can be explained by the $\sigma^\star$ resonances being dampened by the phenyl rings of the chromophores, which stick out of the layer of alkanethiol linkers.

5.2 N 1s NEXAFS Spectra

Fig. 5.2 shows N 1s spectra of SAMs with varying Az11 coverage Θ. We observe the prominent 1s$\to\pi^\star$ (LUMO) excitation at about $398\,\mathrm{eV}$, higher $\pi^\star$ excitations at energies up to $403\,\mathrm{eV}$, and the first $\sigma^\star$ resonance at about $408\,\mathrm{eV}$, in accordance with earlier work for a similar molecule [18]. The intensity of all peaks increases with the Az11 coverage because nitrogen is only present in the azo group.

Additionally we observe that the polarization contrast of the $\pi^\star$ (LUMO) excitation changes with increasing Az11 coverage: For the 15 % Az11 SAM the peak intensity measured with p-polarized light is the highest, for the 80 % Az11 SAM the peak intensity measured with s-polarized light is already higher than the one measured with p-polarized light, and this ratio increases significantly for the pure Az11 SAM. This behavior is analogous to the observations in the C 1s spectra and indicates a significant change of chromophore orientation

Figure 5.3: A schematic of the orientation of azobenzene units with respect to the surface. α denotes the angle between the surface normal $\vec{n}$ and the normal to the plane of the phenyl rings (gray area). The transition dipole moment (TDM) of the 1s→$\pi^\star$ excitation is parallel to this normal. θ denotes the angle between the surface normal and the long axis of the azobenzene moiety.
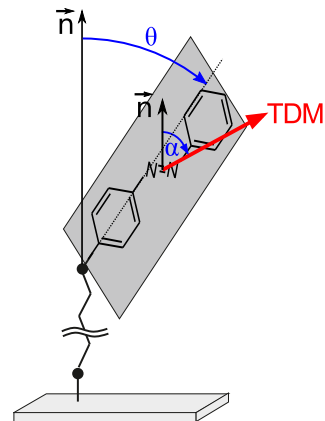
Table 5.1: Average orientations α in SAMs of varying Az11 coverage Θ, determined from C 1s and N 1s spectra (cf. Figs. 5.1 and 5.2). The errors given include systematic contributions and sample-to-sample variations. Taken from [48].

Θ_{Az11} (%)	α (deg)	
	C 1s	N 1s
100	71 ± 5	73 ± 5
80	55 ± 5	59 ± 5
15	42 ± 5	45 ± 5

with chromophore density. As with the C 1s spectra, this polarization contrast can be exploited to determine the average orientation of the phenyl rings of the azo group (see next section).

5.3   Orientation of Chromophores

The orientation of chromophores is determined in terms of two angles: θ, the angle between the surface normal and the long axis of the azobenzene moiety, and α, the angle between the surface normal and the normal of the phenyl rings (see Fig. 5.3). The transition dipole moment (TDM) of the $\pi^\star$ excitation is parallel to this normal. Therefore the angle α can be determined by evaluating the polarization contrast of the $\pi^\star$ excitations in the C 1s and N 1s NEXAFS spectra (see Sec. 3.2.7).

Tab. 5.1 shows the resulting average angles α deduced from the C 1s and N 1s to $\pi^\star$ (LUMO) excitations. They agree with each other and they significantly decrease with decreasing Az11 coverage. This indicates a significant change of chromophore orientation. The angle α determined for the single-component Az11 SAM also agrees well with the ones in SAMs of CN- or CF$_3$-functionalized azobenzene-alkanethiols, where also the angle θ between the long axis of the azobenzene moiety and the surface normal could be determined [86]. For these measurements an average angle θ of about 30° had been obtained. The observed change in α for decreasing Az11 coverage Θ should coincide with a "bending down" of the azobenzene moieties, i.e., an increasing angle θ.

Note that we determine only the *average* orientation of the SAM: In the NEXAFS measurements the signal originates from a macroscopic area of the sample. The results from XPS [48] indicate that the two thiol species Az11 and C12 mix nearly statistically on the surface, i.e., azobenzene moieties at different sites may have a different number of neighbors and thus also different

chromophore orientations.

5.4 Conclusions

We examined the average chromophore orientation in single-component *trans*-Az11 SAMs and mixed *trans*-Az11/C12 SAMs. Since Az11 and C12 mix nearly statistically on the surface and we integrate over a macroscopic area of the sample, only the average orientation of the chromophores could be obtained. In a densely packed *trans*-Az11 SAM the chromophores are standing predominantly upright. Upon diluting the chromophores with C12 spacers the average angle α decreases significantly, which implicates a more flat-lying orientation of the chromophores in average. It could be shown that even a minor dilution to $\Theta = 80\,\%$ already leads to a significant decrease in α.

In Sec. 7.2.1 we examine the photoisomerization of Az11-containing SAMs using NEXAFS.

Chapter 6

Optical Properties of *trans*-Az11 SAMs

The optical properties of SAMs are governed by the absorption characteristics of the molecules, in particular delocalized molecular excitons, and by the transmission and reflection of light at the air/SAM and SAM/metal interfaces, as described by the Fresnel equations. We use differential reflectance (DR) spectroscopy to examine the optical properties of SAMs. Analyzing the optical properties is in particular important to understand the photoisomerization in SAMs (see Chap. 7).

6.1 Qualitative Description of DR Spectra

Single-Component Az11 SAM Fig. 6.1 shows differential reflectance (DR) spectra of a $100\,\%$ Az11 SAM, measured with p- and s-polarized light, respectively, under an angle of incidence of 45°. An absorbance spectrum of *trans*-Az11 in solution is added for comparison.

Below approx. $2.7\,\text{eV}$ a step of the DR signal is visible due to the onset of the d-bands in the absorption spectrum of gold (see Fig. 3.12). The first optical transition in azobenzenes, the S_1 band, is not visible in the DR spectra of the SAM, since it is only weakly allowed.

The S_2 band in the spectral region of 3–$4.5\,\text{eV}$ is very different in the Az11 SAM and in the Az11 solution: Whereas in the absorbance spectrum of Az11 in solution the maximum of the S_2 band appears at about $3.6\,\text{eV}$, the DR spectrum of the Az11 SAM taken with p-polarized light exhibits a pronounced peak at about $4.2\,\text{eV}$ and a weak peak at about $3.5\,\text{eV}$. The spectrum taken with s-polarized light is relatively flat, with small peaks at 3.8 and $3.5\,\text{eV}$, respectively.

As described in Sec. 2.3.1, for a molecular crystal with two molecules per unit cell (as it is the case for azobenzene-alkanethiol SAMs, see Sec. 2.2), one can expect an H-band and a J-band with non-negligible oscillator strength. Since the transition dipole moment (TDM) of the S_2 transition in azobenzene is oriented approximately parallel to the long axis of the azobenzene moiety (see Fig. 6.2) and the molecule is mostly standing upright (see Sec. 5.3), we can expect the H-band to be dominating, whereas the J-band should be weak. Both appears to be visible in the spectrum taken with p-polarized light: the
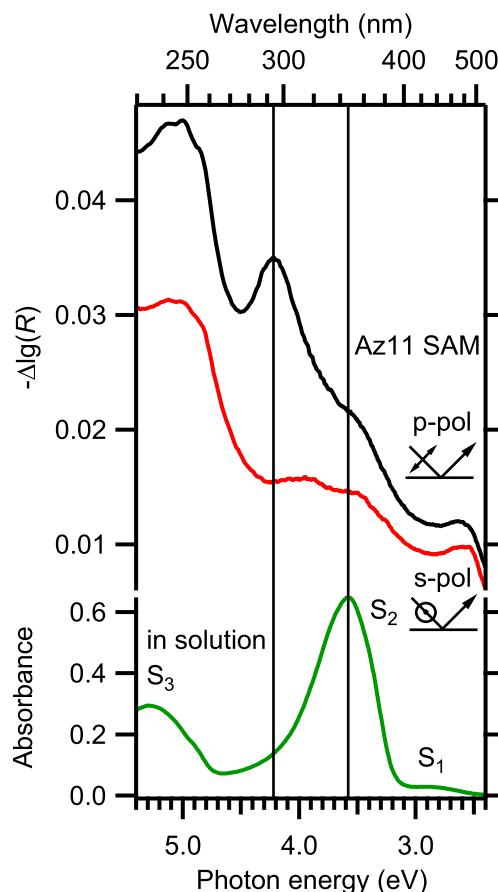
Figure 6.1: DR spectra of a 100 % Az11 SAM measured with s- and p-polarized light, respectively, under an angle of incidence of 45° (top), in comparison with the absorbance of an Az11 solution (bottom).
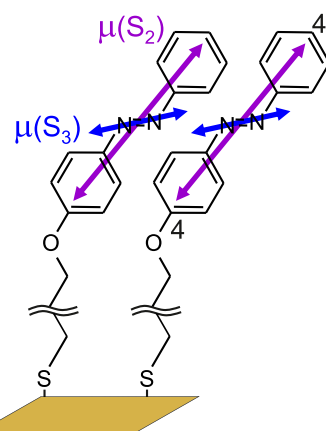
Figure 6.2: Orientation of transition dipole moments (TDMs) μ of the S_2 and S_3 transitions of Az11 according to [18].

maximum of the band (4.2 eV) may be attributed to the H-band and the small peak at 3.5 eV is attributed to the J-band. The H-band is shifted by about 0.6 eV with respect to the S_2 band of the single molecule (3.6 eV). In agreement with its TDM being oriented mostly perpendicular to the surface, the H-band peak at 4.2 eV is mainly visible in the spectrum taken with p-polarized light, because only p-polarized light has an electric field component perpendicular to the surface. Since the TDM of the J-band is rather parallel to the surface, it is observed with s- and p-polarized light. The excitonic nature of the S_2 band in Az11 SAMs is discussed in more detail in Sec. 6.2.

Above 4.5 eV in the DR spectra of the SAM the S_3 band is observed. It is shifted towards lower photon energies with respect to the band in the free Az11,

which indicates a J-band.[1] A peak fine structure is visible in the DR spectra, whereas in the free molecule the S_3 band is featureless. Since vibrational excitations are suppressed in J-bands [87], we attribute the peaks to a fine structure in the electronic transitions. In contrast to the S_2 band, the S_3 band shows relatively little polarization contrast. In the free molecule its TDM lies approximately parallel to the N=N bond (see Fig. 6.2). We therefore conclude that its TDM (and therefore the N=N bond) is oriented at an oblique angle with respect to the surface normal.

Mixed Az11/C12 SAMs Changing the density of azobenzene chromophores in the SAM has strong impact not only on the average chromophore orientation (Sec. 5.3) but also on the optical properties of the SAMs: Fig. 6.3 shows DR spectra of undiluted and diluted Az11 SAMs measured with p-polarized (top) and s-polarized (bottom) light in comparison with the absorbance of Az11 in solution (middle). With decreasing Az11 coverage Θ the DR signal generally decreases in both polarizations. This is expected since the absorption behavior of Az11 is a significant contribution to the DR signal. We also find that the H-band of the S_2 excitation visible in the spectra taken with p-polarized light shifts towards lower photon energies, i.e., a decreasing blue-shift. Additionally, the center of the S_3 band shifts towards higher energies in both polarizations, appearing to approach the band position of the free molecule, i.e., a decreasing red-shift is observed. Both indicates that the excitonic coupling reduces gradually with the Az11 coverage.

This can be attributed to two effects: First, the decreasing chromophore density reduces the width of the exciton band directly (see Sec. 2.3.1). Second, from NEXAFS we know that the chromophores tend to be oriented more parallel to the surface with decreasing Az11 coverage (Chap. 5). This change in average orientation also results in a reduced exciton bandwidth, as illustrated for a linear chain of molecules, where the angle between the molecular axis and the axis of the linear chain is decreased [55]. The continuous shifts of the maxima of the S_2 and S_3 bands corroborate that Az11 and C12 mix nearly statistically in the SAM, which was already concluded from XPS (see Sec. 4.3). Statistical mixing also means, that the chromophore densities are locally different, therefore we expect that the DR spectrum of a mixed SAM is a superposition of excitonic bands of different spectral widths.

The J-band of the S_2 transition (about 3.6 eV in the densely-packed SAM), appears to shift insignificantly with the Az11 coverage, which is because its red-shift with respect to the S_2 band of the free molecule is minor in the first place.

Note that the DR spectra of the SAM with $\Theta = 0$ (pure C12 SAM) show a small peak at 3.6 eV as well. The exact origin of the peak is unknown.[2] It might be related to an optical transition at the sulfur/gold interface.

---

[1] A H-band might be present as well but would lie outside the spectral window.
[2] The possibility of the "C12 SAM" actually still containing Az11, for example because of errors in the sample preparation, can be excluded since a sample produced in the same incubation solution was examined in XPS and no sign of nitrogen or oxygen was found.
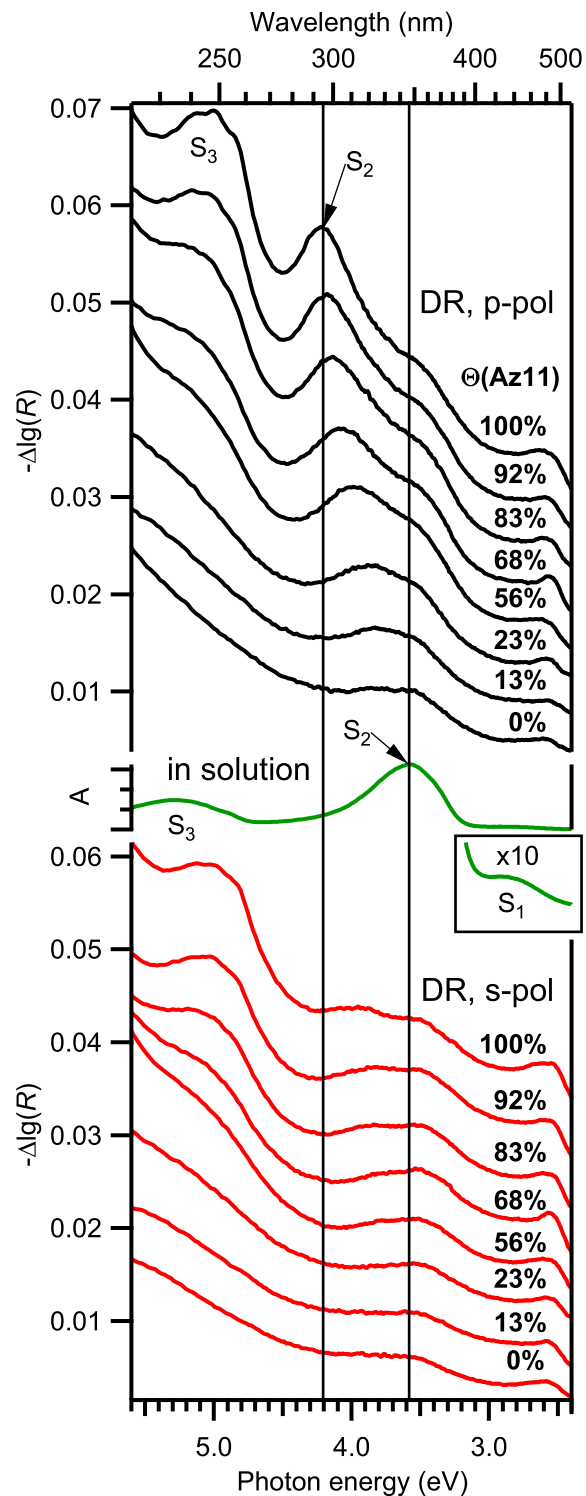
Figure 6.3: A series of DR spectra of Az11 SAMs with different coverages Θ, measured with p- and s-polarized light (top and bottom part, respectively, offsets were added) in comparison with an absorbance spectrum of *trans*-Az11 in methanol (middle part). The inset shows the upscaled S_1 absorption band in the absorbance spectrum. The S_2 band in spectra taken with p-polarized light shows a hypsochromic shift due to excitonic coupling. The coupling is weaker for higher diluted SAMs.
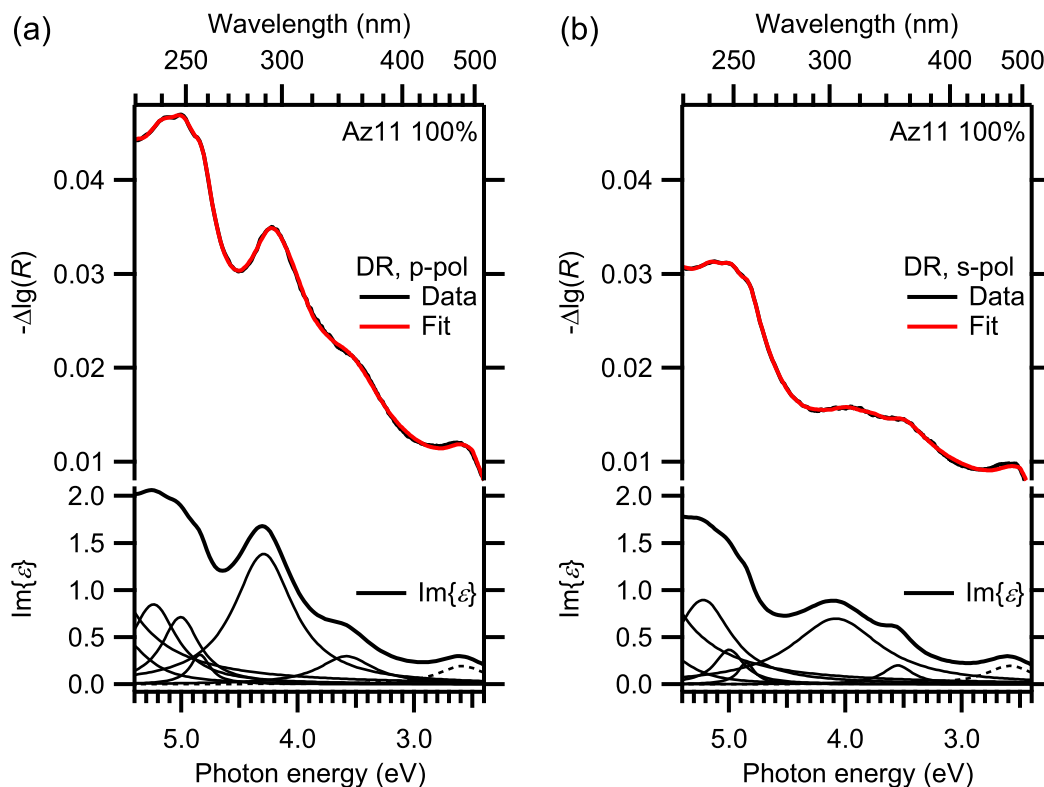
Figure 6.4: DR spectroscopy on a 100 % Az11 SAM measured with light of (a) p-polarization, (b) s-polarization. Top: DR spectra. Bottom: imaginary part of the dielectric function ϵ of the SAM. The lowest-energy peak at about 2.6 eV (dashed line) is attributed to an artifact (see text). All peak parameters are given in Tab. B.3.

6.2 Modeling of DR Spectra

DR spectra are not directly representing the absorption of the molecular film but is strongly influenced by the interfaces air/SAM and SAM/gold.[3] Additionally, the absorption properties of the molecules are altered by excitonic coupling. To disentangle these contributions, the DR spectra are modeled by describing the SAM as a homogeneous dielectric layer of thickness[4] $d = 2$ nm and complex dielectric function ϵ_2 with a set of Lorentzian absorption lines (see Sec. 2.3.2.3). The multiple reflections and transmissions of the light within the layer are calculated according to Sec. 2.3.2.2. The complex index of refraction of the gold substrate is taken from literature [77]. Spectra measured with p- and s-polarized light were fit independently, with the dielectric function of the film containing up to 8 Lorentz oscillators. Details of the fitting are given in Sec. 9.5.2.

Densely-Packed Az11 SAM In Fig. 6.4 DR spectra of a 100 % Az11 SAM, measured with p- and s-polarized light ((a) and (b), respectively) and their fits are shown (top), together with the imaginary part of the calculated dielectric

---

[3] The thermal stability of the *cis* isomer in SAMs indicates the presence of adsorbed water on the SAM under ambient conditions (cf. Sec. 7.2.2), this is neglected here.

[4] This thickness is reasonable considering the bond lengths [88, Sec. 9] of the molecule and its approximate orientation [18].

function ϵ of the film (bottom). The lowest-energy oscillator at about 2.6 eV (480 nm) is not attributed to Az11[5] but to artifacts caused by minor changes in sample position or orientation in the consecutive sample and reference measurement. Such changes have a large effect since in that photon energy range the reflectance of gold changes significantly due to the onset of the d bands (see page 51). As mentioned in the previous section, the S_1 peak is very weak in *trans*-Az11 SAMs and is omitted in the fits. The spectral region of the S_2 band is represented by two peaks. The remaining peaks are used to empirically fit the higher-lying optical transitions. A very good agreement of model and experimental data is observed. The imaginary part of the dielectric function derived for the measurement with p-polarized light, $\text{Im}\{\epsilon_\text{p}\}$, shows an intense peak at about 4.3 eV and a less intense peak at 3.6 eV. In contrast, $\text{Im}\{\epsilon_\text{s}\}$ shows a much broader peak at 4.1 eV and a small peak at 3.6 eV as well. This double-peak structure can be interpreted in the following way: For a perfect molecular crystal with two differently oriented molecules per unit cell one would expect a H-band and a J-band with no oscillator strength in between. The H-aggregate band would have a TDM mainly perpendicular to the surface, and would thus mainly be visible in the measurements with p-polarized light. The J-aggregate band would have a TDM mainly parallel to the surface, thus visible with s- and p-polarized light. Therefore, we can assign the peak in $\text{Im}\{\epsilon_\text{p}\}$ at 4.3 eV to the H-band and the peak at 3.6 eV in both spectra to the J-band. However, since there is some disorder also in the densely packed SAM and there is also coupling to vibrations, other states in between the H- and J-band have some oscillator strength as well. This is probably the origin of the broad peak at 4.1 eV in $\text{Im}\{\epsilon_\text{s}\}$ deduced for the measurement with s-polarized light. Also, the peak associated with the J-band overlaps with absorption of the monomer. This contribution may originate from the S_2 transition of chromophores at defect sites. In STM and AFM studies of azobenzene-alkanethiolates on Au(111) different domains of molecular lattices were found, with disordered zones between two domains of different orientation [38, 39]. Chromophores at these sites would not be part of the aggregate and may have the spectral characteristics of isolated molecules. This view is corroborated by photoisomerization kinetics experiments (Sec. 7.2.4).

Mixed Az11/C12 SAMs The same model was applied to the spectra of mixed SAMs. An exemplary spectrum and fit of a SAM with a chromophore density of 56 % is shown in Fig. 6.5a. Qualitatively, the model reproduces the S_2 band. Also, the blue-shifted peak attributed to the H-band is at a lower photon energy than in the densely packed SAM, as expected. However, when comparing data and model in the region of the S_2 band in more detail (Fig. 6.5b (top)), a deviation can be seen for the 56 % Az11 SAM: the position of the main peak is not well-reproduced and the high-energy edge of the peak has a lower slope in the model than in the data. This is not the case for the single-component Az11 SAM (bottom). Apparently, when the chromophores are diluted on the surface, the S_2 excitation cannot be described by two peaks, attributable to the H- and J-band, any more. This is a consequence of the dilution of Az11 on the surface, it increases the disorder, leading to oscillator

---

[5] The peak is visible in both Az11-containing and pure C12 SAMs.
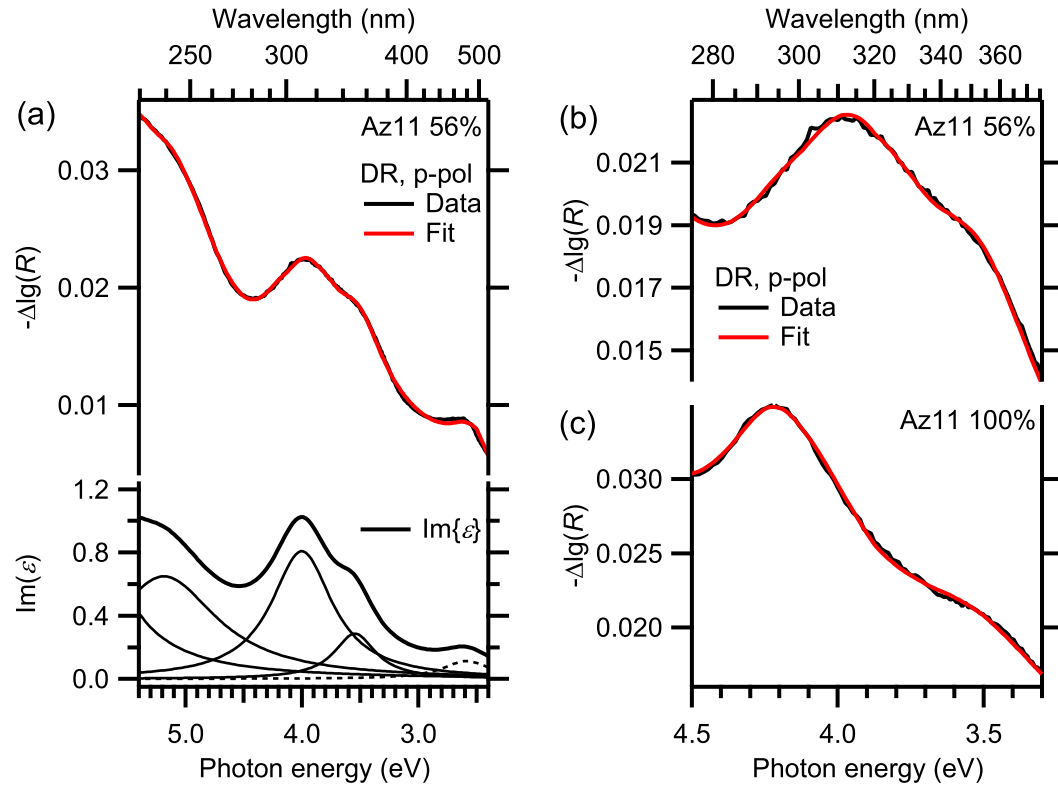
Figure 6.5: DR spectroscopy on a 56 % Az11 SAM measured with p-polarized light. (a) Spectrum and fit, and imaginary part of the resulting dielectric function. (b,c) Zoom into the region of the S_2 band of the 56 % Az11 SAM in comparison with the 100 % Az11 SAM. All peak parameters are given in Tab. B.3.

strength for states all across the band.

Optical Constants of Az11 SAM and Az11 Solution Whereas absorbance spectra directly reflect the extinction coefficient $\kappa^{\mathrm{sol}} = \mathrm{Im}\{\tilde{n}^{\mathrm{sol}}\}$ of the solution (see Sec. 3.3.1), the DR spectra are a result of an interplay of the real and imaginary part of complex refractive index $\tilde{n}$. This means, differences in spectral shape between a DR spectrum of an Az11 SAM and the absorbance spectrum Az11 in solution may in part be due to the physical quantity being measured and not only because of the formation of an exciton band in the SAM.

In order to separate these two effects we compare the extinction coefficient κ of the single-component Az11 SAM with the one of a hypothetical *trans*-Az11 solution of the same chromophore density. Note that κ is a material property, i.e., it is independent from a particular experimental method. According to Eq. 3.19, the extinction coefficient $\kappa^{\mathrm{sol}} = \mathrm{Im}\{\tilde{n}^{\mathrm{sol}}\}$ of the solution can be determined from a UV/vis absorbance measurement:

$$\kappa^{\mathrm{sol}}(\lambda) = \frac{c \ln(10)}{4\pi}\,\varepsilon(\lambda)\,\lambda, \tag{6.1}$$

with light wavelength λ, the concentration c and the decadic molar attenuation coefficient ε. ε of the Az11 solution is known[6] and the concentration of Az11

---
[6] see Sec. 9.2.3

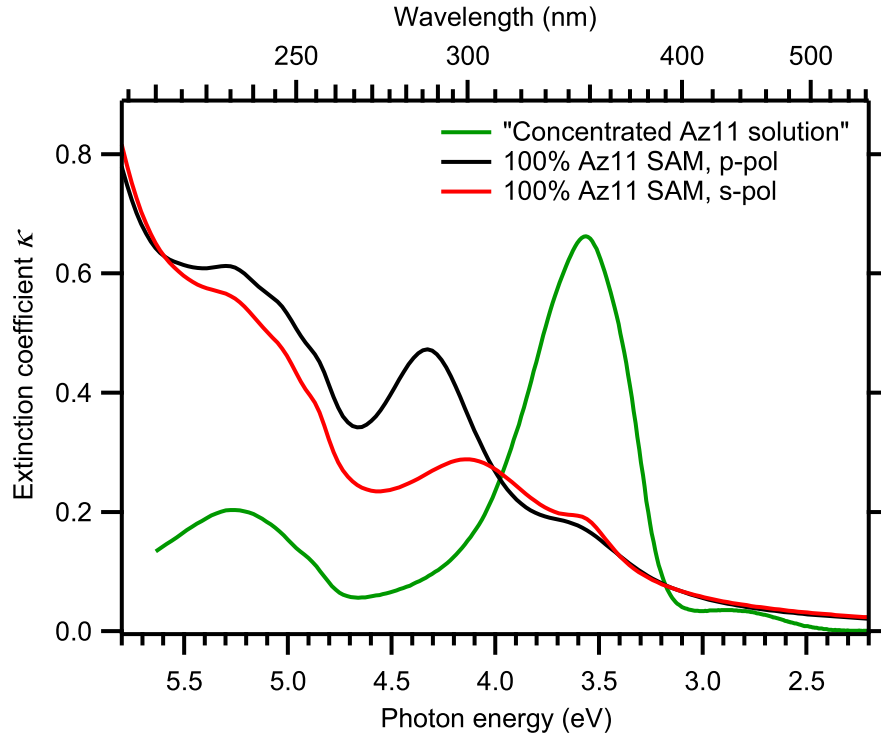**Figure 6.6:** Extinction coefficients κ of a $100\,\%$ Az11 SAM, deduced from the DR measurements with s- and p-polarized light, respectively, and of a hypothetical Az11 solution with a concentration equal to the one in the SAM.

in a molecule film can be calculated according to the footprint of Az11 in a SAM (0.242 molecules per nm^2 [39]) and the film thickness d.

The modeling of the DR spectra of the $100\,\%$ A11 SAM allowed us to determine the complex dielectric function ϵ of the SAM film for the two polarizations. We calculated the extinction coefficient $\kappa^{SAM} = Im\{\tilde{n}^{SAM}\} = Im\{\sqrt{\epsilon^{SAM}}\}$ and compared it with the extinction coefficient of the "concentrated solution".

The resulting κ spectra are shown in Fig. 6.6. The extinction coefficient κ of SAM and "concentrated solution" are on the same order of magnitude but their spectra are quite different. κ of the solution is very similar to the measured absorbance spectrum and exhibits the well-known S_1, S_2 and S_3 bands, with the S_2 band at about $3.6\,eV$ being the dominating peak. The κ spectra of the SAM, deduced for the two different polarization directions, are much more similar than the pair of measured DR spectra (see Fig. 6.1). They match above the S_3 band and below the S_1 band. The maximum of the S_2 band in the κ spectrum of the SAM is shifted by about $0.8\,eV$ with respect to the maximum in solution, whereas the peak shift in the DR spectra (Fig. 6.1) is only about $0.6\,eV$. This shift of $0.8\,eV$ in the κ spectra is directly attributable to the formation of an H-aggregate band in the SAM. A different picture is observed for the S_3 peak: In the κ spectra there appears to be no or no significant spectral shift in the band positions between SAM and solution. However, only in the case of the SAM, the S_3 transition is on top of a background that increases with increasing photon energy. This may make the S_3 transition appear at slightly higher photon energies than they actually are. We conclude that the J-aggregate of S_3 TDMs is weak at most. The

spectral shift of the S_3 band maximum in the DR spectra with respect to the S_3 band in solution (Fig. 6.1) may therefore mainly be a consequence of the experimental method.

The polarization contrast in the spectral region of the S_2 and S_3 bands reflects the orientation of TDMs involved, as discussed above: The S_2 band is split up into a blue-shifted H-band and a slightly red-shifted J-band, with the H-band being mainly visible with p-polarized light and the J-band being visible in both polarizations. The S_3 band exhibits slightly higher absorption for p- than for s-polarized light.

In summary, the deduced κ spectra confirm that the drastic difference in spectral shape of the S_2 transition in DR spectra of SAMs and absorbance spectra of Az11 in solution are due to excitonic coupling and not solely a consequence of the different experimental methods (DR spectroscopy vs. absorbance spectroscopy). This also has implications for the photoisomerization in SAMs, in particular when examining the photoisomerization in dependence on the excitation wavelength (see next chapter).

6.3   Conclusions

In this chapter we have seen that the S_2 band in Az11-containing SAMs is split into an H-band and a J-band. A strong polarization contrast is observed: the H-band corresponds to mostly upright and the J-band to mostly flat-lying TDMs. The blue-shift of the H-band decreases continuously with decreasing Az11 coverage. This is an effect of both decreasing intermolecular distance and changing orientation of chromophores. The continuous shift corroborates that Az11 and C12 mix nearly statistically on the surface. The J-band of the S_2 transition is overlapping with the spectral profile of molecules at defects, e.g., regions of disorder in between different domains of molecular arrangements. The model of two Lorentz oscillators for H- and J-band does not fit well to diluted Az11 SAMs, this is expected since with decreasing order there should be increasing oscillator strength in between the H- and J-band.

In order to disentangle the effect of different experimental methods for SAM and solution from the effect of the excitonic coupling in SAMs, the extinction coefficient κ, which is a material property, was calculated for a $100\,\%$ Az11 SAM and a hypothetical Az11 solution of same chromophore density. The S_2 transition, which is crucial for the *trans–cis* photoisomerization, is very different in the κ spectra of SAM and solution: In the SAM a splitting of the S_2 transition into H- and J-band and a significant polarization contrast is confirmed. The maximum of the H-band in the SAM is shifted by $0.8\,\mathrm{eV}$ with respect to the one in solution. Because of these differences in absorption properties we also expect drastic differences in the photoisomerization of Az11 SAMs and Az11 solutions.

Chapter 7

Isomerization Behavior

The most appealing property of azobenzene is its ability to isomerize upon optical excitation. We will now examine in how far the interaction between azobenzene chromophores has an impact on the isomerization behavior of Az11 SAMs: The chromophores are ordered in a 2D crystal and optical spectroscopy revealed that the chromophores are excitonically coupled. In particular the S_2 transition is very broad, with its peak shifted to higher photon energies. We therefore expect significant differences in the isomerization behavior of Az11 SAMs and Az11 solutions.

7.1 Az11 in Solution

Initially we examine the photoisomerization and the thermal isomerization of Az11 in methanolic solution. This is done by absorbance spectroscopy under ambient conditions. Experimental details are given in Sec. 9.3.

7.1.1 Photoisomerization

As described in Sec. 2.1.1, the absorbance spectrum of *trans*-Az11 is characterized by the very weak S_1 absorption band at ca. 440 nm, the pronounced S_2 band at 347 nm, and the strong S_3 band at 250 nm. Fig. 7.1a shows an absorbance spectrum of *trans*-Az11 and a series of spectra after repeated illumination with light of $\lambda_{\mathrm{exc}} = 365$ nm, which is at the high-wavelength edge of the S_2 band of the *trans* isomer. We observe *trans–cis* photoisomerization: With increasing illumination time the intensity of the S_2 band decreases and the band shifts towards shorter wavelengths (blue-shift). Additionally we observe a signal increase of the S_1 band. The change of the S_3 peak is minor, we observe a small increase and blue-shift. The *trans–cis* photoisomerization upon illumination with light of 365 nm is almost complete ($\approx 98\,\%$, see Tab. 7.1 and Sec. A.1.1) because the absorbance of the *cis* isomer at this wavelength is very minor compared with the very strong absorbance of the *trans* isomer.

Starting from the 365 nm-PSS we then examined the photoisomerization with blue light of $\lambda_{\mathrm{exc}} = 455$ nm, at the S_1 band of *trans*- and *cis*-Az11 (see Fig. 7.1b). Light of this wavelength mainly triggers the *cis–trans* isomerization: As the illumination with blue light proceeds, the intensity of the S_2 peak increases again whereas the intensity of the S_1 decreases. In the PSS we obtain about 74 % *trans* molecules.
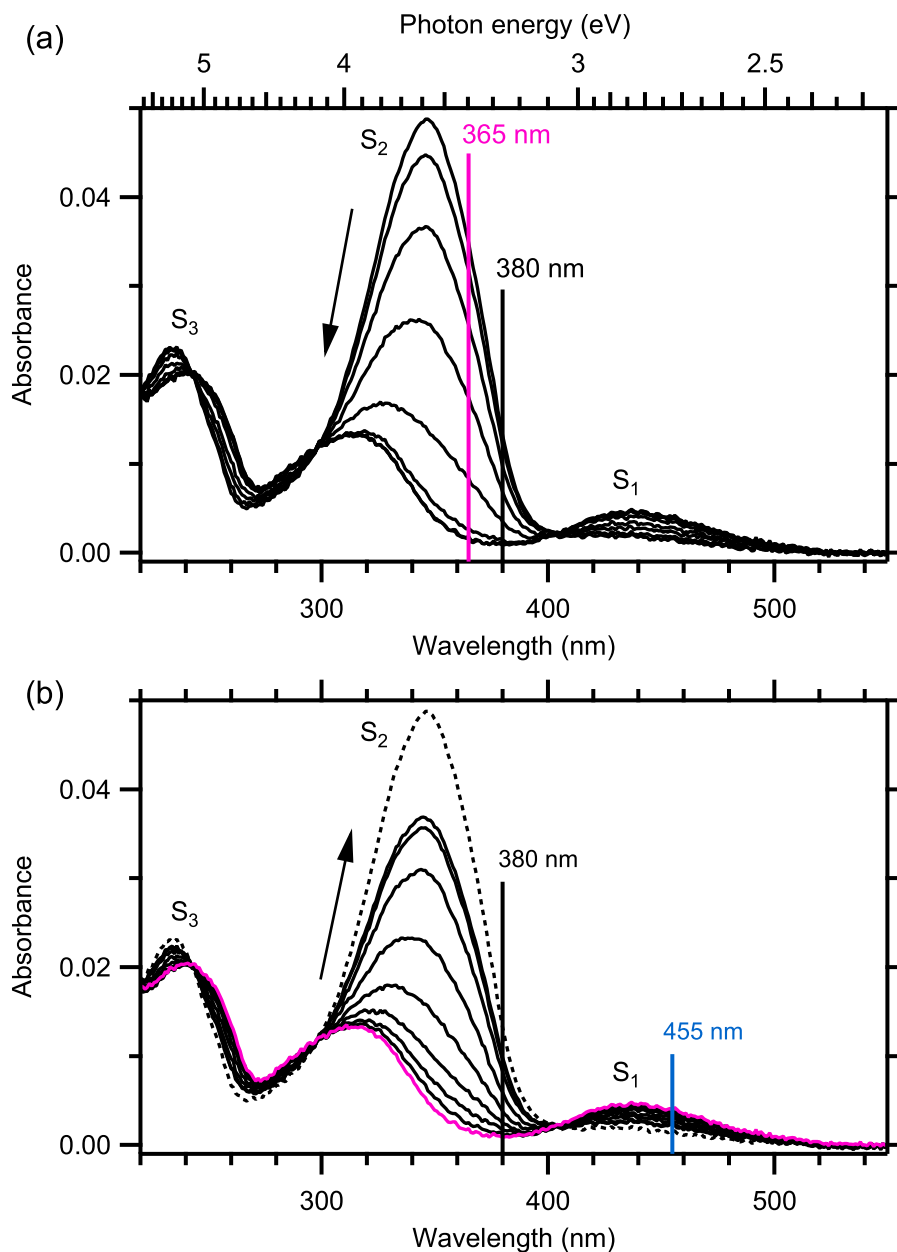
Figure 7.1: Photoisomerization of Az11 in solution. (a) Illumination with UV light of 365 nm (cf. pink line): pristine (pure *trans*) spectrum and spectra after 1, 3, 7, 15, 31, 63, and 127 seconds of illumination. The last two spectra are indistinguishable, meaning that the PSS is reached. The black line at 380 nm marks the wavelength at which the isomerization kinetics were recorded, see Fig. 7.3. (b) Illumination with light of 455 nm (cf. blue line): spectrum of the 365 nm-PSS (pink) and spectra after 2, 4, 8, 16, 32, 64, 128 seconds of illumination, and the pristine spectrum (dashed).
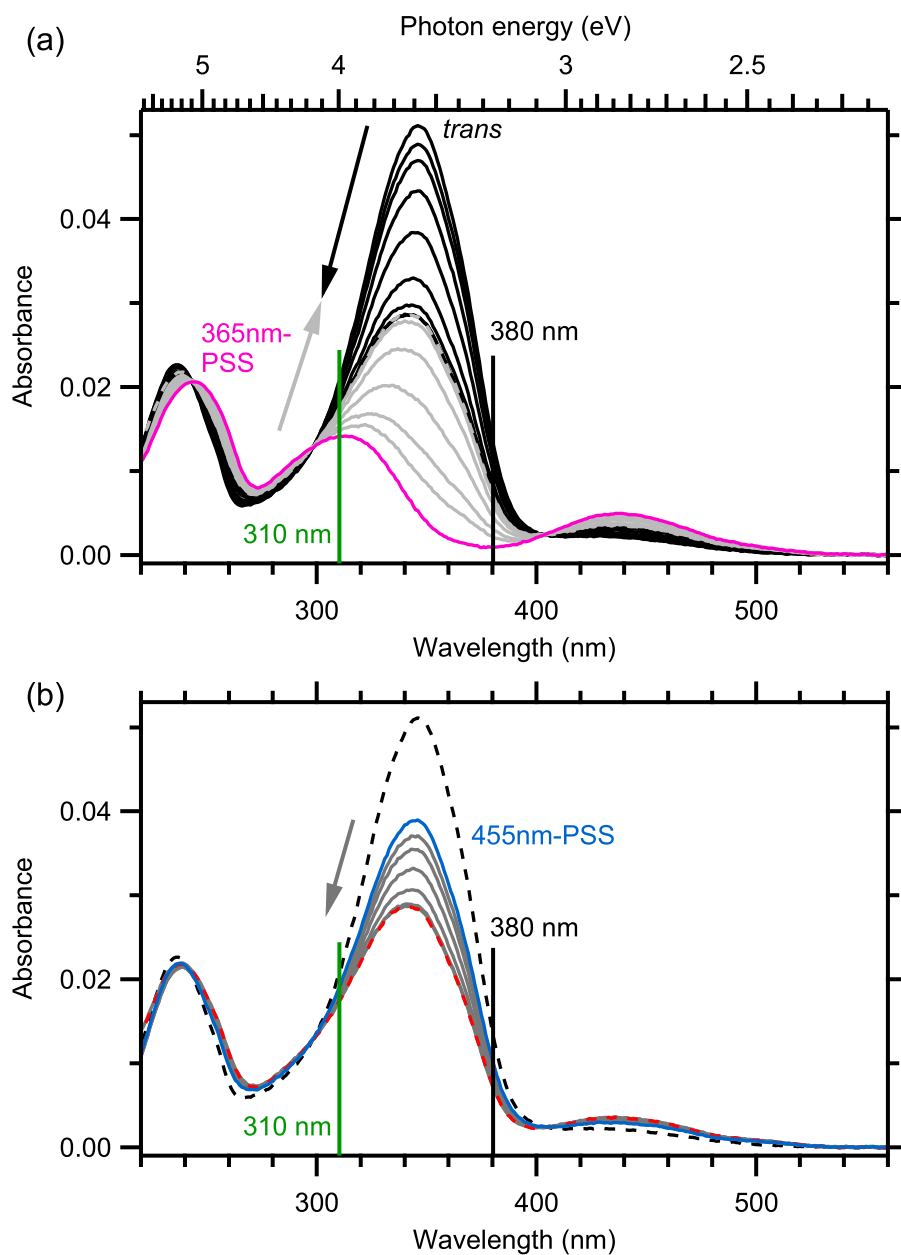
Figure 7.2: Photoisomerization under illumination with 310 nm (cf. green line) starting from different initial states. The black lines at 380 nm mark the wavelength at which the isomerization kinetics (see Fig. 7.3) were examined. (*a*): Spectra of the pristine sample (thick black line) and after 10, 20, 40, 80, 160, 320, 640, and 1280 seconds of illumination (black). Spectrum of the 365 nm-PSS (pink) and spectra after 20, 40, 80, 160, 320, 640, and 1280 seconds of illumination (light gray). The same PSS is reached in both experiments. (*b*): Spectrum of the 455 nm-PSS (blue) and a series of spectra after 20, 40, 80, 160, 320, 640, and 1280 seconds of illumination (dark gray). The PSS obtained is the same as in the previous experiments (red, dashed). The spectrum of the pristine sample (black, dashed) is shown for comparison.

Table 7.1: Photoisomerization and thermal isomerization of Az11 in solution: excitation wavelengths λ_{exc},[a] light intensities I_{ph}, isomerization time constants τ obtained in kinetics measurements (cf. Figs. 7.3 and 7.4), and the respective fraction $\chi_{\mathrm{c,PSS}}$ of *cis* isomers in the PSSs. The errors in the time constants are taken from fit results and do not contain systematic errors (see text). Note: The photoisomerization time constants are on the order of seconds, whereas the thermal isomerization time constant is on the order of days.

λ_{exc}	I_{ph} (mW cm^{-2})	Initial cond.[b]	τ	$\chi_{\mathrm{c,PSS}}$ (%)
365 nm	2.10 $\pm$ 0.12	pure *trans*	9.47 $\pm$ 0.26 s	98 $\pm$ 2
455 nm	3.26 $\pm$ 0.12	365 nm-PSS	19.11 $\pm$ 0.34 s	26 $\pm$ 1
310 nm, #1	0.175 $\pm$ 0.012	pure *trans*	101.0 $\pm$ 2.5 s	48 $\pm$ 1
310 nm, #2	0.175 $\pm$ 0.012	365 nm-PSS	93.9 $\pm$ 1.6 s	48 $\pm$ 1
310 nm, #3	0.175 $\pm$ 0.012	455 nm-PSS	101.1 $\pm$ 2.3 s	49 $\pm$ 1
Thermal isomerization		365 nm-PSS	70 $\pm$ 2 h	

[a] Spectral characteristics of the light sources are given in Tab. 9.3.
[b] Initial condition

Finally we also examined the photoisomerization triggered by deep-UV light with a central wavelength of 310 nm. This wavelength is at the low-wavelength edge of the S_2 band of the *trans* molecule and near the maximum of the S_2 band of the *cis* molecule. Three experiments were performed: The isomerization was monitored starting with the pure *trans* state, the 365 nm-PSS, and the 455 nm-PSS (cf. Fig. 7.2). As expected for first-order kinetics, the PSS does not depend on the initial condition (Eq. 2.13): The same fraction $\chi_{\mathrm{c,PSS}} \approx 50\,\%$ of *cis* isomers in the PSS is found in all three experiments (cf. Tab. 7.1). The 310 nm-PSS lies in between the PSSs obtained at 365 and 455 nm.

In the following we examined the kinetics of the photoisomerization: Fig. 7.3 shows the temporal evolution of the absorbance at 380 nm during illumination with light of 365, 455 and 310 nm.[1] The data is well-described by single-exponential functions, as expected for first-order kinetics (cf. Sec. 2.1.2). The time constants obtained from the fits and the intensities of the light sources are given in Tab. 7.1. In the case of photoisomerization triggered by 310 nm we find that the time constant obtained when starting from a mixture with a high amount of *cis* isomers (365 nm-PSS) is about 10 % lower than the time constant obtained when starting from a mixture with lower amount of *cis* molecules (pure *trans* or 455 nm-PSS). This is probably an experimental artifact, for example by slight inhomogeneity of the light beam on the cell.

The photoisomerization kinetics allows us to determine photoisomerization cross-sections and quantum-yields. This is done in Sec. 7.1.3.

7.1.2 Thermal Isomerization

Starting with a sample in the PSS for illumination with 365 nm, we also examined the thermal isomerization of Az11 in solution by keeping the sample

---

[1] 380 nm is also the wavelength where the fraction of *cis* isomers in the PSSs was determined: at this wavelength the absorption of the *cis* isomer is almost zero (see Sec. A.1.1).
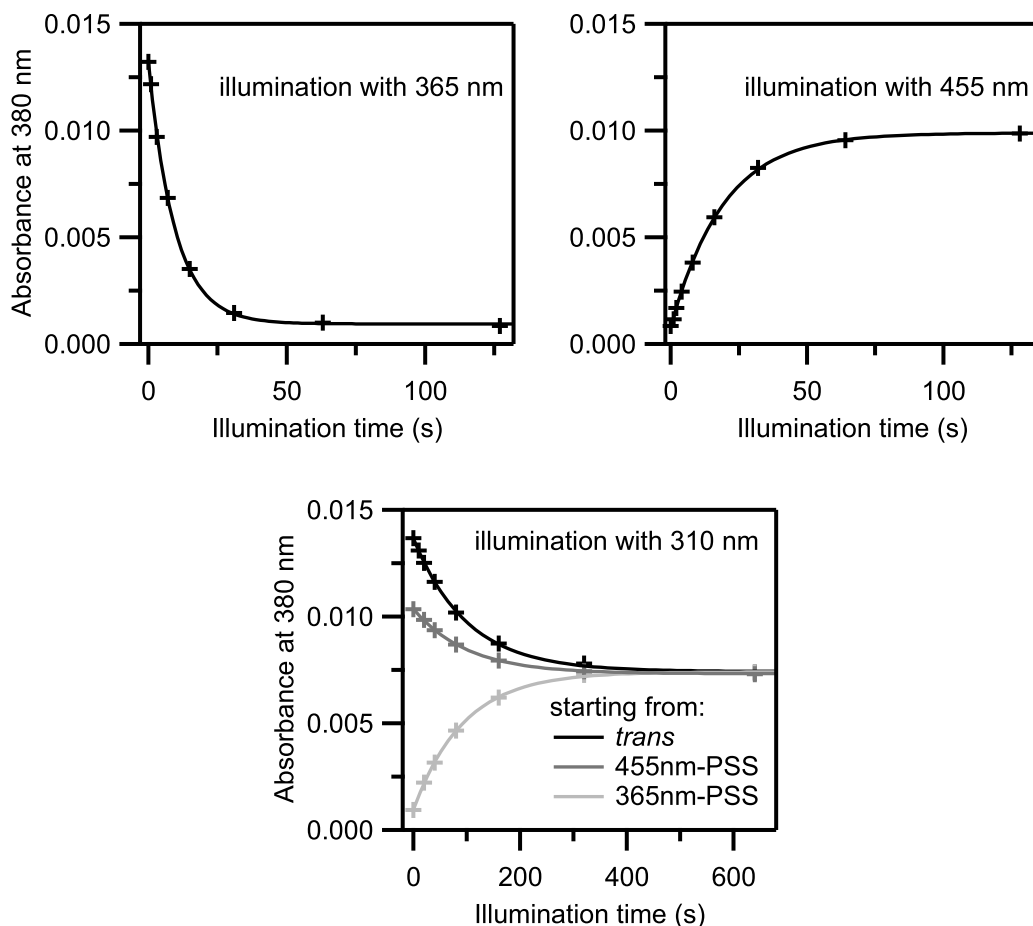
Figure 7.3: Photoisomerization kinetics with light of 365, 455 and 310 nm recorded at 380 nm and fitted with single-exponential functions. The resulting time constants are given in Tab. 7.1.

in the dark and repeatedly recording spectra in certain intervals, see Fig. 7.4. The light intensity of the spectrophotometer is so low that its influence on the isomerization state can be neglected. We evaluated the kinetics of the process analogously to the photoisomerization and fitted the data with a single-exponential function (see inset of Fig. 7.4). We found a time constant τ_{th} of about 70 hours (see Tab. 7.1). In contrast, the time constants of photo-isomerization are on the order of seconds to minutes for the light intensities employed in our experiments. We can therefore neglect thermal isomerization over photoisomerization.

Generally, the thermal isomerization time constant of azobenzenes varies by orders of magnitude depending on the polarity of the solvent and different substituents to the azobenzene skeleton. Experimental [31, 32] and theoretical [89] studies discuss these effects. For 4-methoxy-azobenzene, a compound similar to Az11, time constants of between 30 and 49 hours were found at room temperature [31, 32]. This is in line with our findings.

Figure 7.4: Thermal isomerization: Spectrum of the $365\,\text{nm}$-PSS (pink), selected spectra after increasing periods of time (black), and the spectrum of the pristine solution (dashed). The vertical line at $380\,\text{nm}$ marks the wavelength at wh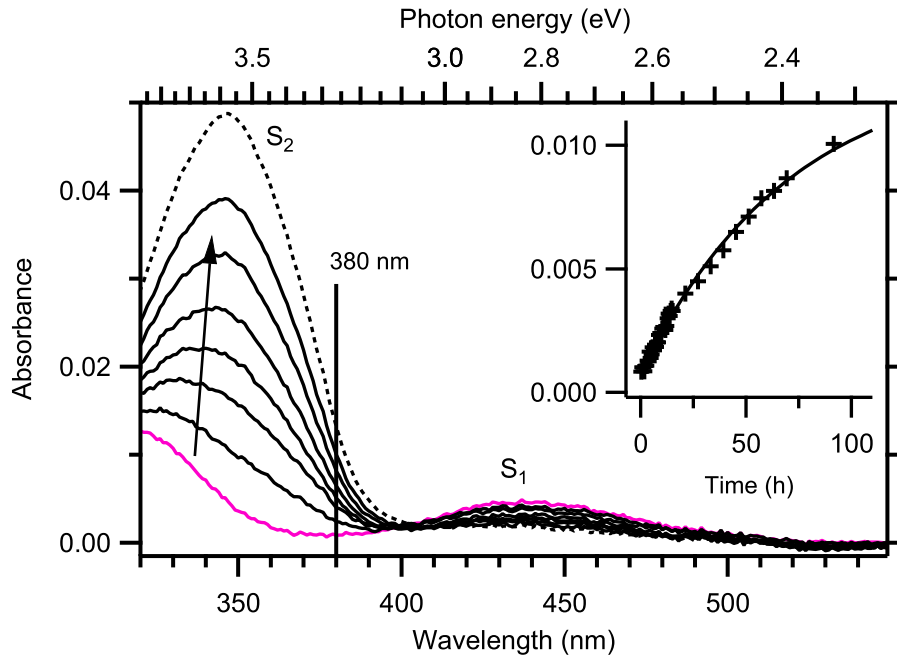ich the isomerization kinetics were evaluated. Inset: Kinetic curve from all spectra (markers) and a single-exponential fit to the data (solid line). We find a thermal isomerization time constant on the order of days (cf. Tab. 7.1). The offset of the exponential function was fixed to the absorbance value of the pristine solution, i.e., for $t \to \infty$ all molecules should isomerize back to *trans*.

7.1.3 Photoisomerization Cross-Sections and Quantum-Yields

The results of the kinetics measurements (Fig. 7.3 and Tab. 7.1) allow us to determine photoisomerization cross-sections and quantum-yields of Az11 in solution. We thereby deduce properties of a single molecule from the measurement of a macroscopic sample: The photoisomerization cross-section σ^{ph} is a measure for the probability of a chromophore to isomerize due to an *incoming* photon and the photoisomerization quantum-yield Φ is the probability of isomerization upon *absorption* of a photon. The equations (2.20), (2.18) and (2.19) were used to calculate the effective isomerization cross-sections $\tilde{\sigma}$, the *trans–cis* isomerization cross-sections $\sigma_{\text{t}}^{\text{ph}}$, and the *cis–trans* isomerization cross-sections $\sigma_{\text{c}}^{\text{ph}}$:

$$\tilde{\sigma} = \frac{\tilde{k}}{J} \tag{7.1}$$

$$\sigma_{\text{t}}^{\text{ph}} = \frac{\tilde{k}\,\chi_{\text{c,PSS}}}{J} \tag{7.2}$$

$$\sigma_{\text{c}}^{\text{ph}} = \frac{\tilde{k}\,(1 - \chi_{\text{c,PSS}}) - k_{\text{c}}^{\text{th}}}{J}. \tag{7.3}$$

The photon flux $J = I_{\text{ph}}/E_{\text{ph}}$ is the ratio of light intensity I_{ph} and photon energy E_{ph}. The effective rate constant $\tilde{k}$ is the inverse of the photoisomerization time constants τ given in Tab. 7.1. The resulting photoisomerization

Table 7.2: Isomerization cross-sections and quantum yields of azobenzenes in solution. The isomerization cross-sections were calculated according to the values in Tab. 7.1. In the case of the illumination with 310 nm the average of the three measurements was used.

λ_{exc}	Cross sections $(10^{-17}\,\mathrm{cm}^2)$			Quantum yields	
	$\tilde{\sigma}$	σ_t^{ph}	σ_c^{ph}	Φ_t	Φ_c
Az11[a]					
365 nm	2.7 ± 0.2	2.7 ± 0.2	$\lesssim 0.2$	0.36 ± 0.03	—
455 nm	0.70 ± 0.03	0.18 ± 0.02	0.52 ± 0.03	0.52 ± 0.06	0.59 ± 0.03
310 nm	3.7 ± 0.3	1.8 ± 0.2	1.9 ± 0.2	0.43 ± 0.04	0.68 ± 0.07
4-EtO-AB[b]					
366 nm				0,35	—
436 nm				0,31	0,56
313 nm				0,52	0,51

[a] In methanol
[b] 4-Ethoxy-azobenzene in ethanol [90]

cross-sections for Az11 in solution are given in Tab. 7.2. Values on the order of $10^{-17}\,\mathrm{cm}^2$ were found. The cross sections can be interpreted according to the following equations, which directly follow from the fact that the photoisomerization proceeds on a much faster timescale than the thermal isomerization: $\tilde{\sigma} = \sigma_t^{ph} + \sigma_c^{ph}$ and $\chi_{c,PSS} = \sigma_t^{ph}/(\sigma_t^{ph} + \sigma_c^{ph})$ (see Eqs. 2.21 and 2.23).

We find that the effective isomerization cross-section $\tilde{\sigma}$ for illumination with 455 nm is considerably smaller than the respective values for illumination with 365 and 310 nm. This is a direct consequence of the relatively low absorbance of both isomers at 455 nm.

In addition we calculated *trans–cis* and *cis–trans* isomerization quantum yields Φ_t and Φ_c (Eqs. 2.24):

$$\Phi_t = \frac{\sigma_t^{ph}}{\sigma_t^{abs}}; \quad \Phi_c = \frac{\sigma_c^{ph}}{\sigma_c^{abs}}, \tag{7.4}$$

with σ_t^{abs} and σ_c^{abs} being the absorption cross-sections of both isomers. They were calculated from the absorbance spectra, see A.1.2. The resulting quantum yields Φ are given in Tab. 7.2. In our findings Φ_c is bigger than Φ_t. Also, Φ_t of illumination with 455 nm is bigger than the ones of illumination with the UV wavelengths. Both is in good agreement with measurements of (unsubstituted) azobenzene in methanol or ethanol [90–93], although the absolute values differ due to different excitation wavelengths and the large difference in the S_2 band position λ_{max} of azobenzene and Az11.[2] The observation that Φ_c is generally bigger than Φ_t is attributed to steeper potential landscapes on the side of the *cis* isomer [27, 95]. That the quantum yield for $\pi\pi^\star$ excitation is smaller than the quantum yield for $n\pi^\star$ excitation,[3] is explained by different isomerization

---

[2] λ_{max} of 320 nm and 347 nm for azobenzene [94] and Az11, respectively
[3] This constitutes a violation of the Kasha rule, which states that fluorescence (which is orders of magnitude faster than nuclear motions) occurs from the lowest excited state [9, 96].

pathways, with increased probability of relaxation back to the initial structure in the case of $\pi\pi^\star$ excitation [9, 27].

The absolute numbers of the photoisomerization quantum yields Φ_t and Φ_c determined for Az11 are compared with the ones of 4-ethoxy-azobenzene (EtO-AB) in ethanol [90] (cf. Tab. 7.2). This molecule has the same chromophore as Az11 and the effect of different alkyl chain lengths is negligible.[4] The quantum yields are generally comparable: there is an excellent agreement in Φ_t(365nm/366nm) and Φ_c(455nm/436nm), whereas some deviations are observed for Φ_t(455nm/436nm) and both quantum yields at $310/313$ nm. It is unclear where the difference of Φ_t(455nm/436nm) comes from. The slightly different excitation wavelengths should be negligible because for all wavelengths it is still the same optical excitation being driven. However, the authors of [90] believe their quantum yields at 313 nm to be erroneous due to admixture of shorter-wavelength light. Also, their chromophore concentrations were very high and manual stirring at frequent intervals was therefore required, while the experimental details concerning the interval time and the photon fluxes of the external light appear to contradict each other.[5]

By comparing the absorbance spectra of *trans*- and *cis*-Az11 and considering their isomerization quantum-yields we can interpret the fraction of *cis* isomers in the PSSs (Tab. 7.1): At 365 nm the absorbance of the *cis* isomer is at least 20 times less than the absorbance of the *trans* isomer. Since in general the photoisomerization quantum-yield of non-interacting photoswitches is ≤ 1, Φ_c is at most three times bigger than $\Phi_t \approx 0.36$. This is not enough to make up for the low absorbance of the *cis* isomer and therefore it is plausible that the 365 nm-PSS contains about $98\,\%$ *cis* isomers (details of the calculation in Sec. A.1.1). At 310 nm the absorbance of the *trans* isomer is about 1.4 times the absorbance of the *cis* isomer but since the *cis–trans* isomerization has the higher quantum yield, about half of the molecules are in the *cis* configuration in the 310 nm-PSS. At 455 nm the *cis* isomer absorbs more than the *trans* isomer and Φ_c is slightly bigger than Φ_t, therefore the PSS contains mostly *trans* isomers.

Finally, it is also possible to extrapolate the fraction of *cis* isomers $\chi_{c,\mathrm{PSS}}(\lambda)$ for any λ in the spectral range of the S_2 band: According to (2.23), $\chi_{c,\mathrm{PSS}}(\lambda)$ in the limit of negligible thermal isomerization (which is the case in Az11 solutions at room temperature) can be written as:

$$\chi_{c,\mathrm{PSS}}(\lambda) = \frac{\sigma_t^{\mathrm{ph}}(\lambda)}{\sigma_t^{\mathrm{ph}}(\lambda) + \sigma_c^{\mathrm{ph}}(\lambda)} = \left(\frac{\sigma_c^{\mathrm{ph}}(\lambda)}{\sigma_t^{\mathrm{ph}}(\lambda)} + 1 \right)^{-1}. \tag{7.5}$$

Expressing the photoisomerization cross-sections σ^{ph} as product of absorption cross-sections σ^{abs} and isomerization quantum yields Φ (see Eqs. 7.4) and using that the absorption cross-section of the respective isomer is proportional to its

---

[4] $\lambda_{\max}$ of the S_2 band lies at 348 nm and 347 nm for EtO-AB in ethanol [94] and Az11 in methanol, respectively.

[5] The typical interval time was 30 s and the photon doses given correspond to light intensities between 1.5 and $6\,\mathrm{mW\,cm^{-2}}$. In our experiments we found time constants on the order of tens to hundred seconds, with light intensities on the same order of magnitude or one order of magnitude lower than theirs. So their interval times should have been too long to follow the kinetics.
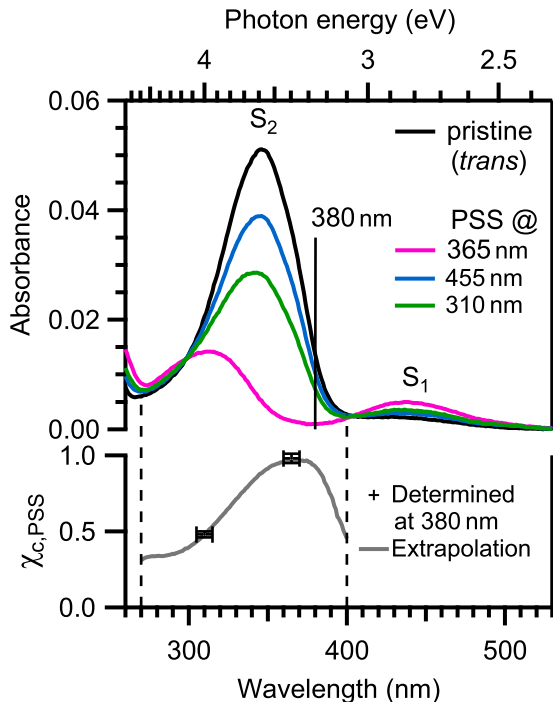
Figure 7.5: Top: Absorbance spectra of Az11 in the pristine (pure *trans*) state and the photostationary states (PSSs) for excitation with light of 365, 455 and 310 nm. Bottom: Fraction $\chi_{c,PSS}$ of *cis* molecules in the PSSs at 310 and 365 nm (crosses) determined from the absorbance at 380 nm. The solid gray curve is an extrapolation of $\chi_{c,PSS}$ for excitation wavelengths across the whole S_2 band (details see text).

absorbance spectrum $A(\lambda)$ (Sec. 3.3), gives

$$\chi_{c,PSS}(\lambda) = \left(\frac{A_c(\lambda)}{A_t(\lambda)} \frac{\Phi_c(\lambda)}{\Phi_t(\lambda)} + 1 \right)^{-1}. \tag{7.6}$$

The ratio Φ_c/Φ_t can be assumed to be constant across the S_2 band [97]. Thus, with the ratio of quantum yields[6] determined at 310 nm, $\chi_{c,PSS}(\lambda)$ can be extrapolated. The resulting curve is shown in Fig. 7.5. Starting at about 300 nm, $\chi_{c,PSS}(\lambda)$ steadily increases, reaches a maximum at about 365 nm and then goes down again, reflecting the absorption profiles of the *trans* and *cis* isomer. This curve will later serve as a basis for comparison of the fraction of *cis* isomers in SAM and solution (see Sec. 7.2.5).

7.1.4   Conclusions

In this section we analyzed the thermal isomerization and photoisomerization of Az11 in solution. We found a thermal isomerization rate-constant on the order of days, which is negligible over photoisomerization for the photon doses employed in this work. Illumination with UV light of 365 nm results in a PSS with almost exclusively *cis* isomers, whereas by illumination with UV light of 310 nm only about 50 % *cis* isomers are observed. Illumination with 455 nm leads to a PSS with about 75 % *trans* isomers. We determined photoisomerization cross-sections on the order of $10^{-17}\,\mathrm{cm^2}$. The resulting photoisomerization quantum-yields are in overall agreement with literature [90]. The dependence of the quantum yield on the isomer and the excitation energy agree with isomerization mechanisms postulated by theoretical calculations [27, 95, 98].

---

[6]   The determination of the ratio Φ_c/Φ_t of quantum yields at 310 nm is described in Sec. A.1.3.

7.2 Az11 SAMs

We now come to the central question on how the isomerization behavior of Az11 is influenced by intermolecular interactions, the SAM structure, the chromophore density and the environment. By NEXAFS we examined the orientation of chromophores in Az11 SAMs (Chap. 5) and by DR spectroscopy (Chap. 6) we examined their optical properties. The isomerization of Az11 in solution, where the intermolecular interactions can be neglected, was examined in the previous section.

In this section we begin by quantifying the photoisomerization and thermal isomerization in Az11 SAMs. This is done by NEXAFS, since NEXAFS is quantitative in the amount of *trans* and *cis* isomers. For this we chose a SAM with Az11 coverage Θ of 20 %. We determine the amount of *cis* isomers in the PSSs and the photoisomerization cross-sections and compare the results with Az11 in solution. We also compare measurements in NEXAFS (vacuum) and DRS (ambient conditions) to examine the effect of the environment. Using DRS we then investigate the photoisomerization of SAMs with different Az11 coverages. We find that already a minor dilution of the Az11 chromophores on the surface allows a pronounced photoisomerization. By examining the isomerization kinetics we find indications of a cooperative photoisomerization process.

7.2.1 Isomerization in Vacuum

7.2.1.1 Spectra

In Fig. 7.6a N 1s NEXAFS spectra of a pristine 20 % Az11 SAM (i.e., all molecules are in *trans* configuration) for different X-ray polarizations are shown. Upon illumination with UV light we expect to observe *trans–cis* photoisomerization. However, an illumination with UV light of 365 nm shows only a minor change in polarization contrast at the LUMO excitation, see Fig. 7.6b. In other parts of the spectrum no changes are observed.

We therefore performed high-resolution NEXAFS on the LUMO excitation to look for possible signatures of photoisomerization. These measurements were performed with the X-ray polarization in magic angle, so that the X-ray absorption is independent of changes in the molecular orientation (see Sec. 3.2.7). In Fig. 7.7a spectra of the pure *trans* state and the PSSs for illumination with light of 365 and 455 nm are shown. It can be seen that for the 365 nm-PSS the position of the LUMO excitation is shifted to a higher photon energy, while its intensity is slightly decreased. After illumination with blue light of 455 nm the original spectrum is preserved. This is a clear indication of photoisomerization.

Since NEXAFS is quantitative in the magic angle geometry, the signal is a linear combination of the spectra of *trans*- and *cis*-Az11, respectively. On this basis the NEXAFS spectrum in the 365 nm-PSS can be decomposed into spectra of the pure isomers (cf. Fig. 7.7b). The spectrum A_{PSS} of a PSS can be written as

$$A_{\text{PSS}} = (1 - \chi_{\text{c,PSS}})A_{\text{t}} + \chi_{\text{c,PSS}}A_{\text{c}}, \tag{7.7}$$

with A_{t} and A_{c} being the spectra of a pure *trans* and *cis* sample, respectively,
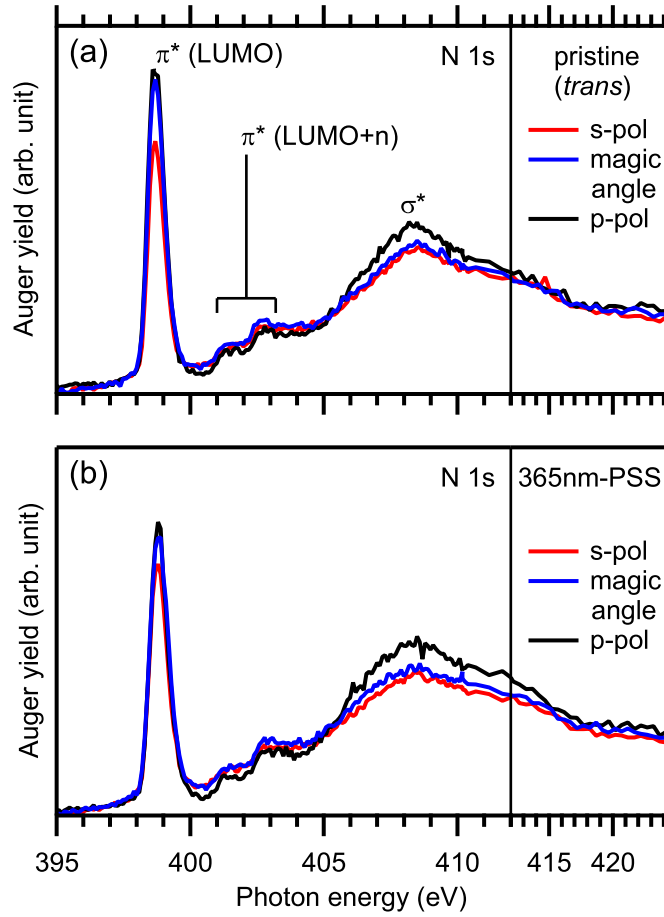
Figure 7.6: N 1s NEXAFS spectra of a 20 % Az11 SAM recorded for different X-ray polarizations. (a) Pristine (pure *trans*) SAM. (b) Spectra after illumination with UV light of 365 nm. No changes could be observed except for a minor change in polarization contrast of the LUMO excitation. Higher-resolution NEXAFS spectra of the LUMO excitation are shown in Fig. 7.7.

and $\chi_{c,PSS} = (1 - \chi_{t,PSS})$ being the fraction of *cis* isomers in the PSS. By rearranging (7.7) we obtain:

$$A_c = \frac{A_{PSS} - (1 - \chi_{c,PSS})A_t}{\chi_{c,PSS}} \tag{7.8}$$

We find $\chi_{c,PSS}(365\text{nm}) \geq 50\%$. Otherwise the reconstructed spectrum of the *cis* SAM would become negative at certain energies, which is unphysical.

An *upper* limit of 74 % for the amount of *cis* isomers in the 365 nm-PSS was determined from the isomerization kinetics (see next section). The resulting reconstructed spectrum of the *cis* SAM with its range of uncertainty according to the upper and lower limits is shown in Fig. 7.7c. We find that the LUMO excitation of the *cis* isomer is broadened and shifted to higher photon energies by about 0.20 ± 0.02 eV with respect to the *trans* isomer. An analogous shift was observed in XPS [99, Supporting Information]: Here the spectrum of the 365 nm-PSS is shifted to higher binding energy with respect to the spectrum of the *trans* state by about 0.14 eV. The shift of the reconstructed *cis* spectrum should be bigger, therefore the shift in XPS is compatible with the energetic difference observed in NEXAFS [100].
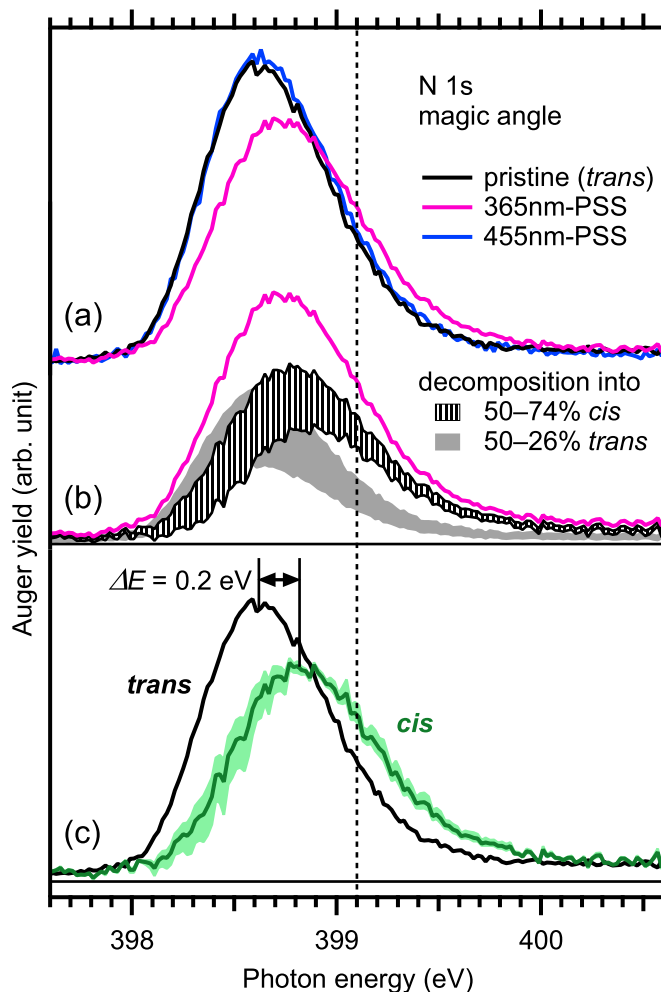
Figure 7.7: High-resolution N 1s NEXAFS spectra of the LUMO excitation shown
in Fig. 7.6, recorded at a sample temperature of ca. 110 K. (a) The pristine state (i.e.,
pure *trans*) and the photostationary states (PSSs) under exposure of light with 365
and 455 nm, respectively. The dashed line at 399.1 eV denotes the photon energy at
which the isomerization kinetics were monitored. (b) Spectrum of the 365 nm-PSS
decomposed into its *trans* and *cis* components. (c) Constructed spectrum of the
pure *cis* isomer. The range of uncertainty corresponds to the upper and lower limit
of the amount of *cis* molecules given in (b). The spectrum of the *trans* isomer is
shown for comparison.

7.2.1.2   Kinetics

The energetic difference between the LUMO excitation of the *trans* and the *cis*
isomer is exploited to examine the isomerization kinetics of Az11 SAMs in an
UHV environment. At a photon energy of 399.1 eV (cf. dashed line in Fig. 7.7)
the *cis* isomer has a higher absorption than the *trans* isomer. Fig. 7.8 shows
an exemplary[7] transient of the X-ray absorption at this photon energy during
photoisomerization experiments with light of 365 and 455 nm, and without
illumination in order to examine the thermal isomerization.

   In each segment the X-ray absorption evolves nearly exponentially towards
a new stationary state. Additionally, we observed a general decrease of the
signal over time with a time constant on the order of hours, which is two

---

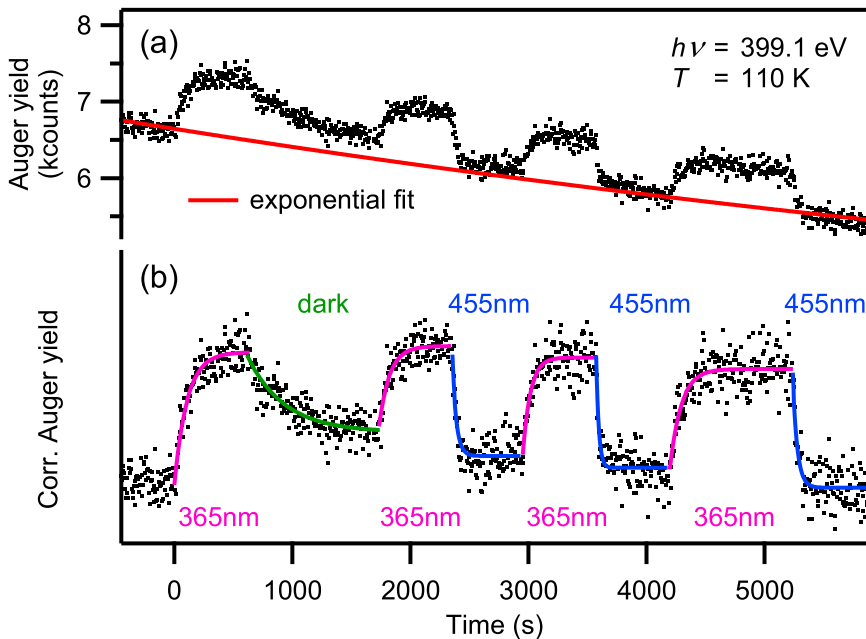[7] Additional data is shown in Sec. B.1.3.

Figure 7.8: Transient NEXAFS measurements on a SAM at ca. 110 K in s-polarization. (a) Data as measured. The general decrease in the signal by ca. 15 % over 1 h is caused by X-ray beam damage and was described by an exponential fit (red line); details are given in Sec A.2. (b) Corrected data. Each segment of the kinetics was fitted with a single-exponential function (pink, green, and blue lines).

Table 7.3: Time constants τ of photoisomerization (and the corresponding light intensities I_{ph}) and thermal isomerization in SAMs with 20 % Az11 coverage. The spectral characteristics of the light sources are given in Tab. 9.3.

λ_{exc}	I_{ph} (mW cm^{-2})	T (K)	τ (s)
365 nm	4.03 ± 0.16	110 ± 5	90 ± 14
455 nm	15.32 ± 0.16	110 ± 5	27.7 ± 8.6
455 nm	8.23 ± 0.16	110 ± 5	37.9 ± 6.3
Thermal isomerization		110 ± 5	340 ± 84
Thermal isomerization		293 ± 5	170 ± 10

orders of magnitude slower than the time constants observed in isomerization reactions. This signal decrease is attributed to X-ray beam damage of the SAM[8] and was corrected by subtracting a suitable background (details on the beam damage and its correction are given in Sec. A.2). The result is shown in Fig. 7.8b. We fitted every segment with single-exponential functions with an

---

[8] This is concluded because the signal decrease is independent from illumination with UV or visible light and SAMs of chemisorbed molecules should otherwise be stable in vacuum. Also, we found the signal decrease to be faster in measurements at room temperature than at 110 K, in agreement with the observation that X-ray beam damage is strongly increased at higher temperatures (see Sec. 3.1.4). To further reduce beam damage, the X-ray exposure time was only a fraction of each time interval (details see Sec. 3.2.3). Varying the x-ray exposure time per interval would have allowed to observe the effect of beam damage directly.
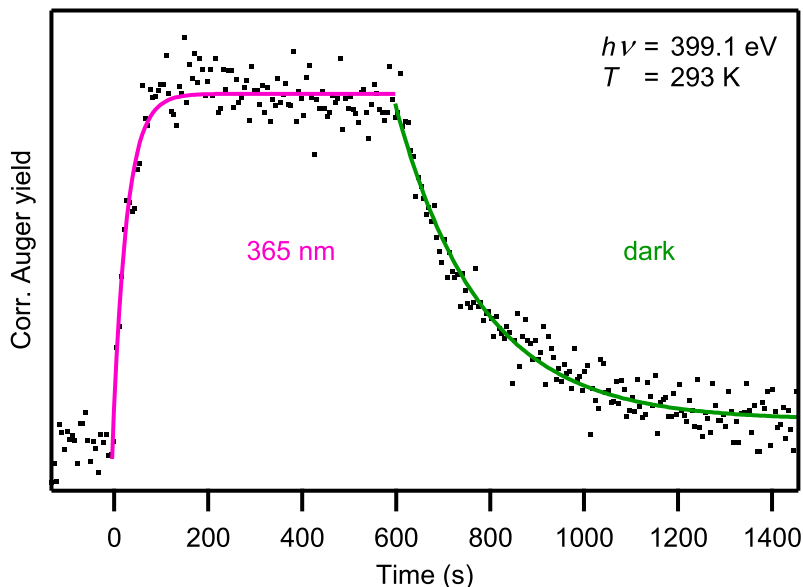
Figure 7.9: Transient NEXAFS measurement on a SAM at room temperature, corrected for X-ray beam damage: Photoisomerization triggered by light of 365 nm and subsequent thermal isomerization in the dark.

effective rate constant (2.7):

$$\tilde{k} = k_c^{ph} + k_c^{th} + k_t^{ph}, \tag{7.9}$$

with k_t^{ph} being the *trans–cis* photoisomerization rate-constant, k_c^{ph} being the analogous *cis–trans* photoisomerization rate-constant, and k_c^{th} being the thermal *cis–trans* isomerization rate-constant.

Fitting the "dark" ($k_c^{ph} = k_t^{ph} = 0$) segment[9] therefore directly yields the thermal isomerization rate-constant k_c^{th}. We determined k_c^{th} at ca. 110 K as well as at room temperature (cf. Fig. 7.9). The resulting time constants $\tau_c^{th} = 1/k_c^{th}$ are given in Tab. 7.3. The thermal relaxation at room temperature is faster than at 110 K, as one would expect. Applying the Arrhenius equation [101, Chap. 1] yields a potential barrier of 10 meV and an attempt frequency of $10^{-2}\,\text{s}^{-1}$ for the thermal *cis–trans* isomerization in the SAM. Both values seem implausibly small: From experimental [32] and theoretical [89] works, energy barriers on the order of 1 eV and $10^{11\pm1}\,\text{s}^{-1}$ have been reported for azobenzene derivatives in vacuo or in solution. This large discrepancy indicates that the thermal isomerization of Az11 in the SAM cannot be described by a simple Arrhenius model.

From the segments measured during illumination with 365 or 455 nm light we determined the photoisomerization time-constants $\tau^{ph} = \tilde{k}^{-1}$ (also given in Tab. 7.3) by single-exponential fits. We find that, for the photon doses employed in our experiment, the thermal isomerization time-constant is of the same order of magnitude as the time constants observed in photoisomerization. Therefore, the fraction $\chi_{c,PSS}$ of *cis* molecules in the 365 nm-PSS is in this case

---

[9] In Fig. 7.8b the asymptote observed in the "dark" segment is different than the asymptotes in the following "blue" segments. This might indicate deviations from first order kinetics.

Table 7.4: Isomerization cross-sections of Az11 SAMs in comparison with Az11 in solution (cf. Sec. 7.1.3). Calculated according to the values in Tab. 7.3.

Sample	λ_{exc}	Cross sections ($10^{-17}\,\text{cm}^2$)		
		$\tilde{\sigma}$	$\sigma_{\text{t}}^{\text{ph}}$	$\sigma_{\text{c}}^{\text{ph}}$
SAM (20 % Az11)	365 nm	0.14 ± 0.02	0.09 ± 0.02	$\lessgtr 0.04$
	455 nm	0.12 ± 0.03	0.005 ± 0.001	0.10 ± 0.03
Az11 (sol.)	365 nm	2.7 ± 0.2	2.7 ± 0.2	$\lessgtr 0.2$
	455 nm	0.70 ± 0.03	0.18 ± 0.02	0.52 ± 0.03

limited by the thermal isomerization:

$$\chi_{\text{c,PSS}} \overset{(2.13)}{=} \frac{k_{\text{t}}^{\text{ph}}}{\tilde{k}} \overset{(7.9)}{=} \frac{\tilde{k} - k_{\text{c}}^{\text{ph}} - k_{\text{c}}^{\text{th}}}{\tilde{k}} \tag{7.10}$$

The *cis–trans* photoisomerization rate-constant k_{c}^{ph} is unknown, but for $k_{\text{c}}^{\text{ph}} \to 0$ we obtain an upper limit of 74 % *cis* isomers in the 365 nm-PSS at 110 K.[10] For non-zero values k_{c}^{ph} $\chi_{\text{c,PSS}}$ would be smaller. A lower limit of 50 % was already determined in Sec. 7.2.1.1. For $\chi_{\text{t,PSS}}(455\text{nm})$ we assumed a value of 95 %, since in Fig. 7.7a the spectrum of the 455 nm-PSS is very similar to the one of the pure *trans* spectrum.

On the basis of the deduced sample compositions we are now able to determine also the photoisomerization cross-sections $\sigma_{\text{t}}^{\text{ph}}$ and $\sigma_{\text{c}}^{\text{ph}}$ according to (2.18) and (2.19), see Tab. 7.4. $\sigma_{\text{t}}^{\text{ph}}$ is bigger than $\sigma_{\text{c}}^{\text{ph}}$ at 365 nm and vice versa at 455 nm. Note that these values reflect the efficiency of *trans–cis* and *cis–trans* photoisomerization and do not contain contributions from the thermal isomerization any more. We also calculated the effective photoisomerization cross-sections $\tilde{\sigma}$ according to (2.20) and found values of the order of $10^{-18}\,\text{cm}^2$ for both excitation wavelengths. These are in line with values reported for mixed azobenzene-alkanethiol/alkanethiol SAMs on gold: $2\text{–}4 \times 10^{-18}\,\text{cm}^2$ for illumination with UV light [22, 23, 102] and $2\text{–}3 \times 10^{-18}\,\text{cm}^2$ for illumination with blue light [22, 102].

Finally we can use (2.23) and the values of $\sigma_{\text{t}}^{\text{ph}}$ and $\sigma_{\text{c}}^{\text{ph}}$ to calculate the fraction of *cis* isomers to be expected if thermal isomerization was negligible:

$$\chi_{\text{c,PSS}}^{\text{no therm.}}(365\text{nm}) = \frac{\sigma_{\text{t}}^{\text{ph}}(365\text{nm})}{\sigma_{\text{t}}^{\text{ph}}(365\text{nm}) + \sigma_{\text{c}}^{\text{ph}}(365\text{nm})} \tag{7.11}$$

By evaluating this expression using the values given in Tab. 7.4, we calculated that the fraction of *cis* isomers in case of negligible thermal isomerization (e.g., for a much higher UV photon flux) would lie between 67 and 100 % instead of 50 and 74 %.

Finally, we compare the cross sections of Az11 SAMs and Az11 solutions: For the Az11 SAM the effective cross sections $\tilde{\sigma}$ of the two excitation wavelengths are approximately the same, whereas for Az11 in solution $\tilde{\sigma}(365\text{nm})$ is about a factor of 4 bigger than $\tilde{\sigma}(455\text{nm})$. Similarly, in literature on mixed

---

[10] This assumption is meaningful also because for the Az11 molecule in solution $\sigma_{\text{c}}^{\text{ph}}(365\text{nm})$ is much smaller than $\sigma_{\text{t}}^{\text{ph}}(365\text{nm})$, see Tab. 7.4.

azobenzene-alkanethiol/alkanethiol SAMs, the effective cross sections of illumination with UV and blue light are approximately the same [22], or the cross section of illumination with UV light is even smaller than the one of illumination with blue light [102]. Also in Ref. [103] it is described that for illumination with UV light the rate of photoisomerization is much smaller in SAM than in solution (same UV light intensity), whereas for illumination with blue light the rates of photoisomerization in SAM and in solution are approximately the same (again same light intensity). We conclude that aligning azobenzene-containing molecular switches on a metal surface has a more drastic effect on the *trans–cis* photoisomerization than on the *cis–trans* photoisomerization. This could be due to steric hindrance or excitonic coupling: The *trans*-SAM is well-ordered and *cis* isomers take up more space laterally than *trans* isomers, therefore *trans–cis* isomerization may be less probable already because of steric reasons. In contrast, the *cis–trans* isomerization is less affected by steric hindrance. Also the excitonic coupling affects the *trans–cis* and the *cis–trans* photoisomerization differently: As shown above, $\tilde{\sigma}(365\text{nm})$ is dominated by *trans–cis* photoisomerization and $\tilde{\sigma}(455\text{nm})$ is dominated by *cis–trans* photoisomerization. In solutions of *trans*-Az11 the excitation wavelength of 365 nm matches the high-wavelength edge of the S_2 peak, but in the *trans*-SAM the S_2 peak is strongly altered, with its maximum shifted to shorter wavelengths (see Chap. 6). This means that the absorbance at 365 nm is significantly reduced compared to the free molecule. Therefore, a significant reduction of the *trans–cis* photoisomerization cross-section is expected.[11] The excitation wavelength of 455 nm matches the S_1 band of *cis*-Az11 in solution. The S_1 band of *cis*-Az11 is not clearly visible in the SAM but since the S_1 TDM of free *cis*-Az11 is much smaller than the S_2 TDM of free *trans*-Az11, a much smaller excitonic shift is expected for the S_1 band in SAMs as well. Therefore, also the absorption profile of *cis*-Az11 in SAMs and solution should be similar. This would also explain that the difference in effective isomerization cross-section of Az11 solutions and Az11-SAMs is bigger for 365 nm than for 455 nm.

7.2.2 Influence of the Environment

In the previous section we have seen that the thermal isomerization of Az11 in SAMs on gold proceeds on the order of minutes when the sample is kept in vacuum. In the following we want to examine the thermal isomerization under ambient conditions. For this we used DR spectroscopy: Fig. 7.10a shows DR spectra of a SAM with 20 % Az11 coverage. In the spectrum of the pristine (pure *trans*) SAM the maximum of the S_2 band is found at 320 nm (ca. 3.9 eV). Upon illumination with UV light of 365 nm we observe a significant signal decrease of the S_2 peak, analogous to Az11 in solution (cf. Sec. 7.1.1). Therefore, the signal change in the DR spectrum is indicative of *trans–cis* photoisomerization (the photoinduced changes in DR spectra of Az11 SAMs are examined in detail in Sec. 7.2.3).

Starting from the DR spectrum of the SAM in the 365 nm-PSS, we then monitored the transient DR signal at 320 nm in order to observe the thermal *cis–trans* isomerization. The resulting curve is shown in Fig. 7.10b. The data

---

[11] Photoisomerization experiments with different excitation energies to match different parts of the S_2 band are presented in Sec. 7.2.5.

Table 7.5: Time constants τ^{th} of thermal isomerization at room temperature in different environments.

Sample	Environment	Method	τ^{th} (seconds)	(hours)	Notes
SAM (20% Az11)	Vacuum	NEXAFS	170 ± 10		Tab. 7.3
SAM (20% Az11)	Vacuum	DR		< 1.5	Fig. 7.10a
SAM (80% Az11)	Nitrogen atm.	SHG[a]	70 ± 20		Ref. [99]
	Ambient air	SHG		> 10	Ref. [99]
SAM (80% Az11)	Ambient air	DR		23 ± 2	Tab. B.4
SAM (20% Az11)	Ambient air	DR		26 ± 3	Fig. 7.10b
Az11	Methanolic sol.	UV/vis		70 ± 2	Tab. 7.1

[a] Second harmonic generation

is well-described with a single-exponential function with a time constant on the order of a day. This is significantly slower than in case of the NEXAFS measurements in vacuum (cf. Tab. 7.5). In order to exclude the possibility that the different experimental methods are the cause for this difference, we illuminated the SAM with UV light of 365 nm again, exposed it to a high vacuum on the order of 10^{-6} mbar for 90 min and recorded a DR spectrum again (Fig 7.10a). It can be seen that the exposure to vacuum leads to an almost complete recovery to the pure *trans* SAM. A subsequent illumination with UV light results in a PSS which is identical to the previous one, which shows that the SAM had not been degraded or altered. We conclude that ambient air leads to a pronounced slowing down of the thermal isomerization.

The thermal isomerization in different environments was also examined by second harmonic generation (SHG) [99]: There, a isomerization time-constant on the order of several hours was observed in ambient air, which is in agreement with the DR measurements. In contrast, in a nitrogen atmosphere a much faster thermal isomerization on the order of seconds was found (cf. Tab. 7.5).

Unlike ambient air, both vacuum and nitrogen atmosphere are water-free environments. Since water is a polar molecule and *cis*-Az11 is polar as well [102], we assume that under ambient conditions water molecules are adsorbed on the SAM at sites of *cis* isomers. The *trans* isomer is much less polar than the *cis* isomer [102], therefore the adventitious water makes the *cis* isomer energetically more favorable and slows down the thermal *cis*–*trans* isomerization. In contrast, in water-free environments such as vacuum or nitrogen atmosphere, such an effect does not exist and the thermal isomerization is faster.

The nanoscale condensation of water even on hydrophobic films was shown by [104]. The interpretation of adventitious water being responsible for the stabilization of the *cis* state is also supported by literature: For a SAM almost identical to ours,[12] a thermal isomerization time-constant on the order of minutes was observed in vacuum as well [105]. In contrast, for another mixed

---

[12] A mixed SAM of Az12 and C12. Az12 is identical to Az11 but has a dodecamethylene linker chain.
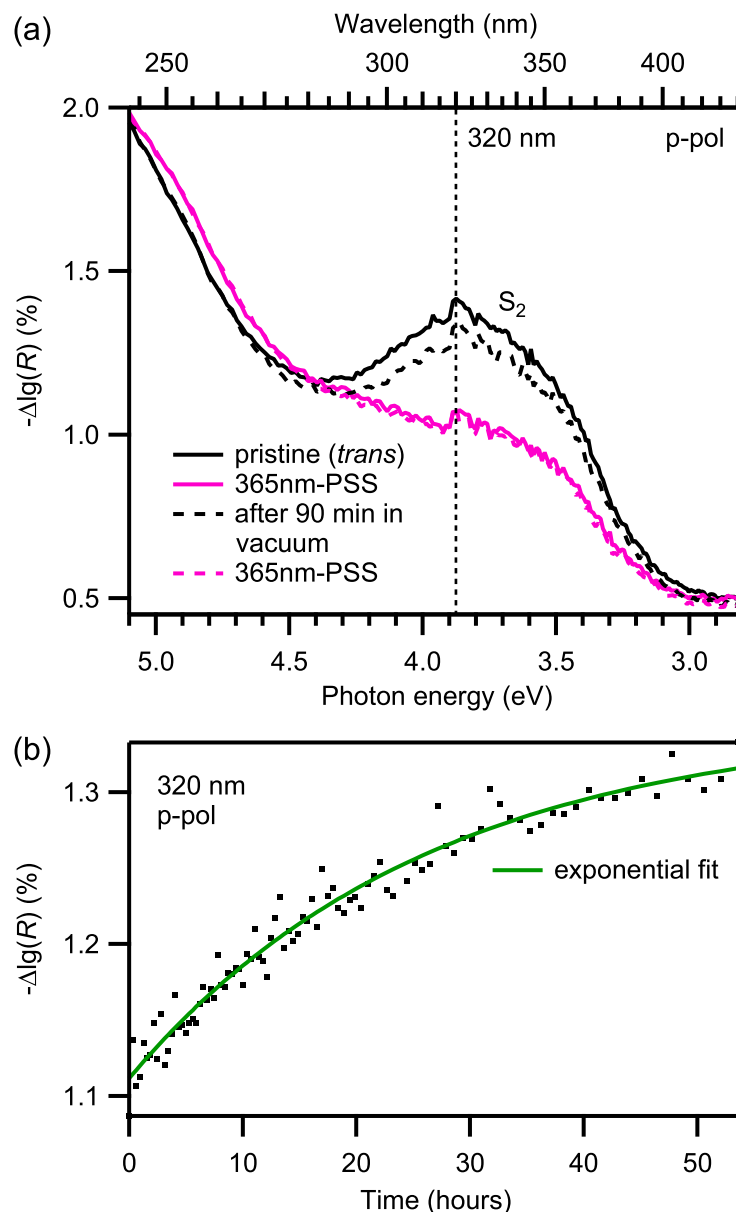
Figure 7.10: Differential reflectance (DR) measurements of a SAM recorded *under ambient conditions*, with p-polarized light and at an angle of incidence of 45°. (a) Spectra of the S_2 band, details see text. (b) Transient of the DR showing the thermal relaxation in air, recorded at 320 nm (vertical dashed line in (a)). We obtain a time constant of about one day (see Tab. 7.5).

SAM consisting of a p-CN-substituted azobenzene and C12 as a spacer, no stabilization of the *cis* state was observed under ambient conditions [23]. In this case the *cis* state might not be stabilized by adventitious water because in contrast to the H-Azo compound, the CN-Azo compound has a smaller dipole moment in the *cis* state than in the *trans* state [105]. We conclude that considering the environment is crucial for examining the isomerization kinetics in SAMs.
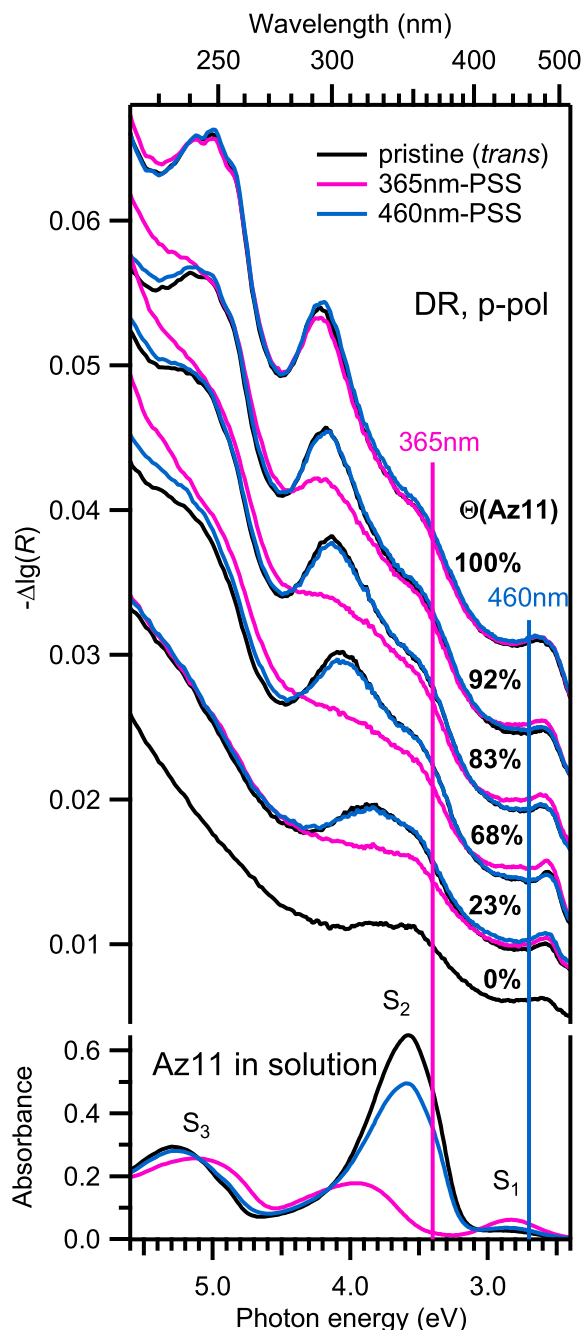
Figure 7.11: Photoisomerization experiments on Az11 SAMs and Az11 in solution. The pristine state and photostationary states (PSSs) for illumination with UV light (365 nm) and blue light (460 nm) are shown. Top: DR spectra of SAMs taken with p-polarized light for different Az11 coverages Θ; vertical offsets were added for clarification. Bottom: Absorbance spectra of Az11 in methanol. The illumination wavelengths are indicated by vertical lines.

7.2.3 Varying the Chromophore Density

By NEXAFS spectroscopy it was demonstrated exemplarily for a 20 % Az11 SAM, that the azobenzene compound can be photoisomerized also in SAMs. In order to investigate how the isomerization behavior depends on the Az11 coverage we used again DR spectroscopy. We expect a dependence of the photoisomerization on Θ since the optical properties of the *trans* SAM already change drastically (see Chap. 6).

In Fig. 7.11 DR spectra of photoisomerization experiments on SAMs with various Az11 coverages are shown, in comparison with the photoisomerization of Az11 in solution. For the 100 % Az11 SAM only very small spectral changes can be seen upon illumination with UV light of 365 nm. This was observed also for other densely-packed azobenzene-alkanethiol SAMs and it was concluded

that the isomerization is hindered by steric hindrance or excitonic coupling (see Sec. 2.2). However, even for a minor dilution to about 92 % Az11, a significant and reversible change in DR is observed. This Az11 coverage Θ corresponds to a situation where in average less than 1 in 8 neighbors in the rectangular lattice [39] is replaced by a spacer molecule. Upon illumination with UV light (365 nm), the DR signal between 3.5 and 4.5 eV goes down and a signal increase is observed at about 2.7 eV, indicating a significant *trans–cis* isomerization. This is analogous to the spectral changes observed for Az11 in solution, where the isomerization to the *cis* conformation leads to a signal decrease in the S_2 band and a signal increase in the S_1 band (see Sec. 7.1.1). Illumination with blue light (460 nm) then predominantly triggers the *cis–trans* isomerization: The DR signal of the S_2 band increases again and the DR signal of the S_1 band decreases. The DR spectrum of the 455 nm-PSS is very close to that of the pure *trans* state. This indicates that the 455 nm-PSS contains mostly *trans* isomers, in agreement with the results from the NEXAFS measurements on SAMs (Sec. 7.2.1).

Analogous spectral changes after illumination with UV and blue light can be seen in spectra of SAMs with lower Az11 coverages. In the cases of SAMs with 83 and 68 % Az11 (in average 1–2 and 2-3 in 8 neighbors are replaced by C12 spacers, respectively), the signal change upon illumination with UV light is bigger than in the 92 % SAM, which indicates that a higher fraction of *cis* isomers is observed. The signal change in the 20 % SAM (in average 6 in 8 lattice sites are occupied by C12) is lower because the area of the peak attributable to the S_2 transition is smaller as well. Quantifying the amount of *cis* isomers from DRS alone is very difficult. However, from the NEXAFS measurements on a 20 % Az11 SAM (Sec. 7.2.1) we could conclude that in the 365 nm-PSS at least 67 % of the chromophores should be in the *cis* state under ambient conditions. A comparison of the effective isomerization cross sections of a 80 % Az11 SAM and a 20 % Az11 SAM can be found in Sec. B.2.2.

Note that in all mixed SAMs the excitation wavelength of 365 nm (3.4 eV) is far from the maximum of the S_2 band in *trans*-Az11 SAMs, but yet the signal change is strongest in this spectral range (between 3.9 and 4.2 eV).[13] The implications of this result are discussed in more detail in the next section.

7.2.4   Probing Different Parts of the S_2 Band

In the previous section it was described that upon photoisomerization with UV light (365 nm, 3.4 eV) the biggest signal change is observed in the maximum of the H-band of the S_2 transition and not in the spectral range where the UV light is absorbed. In the following we examine the kinetics of the photoisomerization, i.e., the temporal evolution of the DR signal during exposure of the sample with UV or blue light. In particular we are interested in the question if not just the amplitude of the signal change but also the kinetics of the photoisomerization are different across the broad S_2 band. For this we chose a SAM with an Az11 coverage Θ of 80 % (spectra shown in Fig. 7.12), i.e., with considerable excitonic shift of the H-band (cf. Fig. 6.3). We recorded the kinetics of photoisomerization triggered by light of 365 and 455 nm at two photon

---

[13] The full width at half maximum of the emission spectrum of the UV light source is only about 0.1 eV (cf. Tab. 9.3), which is too small to explain this.
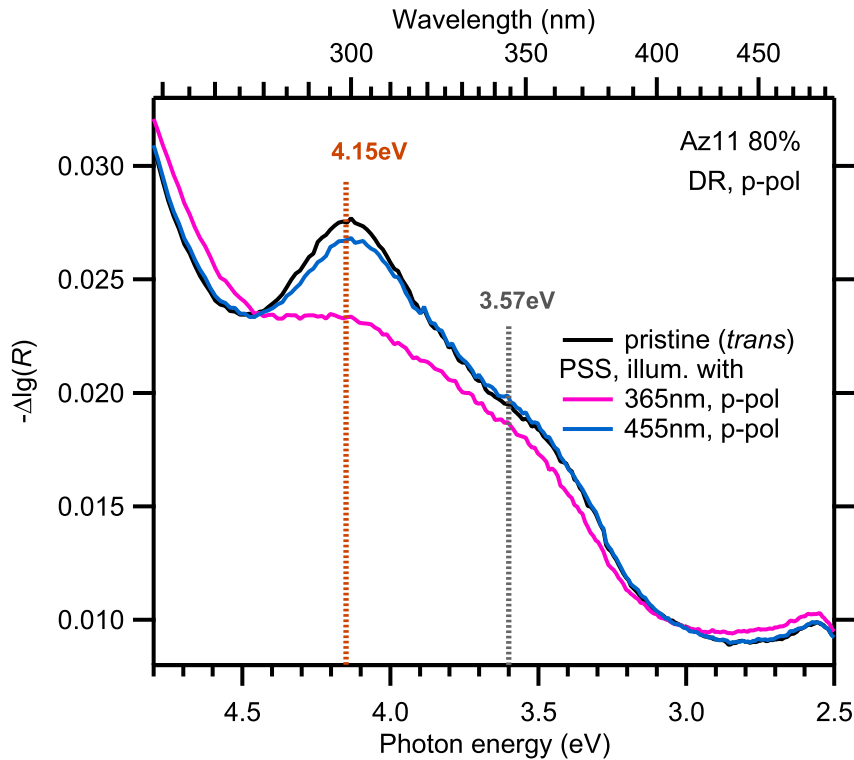
Figure 7.12: DR spectra of a $\Theta = 80\%$ SAM measured with p-polarized light, in the pristine state and the PSSs for illumination with light of 365 and 455 nm. The vertical lines denote the photon energies at which the isomerization kinetics were recorded (see Fig. 7.13).

energies of probing: 3.57 eV (347 nm), the low-energy shoulder of the S_2 band, and at 4.15 eV (299 nm), the maximum of the H-band of the S_2 transition.[14] (Details on how the measurements were performed are given in Sec. 9.5.1.) The kinetic curves are shown in Fig. 7.13. They are reasonably well described by a single-exponential function.[15] Starting with the pure *trans* state, upon illumination with light of 365 nm, a signal decrease is observed at both photon energies of probing, in agreement with the full spectra of the pristine SAM and the SAM in the 365 nm-PSS (Fig. 7.12). We find that the DR signal decreases significantly faster at 4.15 eV than at 3.57 eV (by a factor of about 1.6). Then, when proceeding with blue light illumination (455 nm), which predominantly triggers *cis–trans* isomerization, the opposite behavior is observed: The DR signal at 3.57 eV increases significantly faster than at 4.15 eV (by a factor of about 3.57). The same can also be observed when monitoring the thermal *cis–trans* isomerization (by a factor of about 4.6). The time constants τ^{ph} and τ^{th} of photoisomerization and thermal isomerization obtained from the fits are given in Tab. 7.6.

This behavior may be interpreted considering well-ordered *trans* isomers, disordered *trans* isomers and *cis* isomers: Upon illumination with UV light, disordered *trans* isomers, for example at domain walls, are able to isomerize to

---

[14] The spectral resolution was 2 nm, which corresponds to 0.02 eV at 3.57 eV and 0.03 eV at 4.15 eV.

[15] For long enough measurement times deviations from first order kinetics are observed, see Fig. B.8 in the Appendix.
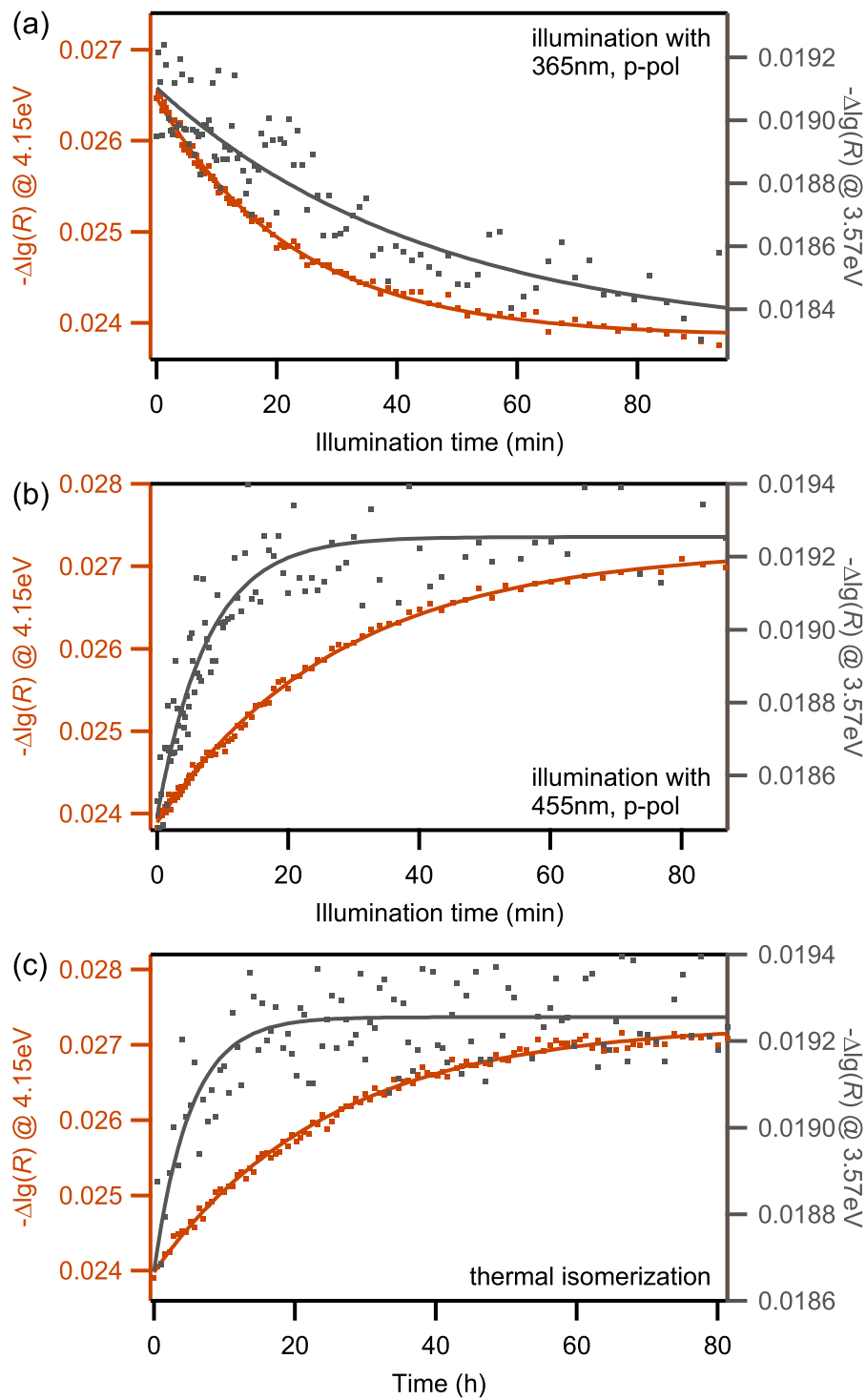
Figure 7.13: Isomerization kinetics of a SAM with $\Theta(\text{Az11}) = 80\%$ probed with p-polarized light of 299 nm (4.15 eV, maximum of the S_2 band, *left axis*) and 347 nm (3.57 eV, low-energy shoulder of the S_2 band, *right axis*). The corresponding spectra are shown in Fig. 7.12. (a) Illumination with 365 nm, p-pol, starting from the 455 nm-PSS. (b) Illumination with 455 nm, p-pol, starting from the 365 nm-PSS. (c) Thermal isomerization, starting from the 365 nm-PSS again.

Table 7.6: Time constants τ^{ph} (minutes) and τ^{th} (hours) of photoisomerization and thermal isomerization, respectively, in a SAM with $\Theta(\mathrm{Az11}) = 80\,\%$, for excitation wavelengths λ_{exc} (p-pol) and probing wavelengths λ_{pr} (p-pol). The spectral characteristics of the light sources are given in Tab. 9.3.

λ_{exc}, pol.	I_{ph} (mW cm^{-2})	Initial condition	Dom- inating process	$\lambda_{\mathrm{pr}} =$	τ^{ph} (min) 299 nm (4.15 eV)	347 nm (3.57 eV)
365 nm, p	0.32 ± 0.02	455 nm-PSS	t→c		23 ± 1	38 ± 7
455 nm, p	0.328 ± 0.009	365 nm-PSS	c→t		27 ± 2	8 ± 1
310 nm, p	0.036 ± 0.003	455 nm-PSS	t→c		45 ± 3	— [a]
310 nm, p	0.036 ± 0.003	365 nm-PSS	c→t		62 ± 3	25 ± 5
					τ^{th} (h)	
Thermal isomerization		365 nm-PSS	c→t		23 ± 2	5 ± 1

[a] No signal change observed

cis. This means that the order among neighboring *trans* is reduced as well, i.e., well-ordered *trans* isomers are converted into disordered *trans* isomers. The disordered *trans* isomers can then be converted to *cis*. This results in a faster signal decrease at the high-energy end of the S_2 transition (corresponding to ordered *trans* isomers) than at the low-energy end (corresponding to disordered *trans* isomers). The opposite behavior is observed for *cis–trans* isomerization: First, *cis* isomers are converted to disordered *trans* isomers. Establishing order in the SAM takes more time. Therefore the signal increase at the maximum of the H-band is slower than at the low-energy edge of the S_2 band. As the state of the surrounding molecules affects the switching probability this can be considered as a cooperative effect.

7.2.5 Varying the Excitation Energy

After examining the kinetics of photoisomerization at different parts of the DR spectrum which represent the absorption behavior of different species of molecules (*trans* isomers in well-ordered arrangements vs *trans* isomers in more disordered arrangements) we now examine how the photoisomerization depends on which species of molecules is optically excited. The DR spectrum is dominated by the H-band of the S_2 transition, attributable to well-ordered *trans* isomers, whereas the DR signal in the low-energy region of the S_2 transition is smaller (J-aggregate and disordered *trans* isomers). By optically exciting the SAM with photon energies in that spectral range, significant *trans–cis* photoisomerization was observed.

In the following we examine in how far the excitation with photon energies in the spectral range of the H-band leads to a different photoisomerization characteristics. To answer this question we again chose a SAM with an Az11 coverage Θ of $80\,\%$ and compared the PSSs we obtained by photoisomerization
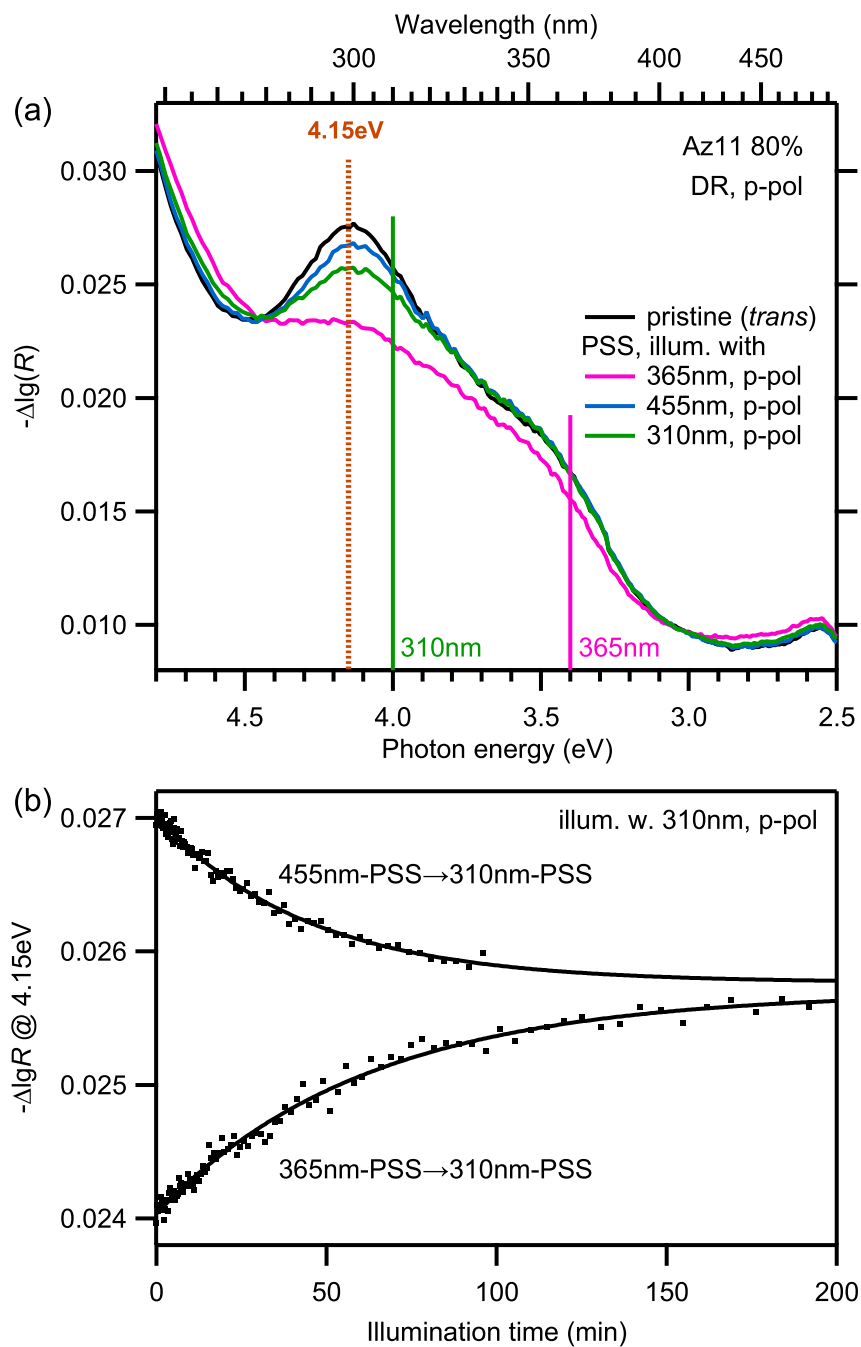
Figure 7.14: Photoisomerization experiment with p-polarized light of $\lambda_{exc} = 310\,\text{nm}$ on a $\Theta = 80\,\%$ SAM. (a) DR Spectra. The $310\,\text{nm}$-PSS lies in between the $455\,\text{nm}$- and $365\,\text{nm}$-PSSs. (a) Isomerization kinetics, starting from the $455\,\text{nm}$-PSS and the $365\,\text{nm}$-PSS.

Table 7.7: Effective[a] photoisomerization cross-sections $\tilde{\sigma}$ of a SAM with $\Theta(\text{Az11}) = 80\,\%$, for excitation wavelengths λ_{exc} (p-pol) and probing wavelengths λ_{pr} (p-pol).

λ_{exc}, pol.	Initial condition	Dominating process	$\tilde{\sigma}$ ($10^{-17}\,\text{cm}^2$)	
			$\lambda_{\text{pr}} = $ 299 nm (4.15 eV)	347 nm (3.57 eV)
365 nm, p	455 nm-PSS	t→c	0.121 ± 0.007	0.07 ± 0.02
455 nm, p	365 nm-PSS	c→t	0.082 ± 0.006	0.29 ± 0.04
310 nm, p	455 nm-PSS	t→c	0.64 ± 0.08	—[b]
310 nm, p	365 nm-PSS	c→t	0.46 ± 0.06	1.1 ± 0.3

[a] Corrected for thermal isomerization according to (2.21). This way the values are independent from the photon flux.

[b] No signal change observed

with light of 310 nm (near the maximum of the H-band) and 365 nm (see Fig. 7.14a). It can be clearly seen that the 310 nm-PSS is in between the PSSs for illumination with 365 nm and 455 nm. This indicates that by using light of 310 nm we actually switch less isomers into the *cis* state than by using light of 365 nm. Or, in other words, triggering the *trans–cis* isomerization is more effective when using light of 365 nm instead of 310 nm. This result is obtained even though the DR signal of the *trans*-Az11 SAM is bigger at 310 than at 365 nm. Apparently, the higher absorption of the *trans* isomer at 310 nm does not result in a higher fraction of *cis* isomers. In that aspect the isomerization behavior of the Az11 SAM and the Az11 solution (see Sec. 7.1.1) are similar: Also in solution a higher fraction of *cis* isomers was observed in the 365 nm-PSS than in the 310 nm-PSS (98 % instead of 48 %). This already gives us a hint that the optical excitation of the H-band of the S_2 transition (which is only present in the SAM) does not result in efficient *trans–cis* isomerization.

A better understanding of this phenomenon is gained by examining also the photoisomerization kinetics. The time constants of photoisomerization and the respective light intensities are given in Tab. 7.6. Since the 310 nm-PSS lies in between the 365 nm-PSS and the 455 nm-PSS, we recorded the kinetics of the photoisomerization starting from both PSSs (see Fig. 7.14b), in analogy to Az11 in solution. We find that both PSSs are approximately the same, whereas the time constants agree with each other within threefold error intervals only (see Tab. 7.6). A full agreement in PSS and time constants is expected for non-interacting chromophores only. This result is another indicator for a cooperative isomerization process.

From the isomerization kinetics we derived the effective photoisomerization cross-sections (Tab. 7.7). These values need to be taken with a grain of salt since the DR is not proportional to the amount of *trans* or *cis* isomers in the SAM. Nevertheless, the kinetics are meaningful, since *trans–cis* isomerization consistently results in a signal decrease in the DR signal in the spectral range of the S_2 transition.

Figure 7.15: Work-function shifts $\Delta\Phi_{\mathrm{PSS}}$ between the PSS for a specific excitation wavelength λ_1 and the PSS for $\lambda_2 = 450\,\mathrm{nm}$, i.e., with almost all molecules in the *trans* state, in a $\Theta = 50\,\%$ (top) and a $\Theta = 20\,\%$ (bottom) Az11 SAM. $\Delta\Phi_{\mathrm{PSS}}$ is an approximate measure of the fraction χ_c of *cis* isomers in the SAM. The overlain gray curves are rescaled and represent the changes in the fraction of *cis* molecules between the PSSs in solution. Taken from [106].
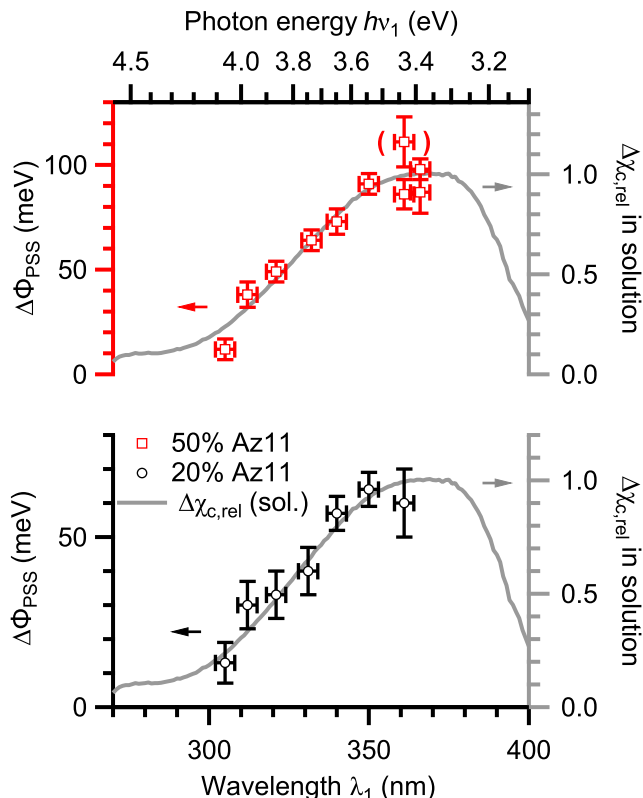
We observe that $\tilde{\sigma}(310\,\mathrm{nm})$ is bigger than $\tilde{\sigma}(365\,\mathrm{nm})$: by a factor of 4–5 and 15 for the kinetics recorded at the maximum (4.15 eV) and the low-energy shoulder of the S_2 band (3.57 eV), respectively. As mentioned in Sec. 2.1.2, the effective photoisomerization cross-section is only a measure for how fast the PSS is reached, regardless which switching processes contribute. $\tilde{\sigma}(310\,\mathrm{nm})$ is dominated by *cis*–*trans* isomerization, as evidenced by the lower number of *cis* isomers in the 310 nm-PSS than in the 365 nm-PSS. The H-band of the *trans*-Az11 SAM can be optically excited (it is visible in the DR spectra), however, this excitation leads to marginal *trans*–*cis* isomerization only.

The same observations were made for a SAM with $\Theta = 20\,\%$ as well. Also here the 310 nm-PSS lies in between the 455 nm-PSS and the 365 nm-PSS, and the effective isomerization cross section $\tilde{\sigma}(310\,\mathrm{nm})$ is bigger than $\tilde{\sigma}(365\,\mathrm{nm})$ (see Sec. B.2.2). Note that the effective isomerization cross-sections determined in the DR measurements under ambient conditions are on the same order of magnitude as the ones determined in NEXAFS in vacuum (see Tab. B.6). This indicates that the environment influences the thermal isomerization but not the photoisomerization in SAMs.

The view that exciting the H-band of the S_2 transition does not lead to efficient *trans*–*cis* isomerization is corroborated by a two-photon-photoemission (2PPE) study on Az11 SAMs [106]: This work makes use of the fact that the work function of the sample changes with isomer composition of the SAM due to different permanent dipole moments of *trans*- and *cis*-Az11. Specifically, the work function shift between the PSS for a specific excitation wavelength λ_1 in the UV range and the PSS for $\lambda_2 = 450\,\mathrm{nm}$ (predominantly *trans*) was measured on SAMs with $\Theta = 50\,\%$ (Fig. 7.15, top) and $\Theta = 20\,\%$ (bottom). We find that the work function shift is highest for a λ_1 of about 360 nm (3.4 eV) and decreases with decreasing λ_1, which corresponds to a decreasing fraction

of *cis* isomers in the respective PSS.

This behavior was compared with the expected fraction χ_c of *cis* isomers of Az11 in solution (see Fig. 7.5). For this the relative change in χ_c, $\Delta\chi_{c,rel}$, between the 455 nm-PSS ($\Delta\chi_{c,rel} = 0$) and the 365 nm-PSS ($\Delta\chi_{c,rel} = 1$) was plotted (gray solid line).[16] We find that $\Delta\chi_{c,rel}$ of Az11 in solution fits very well to the work function change in Az11 SAMs. When varying the excitation wavelength λ_1, the fraction of *cis* isomers in the PSS varies similarly for Az11 in solution and Az11 SAMs.

This is observed even though the S_2 absorption band of Az11 in solution and Az11 in SAMs are very different: Only in SAMs the H-band, which corresponds to a delocalized excitation, is present. UV light with $\lambda_1 < 330$ nm ($h\nu_1 > 3.7$ eV) increasingly excites the H-band. This excitation needs to be localized on a certain isomer in order to drive isomerization. In the delocalized excited state the TDMs of the monomers oscillate in phase (see Sec. 2.3.1). Localization means that a dephasing of the TDMs happens and the delocalized exciton decays into a localized exciton due to interaction with molecular vibrations [107]. Apparently this process is inefficient. This ultimately means that the probability of *trans–cis* isomerization after optical excitation, the *trans–cis* quantum yield, is low. Instead, *cis–trans* isomerization is triggered mainly: The *cis* isomers also absorb the UV light and the *cis* isomer has a much higher quantum yield for photoisomerization than the *trans* isomer. In contrast, with UV light of about 360 nm (3.4 eV), the *trans* chromophores at defect sites have a high absorbance and also a significant *trans–cis* isomerization quantum yield, whereas the absorbance of the *cis* isomer is marginal at this wavelength. This then results in a significant amount of *cis* isomers in the PSS.

7.2.6 Conclusions and Outlook

In this section we examined the photoisomerization and thermal isomerization of Az11 in SAMs with respect to efficiency, the influence of the environment, the chromophore density, the kinetics probed at different wavelengths and the excitation energy. The NEXAFS results showed that by illumination with UV light of 365 nm at least 50 % of the chromophores in a SAM with 20 % Az11 coverage switch into the *cis* state, only limited by the fast thermal isomerization. If thermal isomerization can be neglected, a yield of at least 67 % *cis* isomers is expected. The photoisomerization cross-sections are significantly smaller in the SAM than in solution, which we attribute to steric hindrance or excitonic coupling between the chromophores. The thermal isomerization is fast (on the order of minutes) in water-free environments such as vacuum or protective gas atmosphere but on the order of hours under ambient conditions. We attribute this to a film of adventitious water being present on the SAM in air: Water molecules are polar and stabilize the more polar *cis* conformation of Az11. However, the photoisomerization seems to be unaffected by the environment, the effective photoisomerization cross-sections examined by both NEXAFS in vacuum and DR spectroscopy under ambient conditions are on the order of 10^{-18} cm^2 (see Tab. B.6). One may speculate that the adventitious

---

[16] The relative change in $\chi_{c,rel}$ for Az11 in solution is calculated by $\Delta\chi_{c,rel}(\lambda_1) = [\chi_c(\lambda_1) - \chi_c(455\,\text{nm})] \, / \, [\chi_c(365\,\text{nm}) - \chi_c(455\,\text{nm})]$.

water has a lower influence on the electronically excited states than the ground states, thus, not influencing the photoisomerization.

Using DRS we examined the photoisomerization in SAMs in dependence on the Az11 coverage Θ and found that already a minor dilution to about 90 % (replacing less than 1 in 8 neighboring chromophores by a spacer molecule) is sufficient to observe significant photoisomerization. Also we found indications that the isomerization process is cooperative, in a sense that the isomerization probability of an isomer depends on the state of the neighboring isomers:[17] When illuminating a SAM with light of 365 nm, mainly chromophores at defect sites in the molecular crystal isomerize from *trans* to *cis*, thereby creating a defect for the neighboring *trans* chromophore, which then isomerizes with higher probability. This could be deduced in particular from the kinetics of the isomerization recorded at different wavelengths and from the fact that the biggest change in DR signal is observed in the spectral region of the H-band of the S_2 transition, which is actually not excited by UV light of 365 nm. However, when exciting the H-band directly by light of shorter wavelength, the fraction of *cis* isomers in the PSS is actually less than it is the case for excitation with light of 365 nm. This is attributed to the fact that the H-band is formed by an excitation into a delocalized excitonic state. This delocalized state does not efficiently decay into excitations that are localized onto single chromophores. Therefore, isomerization is inhibited. Instead, the shorter wavelength of light that matches the H-band of the *trans* isomer also matches the absorption band of the *cis* isomer, therefore *cis–trans* isomerization is triggered predominantly. Or, in other words, the H-band of the S_2 transition absorbs photons very well but it is not an efficient pathway for *trans–cis* photoisomerization.

---

[17] A different definition of cooperativity in isomerism is an isomerization quantum yield (2.24) $\Phi > 1$, which would mean that the absorption of one photon results in the isomerization of more than one molecule. We do not postulate cooperativity in this sense.

Chapter 8

Summary

In this work the influence of intermolecular interactions on the optical properties and the photoisomerization in azobenzene-containing self-assembled monolayers (SAMs) on gold was examined. Azobenzene is a molecular switch that can isomerize from the *trans* to the *cis* state and vice versa by optical excitation with UV and blue light, respectively. UV light matches the S_2 transition of azobenzene, whereas blue light matches the S_1 transition.

Anchoring azobenzene to a surface allows to change the properties of the surface by external stimuli, in this case by light. Self-assembly is a simple and effective method to achieve this. Alkanethiols bind to gold readily, forming the thiolate–gold bond. As confirmed by X-ray photoelectron spectroscopy (XPS), the SAMs produced in this work are chemically pure, i.e., there are no unwanted contaminants and the concentration of sulfur species other than the thiolate is less than approximately 3 %. In such SAMs the azobenzene moieties stand very close to each other and form a 2D lattice of two molecules per unit cell. This leads to excitonic coupling, i.e., the S_2 transition of the isolated azobenzene is split into a blue-shifted H-band and a red-shifted J-band.

The photoisomerization in such densely-packed SAMs of azobenzenes is quenched, which can be attributed to the lack of free space of the individual molecule to isomerize (steric hindrance) or the aforementioned excitonic coupling. Both steric hindrance and excitonic coupling are reduced by increasing the intermolecular distance, therefore we fabricated mixed SAMs of azobenzene-alkanethiols as molecular switches and simple alkanethiols as "spacers". By XPS it was found that the azobenzene-alkanethiols and simple alkanethiols mix nearly statistically, i.e., there are no large islands of the same kind of molecules. Using near edge X-ray absorption fine structure (NEXAFS) spectroscopy we determined the average orientation of the azobenzene moieties. Upon decreasing the relative coverage Θ of azobenzenes on the surface they appear to "bend down". This is also reflected in their optical properties, probed by differential reflectance (DR) spectroscopy: In the densely-packed SAM an excitonic coupling of the S_2 excitation is observed, with an intense and significantly blue-shifted H-band and a very weak red-shifted J-band. With decreasing relative chromophore coverage the blue-shift of the H-band is decreasing, which reflects a change in the chromophore–chromophore distance and the relative orientation of the chromophores. That this blue-shift is not just an artifact of the experimental method but indeed a consequence of molecular excitons, was confirmed by extracting the extinction coefficient κ of the

SAM, a material property.

The isomerization in azobenzene SAMs was studied extensively. Generally, the photoisomerization competes with the thermal *cis–trans* isomerization. In azobenzene solutions under ambient conditions the thermal isomerization proceeds on a timescale of days and can therefore be neglected. In the SAM, however, this depends on the environment: Whereas under ambient conditions a similarly large time constant of thermal isomerization as in solution was observed, the thermal isomerization of Az11 in SAMs was on the order of minutes in vacuum and protective gas atmosphere. We attribute this to a film of adventitious water being present on the SAM in air: Water molecules are polar and stabilize the more polar *cis* conformation of Az11, thereby increasing the reaction barrier for *cis–trans* isomerization. Accordingly, in environments where this water film is absent, the thermal isomerization is much faster.

A systematic study regarding the influence of the chromophore coverage on the isomerization behavior revealed that a minor dilution to about 90 % (replacing less than 1 in 8 neighboring chromophores by a spacer molecule) is already sufficient to observe a significant photoisomerization. For a relatively low chromophore coverage of 20 % we were able to quantify the photoisomerization in a SAM using NEXAFS. By illumination with UV light at least 50 % of the molecules could be switched to the *cis* state. By examining the kinetics of photoisomerization at different wavelengths of probing and excitation, we found indications for a cooperative isomerization process: Upon illumination azobenzenes at defects isomerize first, which enables the isomerization of neighboring molecules and so forth. This is in contrast to a solution of azobenzenes, where the chromophores isomerize independently. However, the isomerization cross-sections, which are a measure for the probability of a molecule to isomerize upon an impinging photon, are by one order of magnitude smaller in the SAM than in solution. This we attribute to the steric hindrance or the excitonic coupling. The optical excitation of the H-band of the S_2 transition, which is very prominent in the DR spectra of the SAM, does not lead to a significant *trans–cis* isomerization. This is attributed to the fact that the H-band is an excitation that is delocalized across many *trans* isomers. In order for a *trans* isomer to isomerize, the excitation needs to be localized onto a single *trans* isomer, which is inefficient. Instead, the optical excitation in a spectral range attributed to localized excitons allows significant *trans–cis* isomerization.

In conclusion, in order to prepare photoswitchable azobenzene-containing SAMs, enough space between the azobenzene moieties needs to be provided. Probing the absorption profile of the SAM by optical spectroscopy allowed us to determine the extend of excitonic coupling and therefore the intermolecular interactions that hinder photoisomerization.

Chapter 9

Methods and Materials

9.1 General

All work with solutions and SAMs of azobenzene derivatives was performed under yellow light with a cutoff wavelength of 550 nm, in order to avoid unintentional photoisomerization.

Disposable materials were used for liquid handling. All disposable materials were checked for extractables prior to use: UV/vis spectra of ethanol were recorded before and after rinsing of the vessels, pipette tips, syringes and syringe filters. For syringes we were not able to find a brand that did not release intolerable amounts of substances absorbing at low wavelength. Thus, the syringes were rinsed with solvent before use.

9.2 Sample Preparation

9.2.1 Substrates

Gold Single Crystals   Gold single crystals with (111) surface (area of $10 \times 13 \, mm^2$, thickness of 2 mm) were obtained from MaTeck GmbH, Jülich, Germany. Before use as substrate for SAMs, we performed several cycles of sputtering and annealing in vacuo: First, the crystal was sputtered with Ar ions for 10 minutes, maintaining a sputtering current of 8 µA at an acceleration voltage of 800 V. Second, the crystal was annealed at 610 °C for 10 minutes, with heating and cooling rates of $1 \, K \, s^{-1}$. Cycles of sputtering and annealing were performed until the herringbone surface reconstruction [108, Fig. 7] was visible in low energy electron diffraction (LEED). After initial preparation of the pristine Au crystal, two cycles of sputtering and annealing were usually required before the crystal was used for a new SAM preparation.

Gold/mica sheets   Sheets of epitaxial gold (300 nm thickness) on mica were obtained from Georg Albert PVD-Beschichtungen, Silz, Germany. They were annealed by the manufacturer to obtain large (111) terraces. The sheets had a size of $75 \times 25 \, mm^2$ and were cut into pieces of $10 \times 25 \, mm^2$ (samples for DR spectroscopy) or $10 \times 12 \, mm^2$ (samples for XPS and NEXAFS). The cut gold/mica pieces were stored under argon atmosphere for later use.

9.2.2   SAM-forming Thiols and Solvents

Az11   (11-(4-(Phenyldiazenyl)phenoxy)undecane-1-thiol) [48, Supporting Information] was a courtesy of R. Klajn, Department of Organic Chemistry, Weizmann Institute of Science, 76100 Rehovot, Israel.   The compound is also commercially available (ProChimia Surfaces Sp. z o.o., Sopot, Poland, https://www.prochimia.com).

C12   (1-Dodecanethiol (98 %), Alfa Aesar) was used as obtained.

Methanol   Methanol of HPLC grade was used.

9.2.3   Preparation of SAMs

Mixed SAMs of Az11 and C12 were prepared by immersing the gold substrates into a methanolic solution of both thiols with a total thiol concentration of 0.1 mM. If two identical samples were required, they were immersed back to back into the same incubation solution. The incubation solutions were prepared from stock solutions (see below). We used flat-bottom glass vials[1] with a diameter chosen so that the samples were forced to stand upright and could not lie flat on the bottom. The vials were covered with cover slips to reduce evaporation from the incubation solution. After an incubation time of 20 ± 0.5 h the samples were removed using a pair of cover slip tweezers. They were rinsed thoroughly with methanol using a glass Pasteur pipette and it was taken care to rinse the tweezers also. Then, samples were picked up with a second pair of tweezers at the opposite edge and rinsed again. Finally the samples were blown dry with argon in such a way that the space between the tweezers was dried as well and that no solvent was blown onto the sample. The samples were put into fresh glass vials and stored under argon.

Az11 Stock Solutions   Methanolic solutions of Az11 were prepared by sonication and warming to 40 ℃ for $\approx$ 10 minutes. Typically, a small amount of a disperse solid residue could be observed. We assume this residue is the corresponding disulfide, as more of it precipitates when kept at room temperature for more than one day. The suspensions were filtered through 0.2 μm PTFE-membrane syringe filters. The purity of the filtrate was checked by ultrahigh-performance liquid chromatography. The filtrate was used as stock solution. Due to the unknown amount of residue filtered off, the concentration of this stock solution had to be determined photometrically, as described below. The concentrations were typically $\approx$ 0.4 mM. Prepared stock solutions were stored in the freezer for up to four weeks and were allowed to heat up to room temperature before opening the flask. Typically a small amount of precipitation could be observed, therefore we sonicated the flask, heated to 40 ℃ for $\approx$ 10 minutes, allowed cooling to room temperature, and then verified that no precipitate was visible any more before use.

---

[1]   Carl Roth Art. No. H306.1, borosilicate glass, flat bottom, 4 ml, o.d. 14.5 mm, i.d. 12 mm. The polythene stoppers included with the vials were not used as UV/vis spectra showed that they contained substances extractable with ethanol.

Photometric Determination of Az11   Stock solutions were diluted to a nominal concentration of 0.03 mM and the absorbance in the main band at $\lambda_{max} = 347$ nm was compared with the absorption coefficient $\varepsilon_{max} = (27.3 \pm 0.3) \times 10^6 \, cm^2 \, mol^{-1}$ of Az6 (6-4-[phenyldiazenyl]phenoxyhexane-1-thiol) in methanol, a compound with the same chromophore that dissolves completely and shows an absorbance spectrum indistinguishable from the one of Az11. The absorption coefficient of Az6 was determined from ≈ 0.03 mM solutions prepared by adding the appropriate amount of methanol by weight to weighed samples dried over P_4O_{10} in vacuum for 24 h.

C12 Stock Solutions   1 mM stock solutions of 1-dodecanethiol (C12) were prepared by diluting the liquid compound in 2 steps, assuming a density[2] of $0.845 \, g \, cm^{-3}$. The stock solutions were stored in a fridge and warmed to room temperature before re-opening the flask.

9.3   Absorbance Spectroscopy

In UV/vis experiments of Az11 solutions we recorded spectra in steps of 1 nm with a spectral resolution of 2 nm.

Photometric Measurements   In measurements to determine Az11 concentrations we used disposable UV cells.[3] We prepared a cell with just the solvent and cell(s) with azo solution(s). The reference path was left empty and we performed measurements with solvent and sample(s) in the sample beam for baseline and sample measurement(s), respectively. Integration time was 0.04 s per point.

To be able to photometric measurements also with the DR setup (cf. Fig. 3.11) in place, we mounted a gold/mica sample onto the sample holder, added a cell holder to the rear beam path and treated the rear and front beam paths as sample and reference path, respectively. We then performed baseline and sample measurements as described above. An integration time of 0.12 s per point yielded a sufficient signal-to-noise ratio.

Photoisomerization Experiments   In photoisomerization experiments of Az11 solutions we used fused silica cells (macro or half-micro). We performed a baseline measurement with solvent in both beam paths, then discarded the content of the cell in the sample path, dried the cell with argon, added the Az11 solution, and then performed a sample measurement. The photoisomerization was examined by sequentially illuminating the cell ex situ and recording an absorbance spectrum. These steps were continued until no further spectral change was observed.

A low concentration of Az11 was chosen ($\approx 1.8 \times 10^{-6}$ M), resulting in a maximum absorbance of about 0.04, which corresponds to a transmission of 90 %. This way the intensity of the external light that triggers the photoisomerization is approximately homogeneous along the path through the cell,

---

[2]   1-Dodecanethiol (98%), Alfa Aesar Online Catalog, https://www.alfa.com, Art. No. A12741

[3]   Semi-micro disposable UV cells, Brand GmbH & Co. KG, Germany, Cat. No. 759150

Table 9.1: XPS photon energies (in eV).

	$h\nu$	harmonic
S 2p	260	1st
C 1s	400	3rd
N 1s	500	3rd
O 1s	650	3rd

which is required to determine the isomerization kinetics. Because of the low Az11 concentration integration times of up to 0.6 s per point were required for a sufficient signal-to-noise ratio.

9.4 XPS and NEXAFS

Photoelectron spectra and Auger electrons for Auger yield NEXAFS were recorded at the synchrotron facility BESSY II using an Omicron EA125 hemispherical electron analyzer with a five channel detector. The undulator beamline UE56-2 PGM-2 was used for all measurements present in this thesis. The width of the monochromator exit slit was set to 30 μm (energy resolution of 1:80,000 at 64 eV). The measurement geometries for XPS and NEXAFS have already been shown in Figs. 3.2 and 3.7, respectively. The exit slit of the electron analyzer was in the fully open position for all measurements.

9.4.1 XPS

Experimental All XP binding energies were referenced to the substrate's Au4f$_{7/2}$ peak at a binding energy of 83.95 eV [64]. XP spectra were recorded using vertically polarized radiation, and the following electron analyzer settings: central analyzer energy (CAE, pass energy) 5 eV, step size 0.05 eV, and dwell time 0.2 s. For C 1s spectra one scan was sufficient, for the other elements typically 5 scans measured on the same spot were summed resulting in a total integration time of 1 s per data point. Table 9.1 gives photon energies and diffraction order of the beamline monochromator used for XPS. The gold reference spectra were measured with the same photon energy as the respective S 2p, C 1s, N 1s, O 1s spectra.

Analysis In this work XPS peaks were modeled using the Voigt function, a convolution of a Lorentzian with a Gaussian. Since the Voigt function has no analytical representation, it was numerically evaluated. We used the approximation described by Schreier [109, 110] and implemented in the data analysis software Igor Pro as described in its documentation [111]:

$$g_V(E - \hat{E}, \gamma_L, \gamma_G) = \frac{\sqrt{\ln 2/\pi}}{\gamma_G} K(x, y); \quad K(x, y) = \frac{y}{\pi} \int_{-\infty}^{\infty} \frac{e^{-t^2}}{(x-t)^2 + y^2} dt, \tag{9.1}$$

with E being the binding energy, $\hat{E}$ being the peak position, and γ_L and γ_G being the half width at half maximum of the Lorentzian and the Gaussian, respectively. $K(x, y)$ is the function actually approximated.[4] Its parameters

---
[4] This is the function voigt(x,y) in Igor Pro.

are defined as:

$$x = \frac{\sqrt{\ln 2}}{\gamma_\mathrm{G}}(E - \hat{E}) \quad \text{and} \quad y = \sqrt{\ln 2}\,\frac{\gamma_\mathrm{L}}{\gamma_\mathrm{G}} \tag{9.2}$$

Thus, a single Voigt peak at position $\hat{E}$ is given by

$$\mathrm{singlet}(E; \hat{E}, a, w, y) = a\,K\big(w \cdot (E - \hat{E}), y\big), \tag{9.3}$$

where the amplitude parameter a, the width parameter w and the shape parameter y typically are free parameters in the fit. The Gauss width γ_G and the Lorentz width γ_L can be determined according to the equations given in [111]. For the S 2p and Au 4f peak doublets two Voigt peaks with common width parameter, shape parameter, and amplitude parameters were used. The peak amplitude ratio r was set to the theoretical value according to the L-S coupling (cf. Sec. 3.1.3) and a doublet energy splitting s was used:

$$\begin{aligned}
\mathrm{doublet}(E; \hat{E}, a, w, y; r, s) &= \mathrm{singlet}(E; \hat{E}, a, w, y) \\
&\quad + r \cdot \mathrm{singlet}(E; \hat{E} + s, a, w, y)
\end{aligned} \tag{9.4}$$

As background a sum of a linear and a Shirley type background were used. The Shirley background was determined by integrating the peak model function:

$$\mathrm{background} = b + mE + p \int_{\infty}^{E} \mathrm{d}E' \mathrm{peaks}(E'; \text{peak parameters}), \tag{9.5}$$

with b and m being the coefficients of the linear background and p being the proportionality factor between peak area and Shirley background.

9.4.2 NEXAFS

Both C 1s and N 1s spectra were recorded using horizontally polarized light of the 1st harmonic of the beamline monochromator. To detect the Auger electrons the analyzer's pass energy was set to its maximum value of 50 eV for maximum transmission. This setting corresponds to a 5 eV wide electron energy detection window. Spectra were recorded at nominal electron kinetic energies, i.e., not corrected for the analyzer work function, of 259 eV for C 1s and 377 eV for N 1s spectra. A Hamamatsu G2119-01 photodiode with $10 \times 10\,\mathrm{mm}^2$ active area connected to a Keithley Model 6514 Electrometer was used to measure the X-ray flux. The photon energy was scanned stepwise, integration time was 1 s per data point. Generally the $\pi^\star$ region (C 1s: 280–295 eV, N 1s: 392–410 eV) was scanned with 0.1 eV, the rest of the spectrum (C 1s: 294–330 eV, N 1s: 409–430 eV) with 0.5 eV steps. For high-resolution spectra of the $\pi^\star$ excitation the we scanned the $\pi^\star$ region (C 1s: 283–290 eV, N 1s: 396–401 eV) with a step size of 0.02 eV and the post-edge region (C 1s: 320–330 eV, N 1s: 425–432 eV) with a step size of 0.5 eV. N 1s NEXAFS kinetics measurements of the isomerization in Az11 SAMs were performed at a nominal photon energy of 398.4 eV.

The photon energy calibration of NEXAFS spectra was performed according to reference measurements on nitrogen gas (N 1s) and graphite (C 1s), as

Table 9.2: NEXAFS Photon energy corrections (in eV).

		$h\nu$ corr.	
Beamtime	Measurements	N 1s	C 1s
Jun 2012	Chromophore Orientation, Chap. 5	0.59	0.26
Feb 2014	Photoisomerization, Secs. 7.2.1 and B.1.2	0.69	0.26

described in Sec. 3.2.6. In the case of the beamtime in June 2012, no nitrogen gas reference was available, therefore the photon energy offsets in the N 1s spectra was chosen so that they matched the spectra of the February 2014 beamtime. The resulting values are given in Tab. 9.2.

9.5   DR Spectroscopy

9.5.1   Experimental

Spectra   DR Spectra were recorded with s- or p-polarized light in steps of 1 nm with a spectral resolution of 2 nm, with 1 or 2 s of integration time per point.

Kinetics   In order to record the photoisomerization kinetics of azobenzene SAMs we sequentially measured the DR signal and illuminated the sample with external light of a selected LED (cf. Fig. 3.11) for a certain time interval. The DR signal was recorded at selected wavelengths (spectral resolution of 2 nm): At the maximum of the blue-shifted S_2 band (at 299 nm in the case of the SAM with $\Theta(Az11) = 80\%$), the maximum of the S_2 band in solution (347 nm), and at 550 nm, well outside the S_1 band, the lowest-energy electronic transition. The measurement at 550 nm was used to monitor possible temporal drifts unrelated to azobenzene photoisomerization. We performed about 100 cycles of measuring and illumination: We first measured the DR signal at the selected wavelengths for 5 s each, then the mirror M6 was flipped into the beam path and the shutter S was opened for a few seconds. The total illumination time was set to about three times the time constant determined from a series of exploratory experiments. Note that before and after such a kinetics measurement we always recorded a full spectrum.

The thermal isomerization is generally much slower than the photoisomerization, therefore full spectra were recorded in certain time intervals and the data was then evaluated at certain wavelengths.

In the photoisomerization and thermal isomerization measurements the signal change at 550 nm was interpreted as a thermal drift of the experimental setup itself and was subtracted from the curves. Thermal drift was reduced to a minimum by working under air conditioning and monitored with Pt100 temperature resistors.

9.5.2 Analysis

DR spectra of SAMs were fit according to the equations deduced in Sec. 2.3.2: The differential reflectance of a gold substrate (medium 3) covered by molecular layer (medium 2) of thickness d in air (medium 1) is given by

$$-\Delta \lg R = -\lg\left(\frac{|r_{123}(d)|^2}{|r_{123}(d=0)|^2}\right) + \text{offset}, \qquad (9.6)$$

with an offset as a free parameter. The reflection coefficient r_{123} was calculated according to

$$r_{123} = \frac{r_{12} + r_{23}\,e^{i\delta}}{1 + r_{12}r_{23}\,e^{i\delta}}; \quad \delta = 2\,k_{z,2}\,d, \qquad (9.7)$$

with the Fresnel coefficients r_{12} and r_{23} (which depend on the refractive indices of the respective layers, the polarization, and the angle of incidence $\theta_1 = 45°$), and the wave's z component $k_{z,2}$ in the layer. The refractive index $\tilde{n}_1$ of the environment (air) was set to 1. The refractive index $\tilde{n}_2 = \sqrt{\epsilon_2}$ of the molecular layer was modeled according to

$$\epsilon_2 = \epsilon_{\text{const}} + \sum_{j=0}^{7}\frac{f_j}{(h\nu_j)^2 - (h\nu)^2 - i(h\nu)\gamma_j}, \qquad (9.8)$$

with a constant ϵ_{const}, oscillator strengths f_j, resonance energies $h\nu_j$, damping constants γ_j, and photon energy $h\nu$. The refractive index $\tilde{n}_3$ of the gold substrate was taken from [77].

The parameters $\epsilon_{\text{const}} = 1.3$ and film thickness $d = 2\,\text{nm}$ (see Sec. 6.2) were fixed for all fits. ϵ_{const} was chosen so that the real part of ϵ_2 approached a value of about 2 for low photon energies (the static permittivity of dodecane is 2 [112, Sec. 6]).

9.6 Characterization of LED Light Sources

Spectral Characteristics LED lamps in the UV and blue spectral range were used to trigger photoisomerization in Az11 SAMs and Az11 solutions. Emission spectra of the LED lamps were recorded with an Avaspec 2048 spectrometer (spectral characteristics given in Tab. 9.3).

Light Intensities in Experiments with Az11 Solutions In photoisomerization experiments of Az11 solutions (cf. Tab. 7.1) the light of the LEDs was collimated with 50 mm optics so that the cell could be homogeneously illuminated. The intensity of the light was then measured with a Melles Griot 13PEM001 powermeter (diameter of active area of approx. 10 mm).

Light Intensities in Experiments with Az11 SAMs In NEXAFS measurements the LED light was collimated to a diameter of 50 mm, well bigger than the sample. The intensity of the light in sample distance was measured with a Melles Griot 13PEM001 powermeter.

In DR measurements the light of the LEDs was collimated and cut with a rectangular aperture so that their spot on the sample was well bigger than

Table 9.3: Central wavelength λ, central photon energy E_{ph}, and the respective full width at half maximum (FWHM) of the external light sources used in photoisomerization experiments of Az11 solutions and Az11 SAMs.

	λ (nm)	FWHM	E_{ph} (eV)	FWHM
LED array[a]	460	26	2.70	0.15
Thorlabs M455L2	455	20	2.73	0.12
Thorlabs M365L2	365	11	3.40	0.10
Thorlabs M310L3	310	10	4.00	0.13

[a] Used only in the experiments of Fig. 7.11

the spot of the spectrometer lamps. The intensity of the light on the sample was determined in the following way: A photodiode (Hamamatsu S1337-33BQ, photosensitive area of $2.4 \times 2.4\,\text{mm}^2$) was placed on the sample holder in normal incidence and the photodiode current was measured with a Keithley Model 6514 electrometer. The photodiode was calibrated with the Melles Griot 13PEM001 powermeter. Since the external light in the photoisomerization experiments hits the sample under an angle of incidence of 45°, the intensities are finally multiplied by $\cos 45°$. The resulting intensities on the sample are given in Tab. B.5.

Appendix A

Evaluation of Isomerization Kinetics

A.1 Photoisomerization of Az11 Solutions

A.1.1 Fraction of *cis* Isomers in the PSSs

Illumination with 365 nm   The fraction of *cis* isomers in the 365 nm-PSS was determined by reconstructing the absorbance spectrum of the *cis* isomer. The spectrum $A_{PSS}(\lambda)$ of every mixture of isomers obtained in a PSS can be written as a linear combination of the spectra $A_t(\lambda)$ and $A_c(\lambda)$ of the two isomers:

$$A_{PSS}(\lambda) = (1 - \chi_{c,PSS})\, A_t(\lambda) + \chi_{c,PSS}\, A_c(\lambda). \tag{A.1}$$

Therefore:

$$A_c(\lambda) = \frac{A_{PSS}(\lambda) - (1 - \chi_{c,PSS})\, A_t(\lambda)}{\chi_{c,PSS}}. \tag{A.2}$$

When applying this equation using the spectrum of the 365 nm-PSS and different values for $\chi_{c,PSS}(365\text{nm})$, we find that the 365 nm-PSS contains at least 96 % *cis* molecules: For $\chi_{c,PSS}(365\text{nm}) < 96\,\%$ a negative absorbance of the *cis* isomer would be observed at about 370 nm, which is unphysical (cf. Fig. A.1). The upper limit for $\chi_{c,PSS}$ is 100 % and we therefore give the fraction of *cis* molecules as $98 \pm 2\,\%$.

Illumination with 455 and 310 nm   In the photoisomerization experiments with 455 and 310 nm the fraction of *cis* isomers was obtained in the following way: The absorbance of the *cis* form of Az11 at 380 nm is close to zero (cf. Fig. 7.1). Therefore we can assume that the fraction of *trans* molecules in a PSS is directly proportional to the absorbance $A_{PSS}(380\text{nm}) \equiv A'_{PSS}$:

$$\chi_{t,PSS} \approx \frac{A'_{PSS}}{A'_t} \tag{A.3}$$

This is only the upper limit since the *cis* species has a very minor remaining absorbance. A lower limit can be obtained by subtracting this remaining absorbance from the numerator and the denominator, respectively. Since the spectrum of the pure *cis* cannot be obtained photochemically, we approximate the *cis* spectrum with the one of the 365 nm-PSS, which contains almost
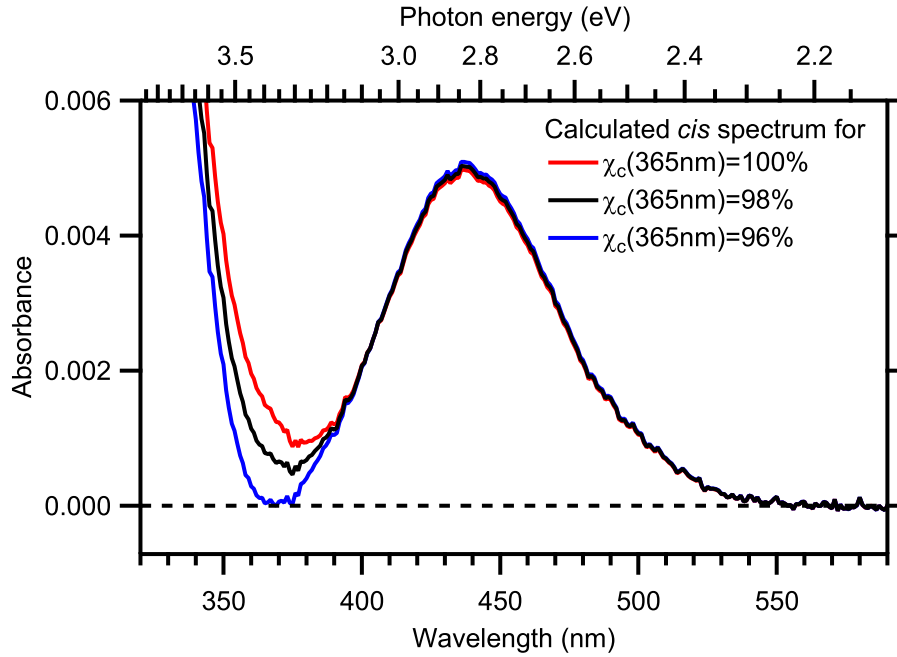
Figure A.1: Calculated spectrum of the pure *cis* isomer for different values of the fraction of *cis* isomers χ_c in the 365 nm-PSS. For $\chi_c < 96\,\%$ the calculated spectrum of the *cis* becomes negative at about 370 nm, which is unphysical. This means the 365 nm-PSS contains at least 96 % *cis* isomers.

exclusively *cis* molecules:

$$\frac{A'_{\text{PSS}}}{A'_{\text{t}}} > \chi_{\text{t,PSS}} > \frac{A'_{\text{PSS}} - A'_{\text{365nm-PSS}}}{A'_{\text{t}} - A'_{\text{365nm-PSS}}} \tag{A.4}$$

By employing $\chi_c = 1 - \chi_t$, we can rearrange the inequalities for χ_c:

$$1 - \frac{A'_{\text{PSS}}}{A'_{\text{t}}} < \chi_{\text{c,PSS}} < 1 - \frac{A'_{\text{PSS}} - A'_{\text{365nm-PSS}}}{A'_{\text{t}} - A'_{\text{365nm-PSS}}} \tag{A.5}$$

These inequalities were then used to calculate $\chi_{\text{c,PSS}}$ in the cases of illumination with 455 and 310 nm (cf. Tab. 7.1).

A.1.2 Absorption Cross-Sections of the *trans* and *cis* Isomers

By employing (3.13), cross-sections $\sigma^{\text{abs}}(\lambda)$ of the *trans* and *cis* isomer were calculated from the absorbance spectra[1] $A(\lambda)$:

$$\sigma^{\text{abs}}(\lambda) = \frac{\ln(10)}{N_{\text{A}}}\, \varepsilon(\lambda) \overset{(3.17)}{=} \frac{\ln(10)}{N_{\text{A}}} \frac{A(\lambda)}{c\, l} \tag{A.6}$$

The concentration c of Az11 in solution does not change by isomerization. It is given by

$$c = \frac{A_{\text{t}}(347\text{nm})}{\varepsilon_{\text{t}}(347\text{nm})\, l}, \tag{A.7}$$

---

[1] As spectrum of the *cis* isomer we used the one calculated in Sec. A.1.1.

with the absorbance spectrum $A_t(\lambda)$ of the *trans* isomer and the molar extinction coefficient $\varepsilon_t(347\text{nm}) = 27.3 \times 10^6 \,\text{cm}^2\,\text{mol}^{-1}$ of the *trans* isomer (cf. p. 107). By inserting (A.7) into (A.6) we obtain

$$\sigma^{\text{abs}}(\lambda) = \frac{\ln(10)}{N_A} \frac{A_t(347\text{nm})}{\varepsilon_t(347\text{nm})} A(\lambda). \tag{A.8}$$

A.1.3 Ratio of *cis–trans* and *trans–cis* Quantum Yields

The *cis–trans* isomerization quantum yield is given by

$$\Phi_c = \frac{\sigma_c^{\text{ph}}}{\sigma_c^{\text{abs}}} = \frac{k_c^{\text{ph}} J}{\sigma_c^{\text{abs}}}, \tag{A.9}$$

with the *cis–trans* isomerization cross-section σ_c^{ph}, the absorption cross-section σ_c^{abs} of the *cis* molecule, the *cis–trans* photoisomerization rate-constant k_c^{ph}, and the photon flux J. An analogous equation can be written for the *trans–cis* isomerization quantum yield Φ_t. Therefore, the ratio Φ_c/Φ_t of photoisomerization quantum yields can be written as

$$\frac{\Phi_c}{\Phi_t} = \frac{k_c^{\text{ph}}}{k_t^{\text{ph}}} \frac{\sigma_{\text{abs,t}}}{\sigma_{\text{abs,c}}} \tag{A.10}$$

The rate constants in the case of negligible thermal isomerization are (cf. Eqs. 2.16 and 2.17):

$$k_t^{\text{ph}} = \tilde{k}\,\chi_c \tag{A.11}$$

$$k_c^{\text{ph}} = \tilde{k}\,(1 - \chi_c), \tag{A.12}$$

with $\tilde{k}$ being the effective rate constant and χ_c being the fraction of *cis* molecules in the photostationary state. The ratio $\sigma_{\text{abs,t}}/\sigma_{\text{abs,c}}$ is equal to the respective ratio A_t/A_c of absorbances (see Sec. A.1.2). The ratio of quantum yields for illumination with 310 nm-light can therefore be written as

$$\left.\frac{Q_{ct}}{Q_{tc}}\right|_{310\,\text{nm}} = \frac{1 - \chi_c(310\,\text{nm})}{\chi_c(310\,\text{nm})} \frac{A_t(310\,\text{nm})}{A_c(310\,\text{nm})}. \tag{A.13}$$

A.2 Correcting for the X-ray Beam Damage in NEXAFS Kinetics

Due to radiation damage during a NEXAFS kinetics measurement the total number N of Az11 molecules in the SAM is not constant but decreases over time. We assume an exponential decay with N_0 being the total number of molecules at $t = 0$ and k_{rad} being the decay rate-constant:

$$N(t) = N_0\,e^{-k_{\text{rad}}t} \tag{A.14}$$

Using this relation and the definition of the mole fraction of *cis* molecules (2.2), the number of molecules in the *cis* state can be written as

$$N_c(t) = N_0\,e^{-k_{\text{rad}}t}\,\chi_c(t). \tag{A.15}$$

In order to trace the isomerization kinetics, we recorded the Auger electron yield $A_{\mathrm{Auger}}(t)$ at the trailing edge of the $\pi^\star$ excitation ($h\nu = 399.1\,\mathrm{eV}$, dashed line in Fig. 7.7). For this photon energy we assume that the Auger yield $A_{\mathrm{Auger}}(t)$ is linear in $N_{\mathrm{c}}(t)$ and $N_{\mathrm{t}}(t) = N(t) - N_{\mathrm{c}}(t)$, with a_{c} and a_{t} being the respective coefficients, plus a constant background C of secondary electrons:

$$
\begin{aligned}
A_{\mathrm{Auger}}(t) &= a_{\mathrm{c}}\, N_{\mathrm{c}}(t) + a_{\mathrm{t}}\,[N(t) - N_{\mathrm{c}}(t)] + C \\
&= (a_{\mathrm{c}} - a_{\mathrm{t}})\, N_{\mathrm{c}}(t) + a_{\mathrm{t}}\, N(t) + C
\end{aligned}
\tag{A.16}
$$

Using (A.14) and (A.15), we obtain:

$$
A_{\mathrm{Auger}}(t) = N_0\, e^{-k_{\mathrm{rad}}t}\,[(a_{\mathrm{c}} - a_{\mathrm{t}})\, \chi_{\mathrm{c}}(t) + a_{\mathrm{t}}] + C
\tag{A.17}
$$

In Sec. 2.1.2 we derived an expression for $\chi_{\mathrm{c}}(t)$:

$$
\chi_{\mathrm{c}}(t) = \frac{k_{\mathrm{t}}^{\mathrm{ph}}}{\tilde{k}} + \left(\chi_{\mathrm{c},0} - \frac{k_{\mathrm{t}}^{\mathrm{ph}}}{\tilde{k}} \right) e^{-\tilde{k}t}
\tag{A.18}
$$

We insert this into the expression of the Auger electron yield (A.17):

$$
A_{\mathrm{Auger}}(t) = N_0\, e^{-k_{\mathrm{rad}}t} \times
$$
$$
\left[(a_{\mathrm{c}} - a_{\mathrm{t}}) \frac{k_{\mathrm{t}}^{\mathrm{ph}}}{\tilde{k}} + a_{\mathrm{t}} + (a_{\mathrm{c}} - a_{\mathrm{t}}) \left(\chi_{\mathrm{c},0} - \frac{k_{\mathrm{t}}^{\mathrm{ph}}}{\tilde{k}} \right) e^{-\tilde{k}t} \right] + C
\tag{A.19}
$$

Finally we want to correct the Auger yield (A.19) for the beam damage in order to be able to fit the transient Auger signal with a single exponential function. For this we subtract the constant C, divide by $\exp(-k_{\mathrm{rad}}\, t)$ and then obtain the following expression for the corrected Auger yield $A_{\mathrm{Auger}}^{\mathrm{corr}}(t)$:

$$
A_{\mathrm{Auger}}^{\mathrm{corr}}(t) = N_0 \left[(a_{\mathrm{c}} - a_{\mathrm{t}}) \frac{k_{\mathrm{t}}^{\mathrm{ph}}}{\tilde{k}} + a_{\mathrm{t}} \right] + N_0\, (a_{\mathrm{c}} - a_{\mathrm{t}}) \left(\chi_{\mathrm{c},0} - \frac{k_{\mathrm{t}}^{\mathrm{ph}}}{\tilde{k}} \right) e^{-\tilde{k}t}
\tag{A.20}
$$

In order to perform this correction for our data, the offset C was read from uncorrected spectra below the N 1s edge and the rate constant k_{rad} was determined by fitting an exponential function to the sections of data assigned to the *trans* species (cf. Fig. 7.8a). We obtained time constants $\tau_{\mathrm{rad}} = k_{\mathrm{rad}}^{-1}$ on the order of 4 hours and 1 hour in experiments at $110\,\mathrm{K}$ and at room temperature, respectively. This difference in time constants is in agreement with the observation that X-ray beam damage is strongly increased at higher temperatures [67].

Appendix B

Additional Data

B.1 XPS and NEXAFS

B.1.1 XPS

Table B.1: Peak parameters of the S 2p XP spectrum in Fig. 4.1. The doublet energy splitting was fixed at 1.22 eV, determined from spectra which could be described by only one doublet.

	BE (eV)	FWHM (eV)	peak area (%)
S 2p$_{3/2}$, doublet 1	161.0	0.4	12
S 2p$_{3/2}$, doublet 2	162.0	0.4	88

Table B.2: Peak parameters of the XP spectra in Figs. 4.2 and 4.3.

Θ(Az11)	Binding energy and full width at half maximum (in eV)						
	S 2p$_{3/2}$		C 1s #1		C 1s #2	C 1s #3	
100 %	162.0	0.4	284.2	0.6	284.8	0.8	286.2	0.7
20 %	162.0	0.4	284.8	0.8	285.3	0.8	286.5	0.8
0 %	162.0	0.4	284.9	0.9	-		-	
	O 1s		N 1s #1		N 1s #2	N 1s #3	
100 %	533.0	1.0	399.5	0.8	401.5	0.7	402.9	1.0
20 %	533.2	1.3	400.0	1.0	-		-	

B.1.2   C 1s NEXAFS Spectra
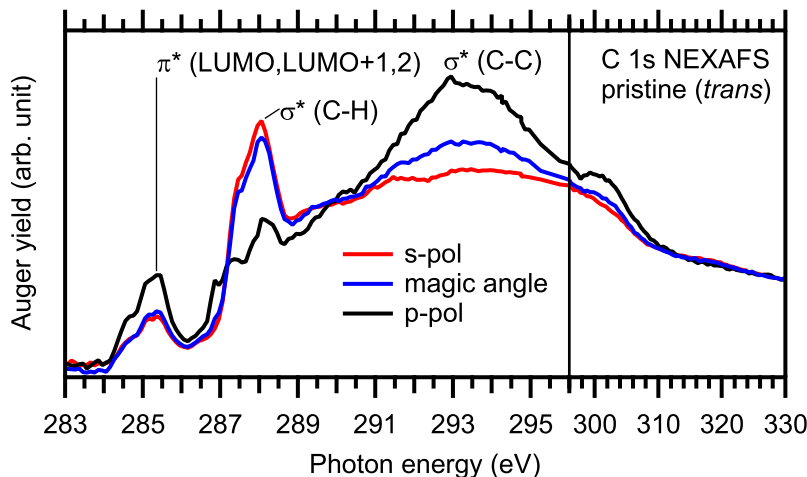
Figure B.1: C 1s NEXAFS spectra of a SAM with 20 % Az11 coverage for different X-ray polarizations. Peak assignments according to Sec. 5.1.

In Fig. B.1 C 1s NEXAFS spectra of a pristine (pure *trans*) SAM with 20 % Az11 coverage for three different X-ray polarizations are shown. A detailed description of C 1s NEXAFS spectra of Az11 SAMs can be found in Sec. 5.1.

Fig. B.2 shows spectra of the pristine state and after illumination with 365 and 455 nm light. In the case of spectra measured with X-ray light in p-polarization and in magic angle some changes could be observed: There is a signal decrease at the $\sigma^\star$ resonance (ca. 293 eV) in the three consecutive measurements, therefore we attribute this to X-ray radiation damage. The $\pi^\star$ excitations at 285 eV change reversibly upon illumination: the peak structure in the 365 nm-PSS is different than in the pristine state and the 455 nm-PSS. This is in particular visible for the measurement with p-polarized light.

In order to examine the $\pi^\star$ excitations of the *trans* and *cis* isomer in detail, we performed high-resolution scans for the three X-ray polarizations (Fig. B.3). In the *trans* species we observe maxima at 284.5, 285.1 and 285.3 eV. The lowest-energy peak at 284.5 eV can be assigned to the LUMO excitation of the *trans* isomer, whereas the higher peaks may be assigned to the LUMO+1 and LUMO+2 orbitals. We observe that upon illumination with light of 365 nm the shape of the $\pi^\star$ excitations changes: There appears to be a shift in intensity from the first to the second peak. This is reversed by illumination with 455 nm light. Using the method described for the N 1s NEXAFS spectra (Sec. 7.2.1.1) we constructed the spectra of the pure *cis* SAM from the spectra of the *trans* SAM and the spectra of the 365 nm-PSS. We find that for all X-ray polarizations the spectra of the *cis* state have a lower intensity at 284.5 eV and a higher intensity at 285.1 eV than the spectra of the *trans* state. As mentioned above, in the *trans* state the peak at 284.5 eV can be assigned to the 1s→$\pi^\star$ (LUMO) excitation. However, a diminishing of the LUMO orbital in the *cis* state seems rather implausible. Instead, because a shift of the LUMO to higher energy was also observed in the N 1s NEXAFS results (Sec. 7.2.1.1), it seems more plausible that also in the C 1s NEXAFS we observe a shift of the energetic position of the LUMO, whereas the higher orbitals remain relatively unchanged. This
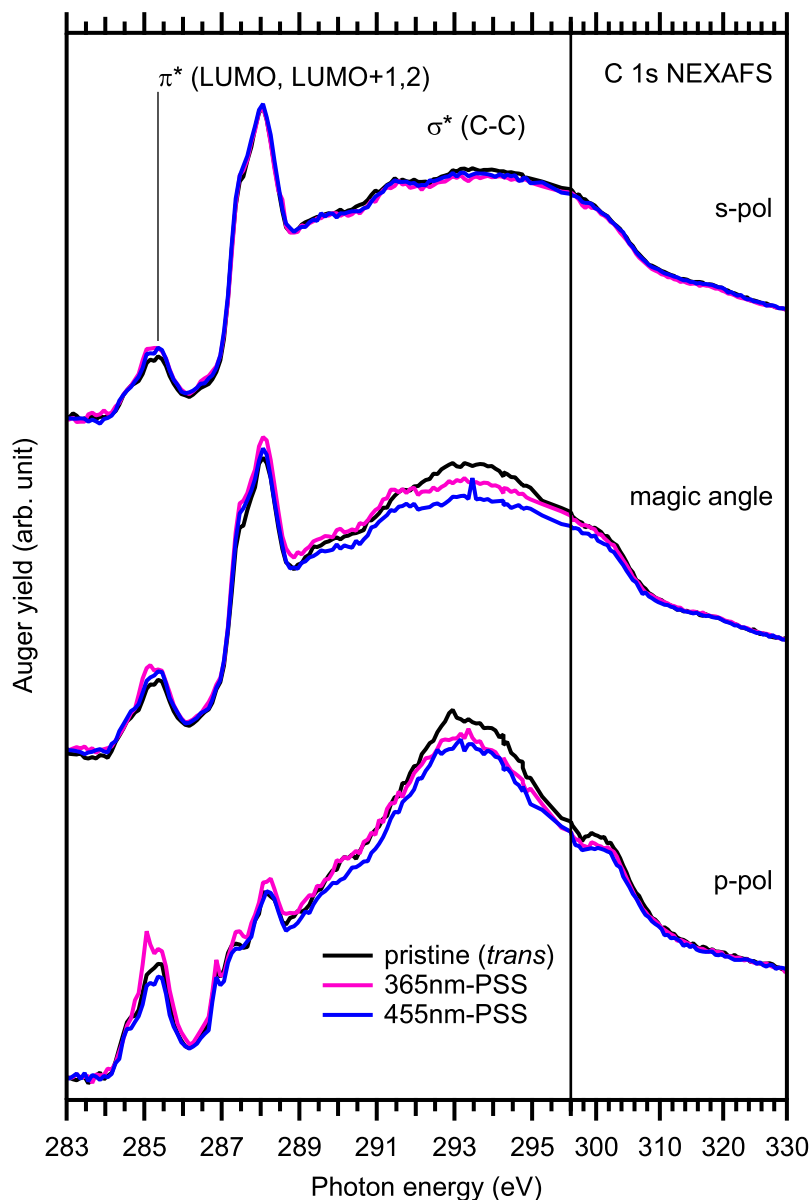
Figure B.2: C 1s NEXAFS spectra of the pristine state and of the PSSs for illumination with light of 365 and 455 nm, measured with different X-ray polarizations.

leaves the question why the LUMO+1 and LUMO+2 levels would be similar in the *trans* and *cis* isomers. This can be explained when looking at the isodensity contours of the LUMO and higher-lying orbitals of the chromophore:[1] In the case of the LUMO orbital there is significant probability density at the N=N bond of the chromophore, whereas the higher orbitals (LUMO+1 to LUMO+3) have little probability density at the N=N bond. Since by isomerization the molecular structure is changed predominantly at the N=N bridge, we expect a significant change in energetic position of the LUMO, but not the higher orbitals.

---

[1] [86, Fig. 9] shows the isodensity contours of CF_3-Az6, which is different from Az11 only by a shorter alkyl chain and a CF_3 head group, neither should significantly change the orbitals.
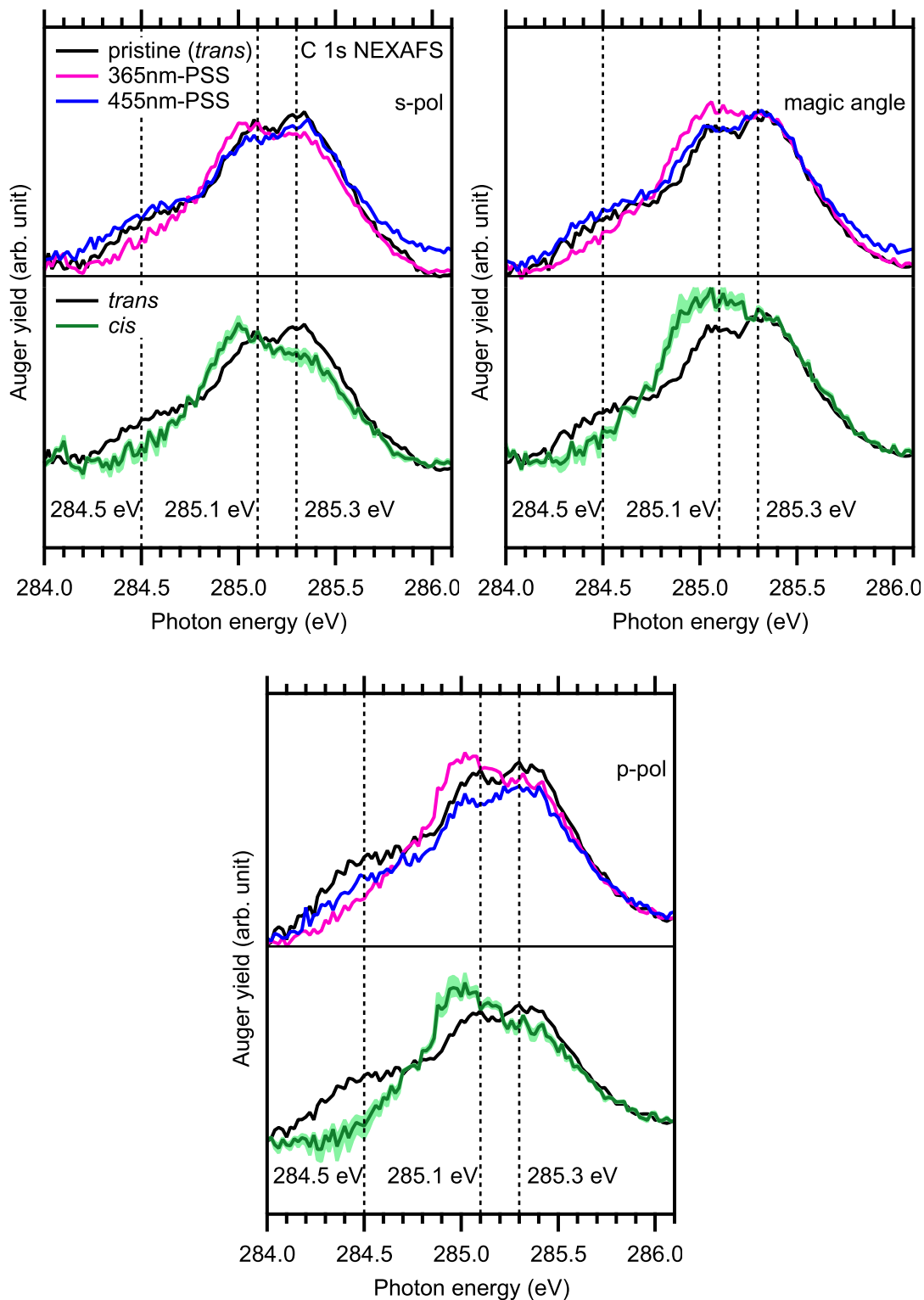
Figure B.3: High-resolution NEXAFS spectra of the C 1s→$\pi^\star$ excitation for measured in different X-ray polarizations. Top of every panel: pristine (pure *trans*) state and PSSs for illumination with light of 365 and 455 nm. Bottom of every panel: reconstructed *cis* spectrum. The range of uncertainty corresponds to the upper and lower limit of the amount of *cis* molecules in the 365 nm-PSS (cf. Sec. 7.2.1.1). The *trans* spectrum is shown for comparison.

B.1.3 N 1s NEXAFS Kinetics
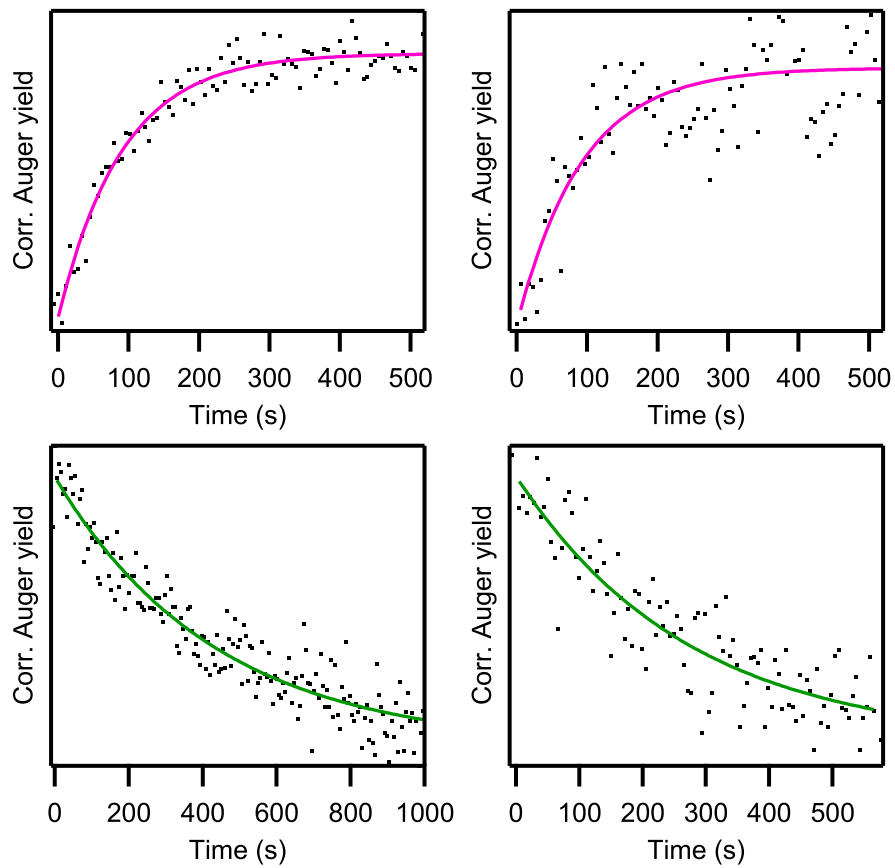
Figure B.4: Additional kinetic curves recorded at the N 1s edge ($h\nu = 399.1\,\text{eV}$) at a temperature of $110\,\text{K}$, evaluated for the results given in Tab. 7.3. Top: Photo-isomerization with light of $365\,\text{nm}$. Bottom: Thermal isomerization.

B.2   DR Spectroscopy

B.2.1   Modeling of Spectra

Table B.3: Fit results from the DR spectra of Az11 SAMs (Figs. 6.4 and 6.5). All parameters in eV. Values with no error were fixed. Film thickness 2 nm, $\epsilon_{\text{const}} = 1.3$.

	100 % Az11 SAM				56 % Az11 SAM	
	p-pol		s-pol		p-pol	
	Value	Error	Value	Error	Value	Error
$h\nu_0$	2.6	-	2.6	-	2.6	-
f_0	0.228	0.009	0.25	0.02	0.147	0.008
γ_0	0.5	-	0.5	-	0.5	-
$h\nu_1$	3.596	0.005	3.552	0.008	3.552	0.006
f_1	0.62	0.04	0.21	0.04	0.44	0.04
γ_1	0.61	0.03	0.30	0.04	0.43	0.03
$h\nu_2$	4.292	0.002	4.109	0.006	4.014	0.004
f_2	3.22	0.04	2.8	0.2	2.08	0.05
γ_2	0.609	0.006	0.95	0.05	0.64	0.02
$h\nu_3$	4.848	0.007	4.848	0.007	5.214	0.006
f_3	0.5	0.1	0.16	0.09	3.7	0.1
γ_3	0.26	0.02	0.17	0.05	1.11	0.03
$h\nu_4$	5.012	0.007	5.00	0.02	-	-
f_4	0.6	0.2	1.03	0.3	-	-
γ_4	0.28	0.05	0.38	0.05	-	-
$h\nu_5$	5.22	0.01	5.24	0.02	-	-
f_5	2.29	0.01	1.9	0.2	-	-
γ_5	0.5	-	0.5	-	-	-
$h\nu_6$	5.49	0.02	5.50	0.02	-	-
f_6	1.09	0.05	1.01	0.07	-	-
γ_6	0.5	-	0.5	-	-	-
$h\nu_7$	6	-	6	-	6	-
f_7	10.62	0.08	12.2	0.2	6.73	0.07
γ_7	0.7	-	0.7	-	0.7	-
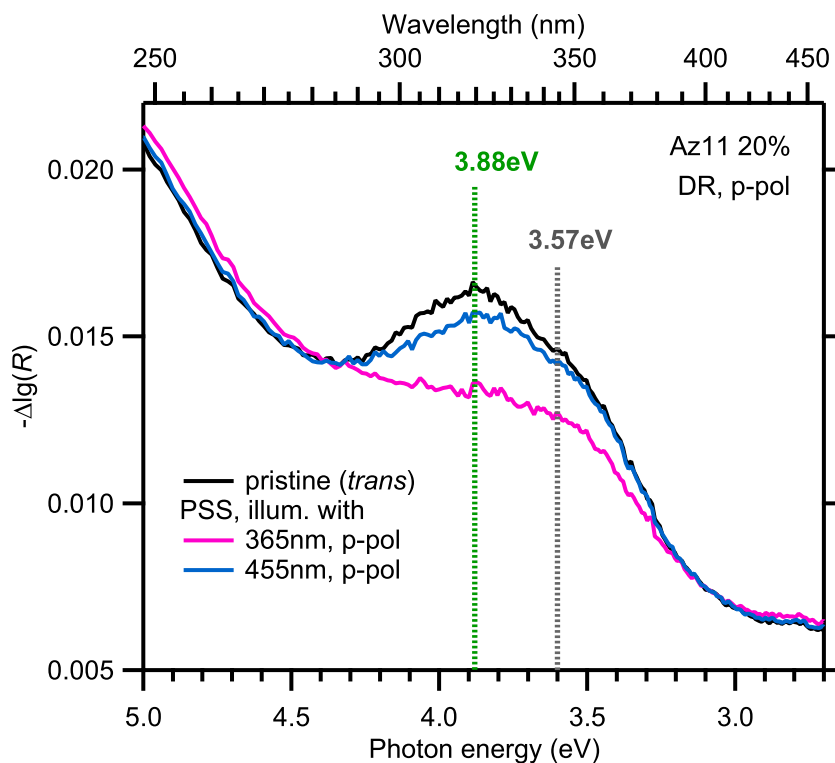
Figure B.5: DR spectra of a $\Theta = 20\,\%$ SAM measured with p-polarized light. The pristine state, the 365 nm-PSS, and the 455 nm-PSS are shown. The vertical lines denote the photon energies at which the isomerization kinetics were recorded (see Fig. B.6).

B.2.2 Isomerization Kinetics

Photoisomerization on a SAM with 20 % Az11 Coverage Fig. B.5 shows DR spectra of a SAM with $\Theta(\mathrm{Az11}) = 20\,\%$ in the pristine state and the PSSs for illumination with light of 365 and 455 nm. The photoisomerization and thermal isomerization kinetics were recorded at two photon energies in the spectral region of the S_2 band: at 3.57 eV (347 nm), the spectral region associated with disordered *trans* isomers, and at 3.88 eV (320 nm), associated with ordered *trans* isomers. The results are shown in Fig. B.6. The difference in time constants is much smaller than for the $\Theta(\mathrm{Az11}) = 80\,\%$ SAM (Fig. 7.13). This is expected since the order is generally weaker in a 20 %-Az11-SAM than in a 80 %-Az11-SAM.

Fig. B.7a shows DR spectra of a SAM with $\Theta(\mathrm{Az11}) = 20\,\%$ in the pristine state and the 310 nm-PSS in comparison with the 365 nm- and 455 nm-PSSs. The 310 nm-PSS lies in between the 365 nm- and 455 nm-PSSs. This can also be seen from the isomerization kinetics (Fig. B.7b).
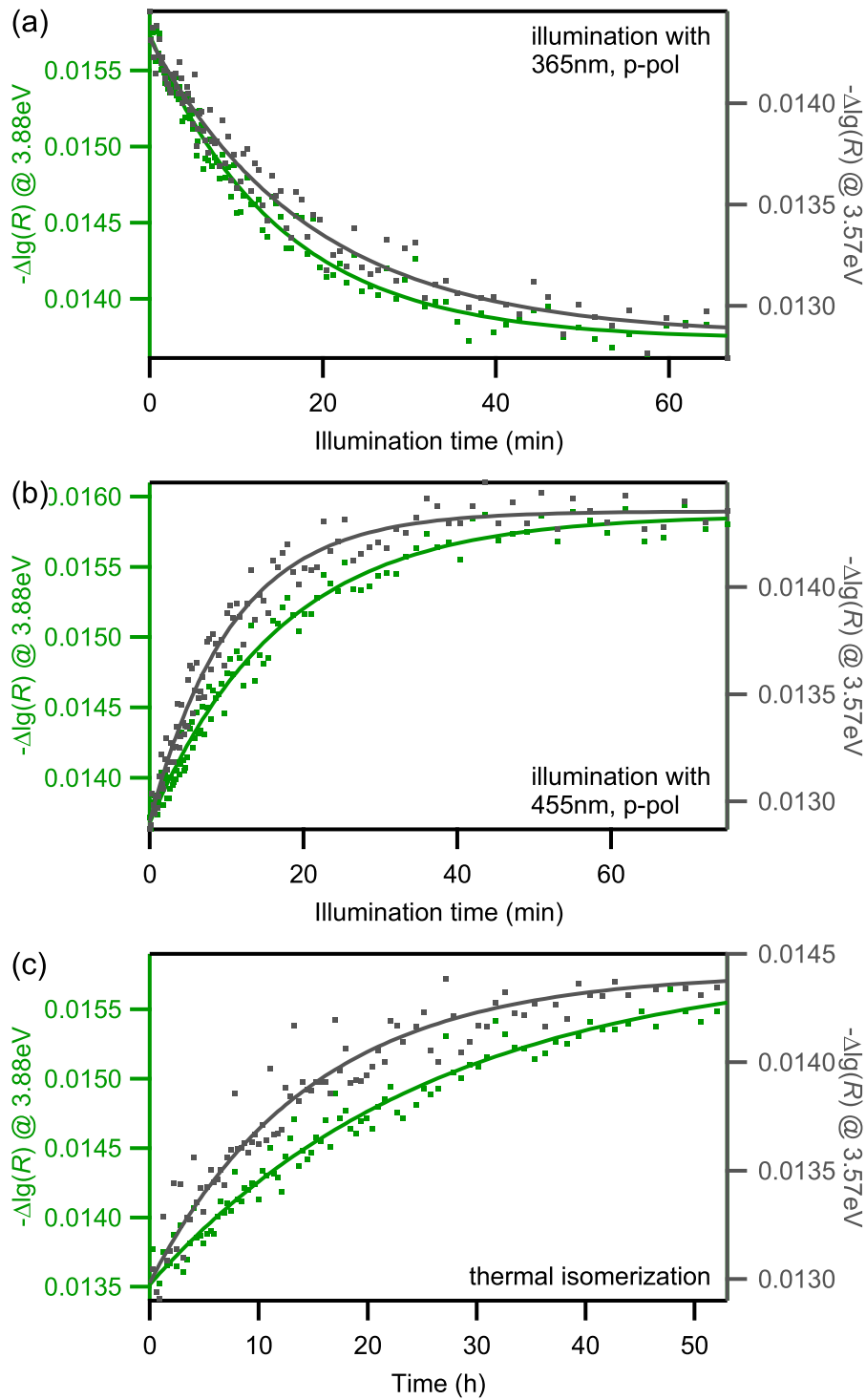
Figure B.6: Isomerization kinetics of a SAM with $\Theta(\text{Az}11) = 20\%$ probed with p-polarized light of 320 nm (3.88 eV, maximum of the S_2 band, *left axis*) and 347 nm (3.57 eV, low-energy shoulder of the S_2 band, *right axis*). The corresponding spectra are shown in Fig. 7.12. (a) Illumination with 365 nm, p-pol, starting from the 455 nm-PSS. (b) Illumination with 455 nm, p-pol, starting from the 365 nm-PSS. (c) Thermal isomerization, starting from the 365 nm-PSS again.
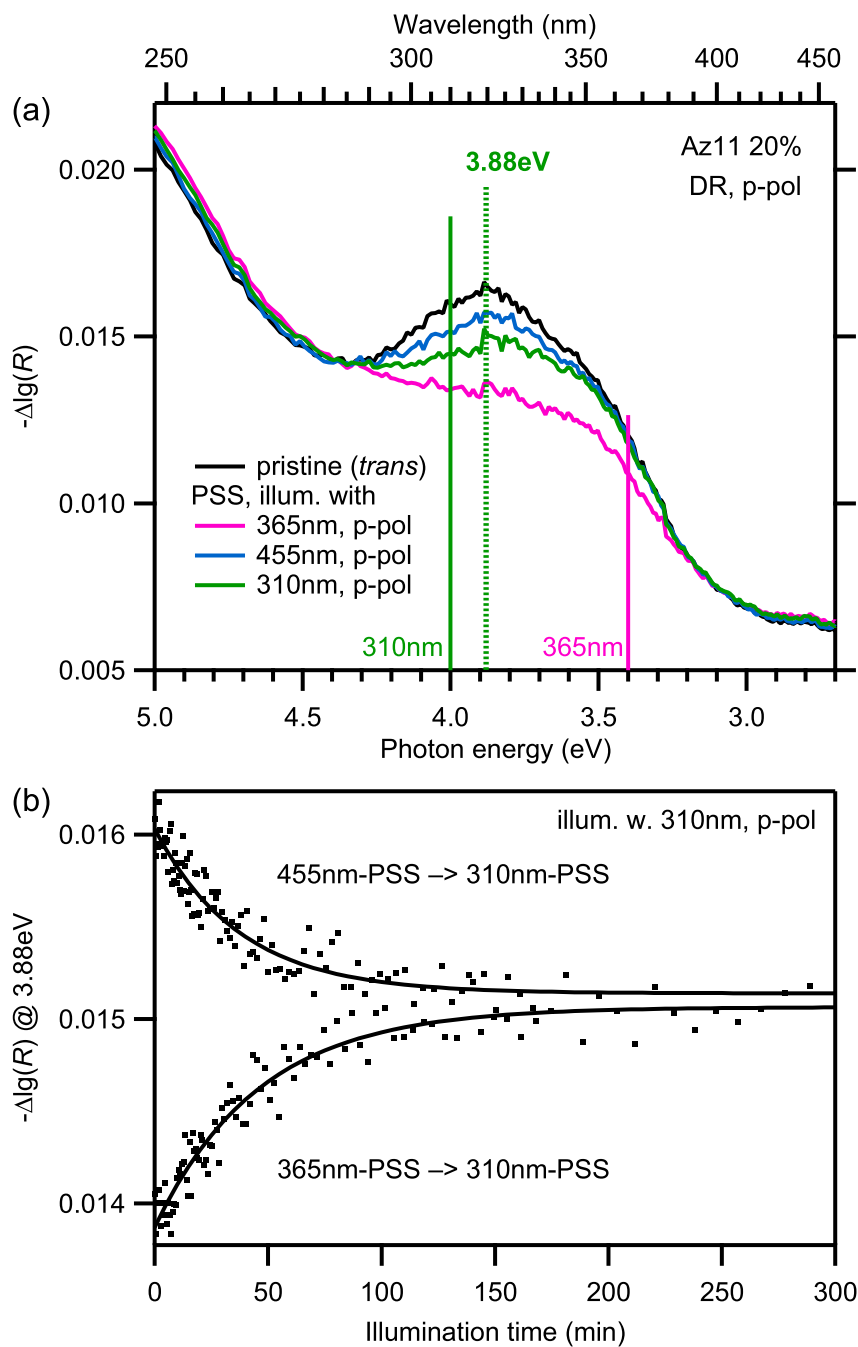
Figure B.7: Photoisomerization experiment with p-polarized light of $\lambda_{\text{exc}} = 310\,\text{nm}$ on a $\Theta = 20\,\%$ SAM. (a) DR Spectra. The $310\,\text{nm}$-PSS lies in between the $455\,\text{nm}$- and $365\,\text{nm}$-PSSs. (a) Isomerization kinetics, starting from the $455\,\text{nm}$-PSS and the $365\,\text{nm}$-PSS.

Tables   The Tables B.4 and B.5 show time constants of thermal isomerization and photoisomerization obtained in DR experiments on SAMs with 80 % and 20 % Az11 coverage Θ, respectively. The isomerization kinetics were recorded with p-polarized light (thereby being able to probe the H-aggregate). Tab. B.6 shows the effective photoisomerization cross-sections obtained from these measurements. The effective isomerization cross-sections determined in NEXAFS (Sec. 7.2.1) and from absorbance spectroscopy of Az11 in solution (Sec. 7.1.1) were added for comparison.

Table B.4: Time constants τ^{th} of thermal isomerization in Az11 SAMs, examined by DR spectroscopy of p-polarized light.

Sample		τ^{th} (h)		
	$\lambda_{\mathrm{pr}} =$	299 nm (4.15 eV)	320 nm (3.88 eV)	347 nm (3.57 eV)
80 % Az11 SAM		23 ± 2		5 ± 1
20 % Az11 SAM			26 ± 3	15 ± 2

Table B.5: Photoisomerization in Az11 SAMs examined by DR spectroscopy of p-polarized light: Time constants τ^{ph} of photoisomerization triggered by light of wavelength λ_{exc} in s- or p-polarization and with intensity I_{ph}.

Illumination with		Initial	τ^{ph} (s)			
λ_{exc}, pol.	I_{ph} (mW cm^{-2})	condition	80 % Az11 SAM		20 % Az11 SAM	
		$\lambda_{\mathrm{pr}} =$	299 nm (4.15 eV)	347 nm (3.57 eV)	320 nm (3.88 eV)	347 nm (3.57 eV)
365 nm, p	0.32 ± 0.02	455 nm-PSS	1400 ± 50	2300 ± 400	860 ± 30	1100 ± 50
s	0.33 ± 0.02		540 ± 40	500 ± 100	240 ± 20	280 ± 30
455 nm, p	0.328 ± 0.009	365 nm-PSS	1600 ± 100	450 ± 50	1050 ± 40	650 ± 30
s	0.331 ± 0.009		680 ± 20	210 ± 30	330 ± 20	210 ± 10
310 nm, p	0.036 ± 0.003	455 nm-PSS	2700 ± 200	— [a]	2300 ± 100	3400 ± 600
s	0.044 ± 0.004		720 ± 30	— [a]	430 ± 40	440 ± 40
310 nm, p	0.036 ± 0.003	365 nm-PSS	3700 ± 200	1500 ± 300	2700 ± 200	1700 ± 200
s	0.044 ± 0.004		930 ± 30	400 ± 40	540 ± 40	400 ± 30

[a] No signal change observed

Table B.6: Effective[a] photoisomerization cross-sections, in $10^{-17}\,\mathrm{cm}^2$.

λ_{exc}, pol.	Initial condition	SAM (80 %) DR, p-pol		SAM (20 %) DR, p-pol		SAM (20 %) NEXAFS[c]	Az11 (sol.) UV/vis[c]
	$\lambda_{\mathrm{pr}} =$	299 nm (4.15 eV)	347 nm (3.57 eV)	320 nm (3.88 eV)	347 nm (3.57 eV)		
365 nm, p	455 nm-PSS	0.121 ± 0.007	0.07 ± 0.02	0.20 ± 0.02	0.15 ± 0.01	0.11 ± 0.02	2.7 ± 0.2
s		0.30 ± 0.03	0.32 ± 0.07	0.68 ± 0.07	0.58 ± 0.07		
455 nm, p	365 nm-PSS	0.082 ± 0.006	0.29 ± 0.04	0.125 ± 0.006	0.20 ± 0.02	0.10 ± 0.03	0.7 ± 0.03
s		0.192 ± 0.008	0.6 ± 0.1	0.40 ± 0.03	0.63 ± 0.04		
310 nm, p	455 nm-PSS	0.64 ± 0.08	— [b]	0.76 ± 0.09	0.5 ± 0.2		
s		2.0 ± 0.3	— [b]	3.3 ± 0.5	3.3 ± 0.5	—	3.7 ± 0.3
310 nm, p	365 nm-PSS	0.46 ± 0.06	1.1 ± 0.3	0.64 ± 0.08	1.0 ± 0.2		
s		1.5 ± 0.2	3.5 ± 0.5	2.7 ± 0.4	3.6 ± 0.5		

[a] In the case of the measurements on SAMs the values were corrected for the thermal isomerization, in the case of Az11 in methanol the thermal isomerization can be neglected.

[b] No signal change observed

[c] Illuminated with unpolarized light
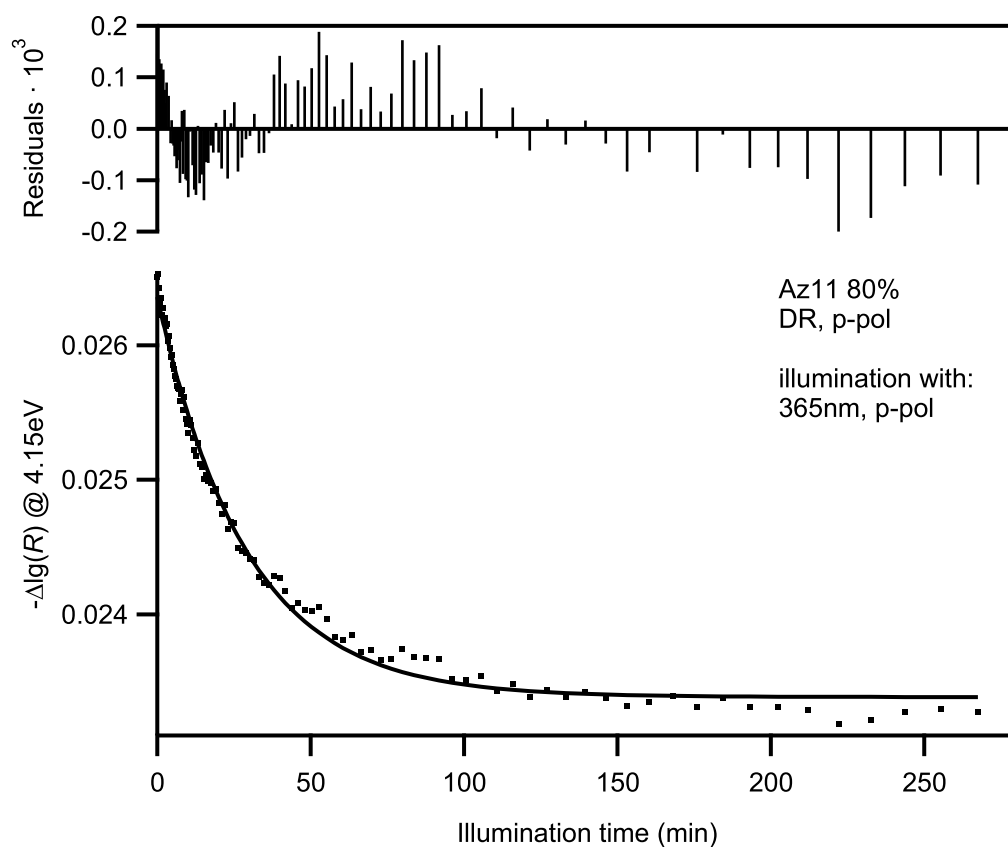
Figure B.8: If the photoisomerization kinetics is recorded long enough, slight deviations from first order kinetics are observed.

Bibliography

[1]   H. H. Radamson, X. He, Q. Zhang, J. Liu, H. Cui, J. Xiang, Z. Kong, W. Xiong, J. Li, J. Gao, H. Yang, S. Gu, X. Zhao, Y. Du, J. Yu, and G. Wang. "Miniaturization of CMOS." *Micromachines* **10** (2019), 293. DOI: `10.3390/mi10050293` (cit. on p. 9)

[2]   T. Tamaki and T. Ogawa. "Nonlinear and Nonsymmetric Single-Molecule Electronic Properties Towards Molecular Information Processing." *Top. Curr. Chem.* **375** (2017). DOI: `10.1007/s41061-017-0167-y` (cit. on p. 9)

[3]   K. Ichimura, S.-K. Oh, and M. Nakagawa. "Light-Driven Motion of Liquids on a Photoresponsive Surface." *Science* **288** (2000), 1624–1626. DOI: `10.1126/science.288.5471.1624` (cit. on p. 9)

[4]   J. García-Amorós and D. Velasco. "Recent Advances Towards Azobenzene-Based Light-Driven Real-Time Information-Transmitting Materials." *Beilstein J. Org. Chem.* **8** (2012), 1003–1017. DOI: `10.3762/bjoc.8.113` (cit. on pp. 9–10, 13)

[5]   J. M. Abendroth, O. S. Bushuyev, P. S. Weiss, and C. J. Barrett. "Controlling Motion at the Nanoscale: Rise of the Molecular Machines." *ACS Nano* **9** (2015). PMID: 26172380, 7746–7768. DOI: `10.1021/acsnano.5b03367` (cit. on p. 9)

[6]   L. Grill. "Functionalized Molecules Studied by STM: Motion, Switching and Reactivity." *J. Phys.: Condens. Matter* **20** (2008), 053001 (19pp). DOI: `10.1088/0953-8984/20/05/053001` (cit. on p. 9)

[7]   N. Katsonis, M. Lubomska, M. M. Pollard, B. L. Feringa, and P. Rudolf. "Synthetic Light-Activated Molecular Switches and Motors on Surfaces." *Prog. Surf. Sci.* **82** (2007), 407–434. DOI: `10.1016/j.progsurf.2007.03.011` (cit. on pp. 9, 13)

[8]   V. Kriegisch and C. Lambert. "Self-Assembled Monolayers of Chromophores on Gold Surfaces." *Top. Curr. Chem.* **258** (2005), 257–313. DOI: `10.1007/b135682` (cit. on p. 10)

[9]   H. M. D. Bandara and S. C. Burdette. "Photoisomerization in Different Classes of Azobenzene." *Chem. Soc. Rev.* **41** (2012), 1809–1825. DOI: `10.1039/C1CS15179G` (cit. on pp. 10, 15–16, 81–82)

[10] R. Klajn. "Immobilized Azobenzenes for the Construction of Photoresponsive Materials." *Pure Appl. Chem.* **82** (2010), 2247–2279. DOI: `10.1351/PAC-CON-10-09-04` (cit. on pp. 10–11, 22)

[11] M. J. Comstock, N. Levy, A. Kirakosian, J. Cho, F. Lauterwasser, J. H. Harvey, D. A. Strubbe, J. M. J. Fréchet, D. Trauner, S. G. Louie, and M. F. Crommie. "Reversible Photomechanical Switching of Individual Engineered Molecules at a Metallic Surface." *Phys. Rev. Lett.* **99**, 038301 (2007), 038301. DOI: `10.1103/PhysRevLett.99.038301` (cit. on pp. 10, 22)

[12] R. J. Maurer and K. Reuter. "Computational Design of Metal-Supported Molecular Switches: Transient Ion Formation During Light- and Electron-Induced Isomerisation of Azobenzene." *J. Phys.: Condens. Matter* **31** (2018), 044003. DOI: `10.1088/1361-648x/aaf0e1` (cit. on pp. 10, 22)

[13] S. Hagen, P. Kate, M. V. Peters, S. Hecht, M. Wolf, and P. Tegeder. "Kinetic Analysis of the Photochemically and Thermally Induced Isomerization of an Azobenzene Derivative on Au(111) Probed by Two-Photon Photoemission." *Appl. Phys. A* **93** (2008), 253–260. DOI: `10.1007/s00339-008-4831-5` (cit. on p. 10)

[14] A. Ulman. "Formation and Structure of Self-Assembled Monolayers." *Chem. Rev.* **96** (1996), 1533–1554. DOI: `10.1021/cr9502357` (cit. on pp. 10, 13, 20–21)

[15] C. Vericat, M. E. Vela, G. Benitez, P. Carro, and R. C. Salvarezza. "Self-Assembled Monolayers of Thiols and Dithiols on Gold: New Challenges for a Well-Known System." *Chem. Soc. Rev.* **39** (2010), 1805–1834. DOI: `10.1039/b907301a` (cit. on pp. 10, 20–21)

[16] G. Pace, V. Ferri, C. Grave, M. Elbing, C. von Hänisch, M. Zharnikov, M. Mayor, M. A. Rampi, and P. Samorì. "Cooperative Light-Induced Molecular Movements of Highly Ordered Azobenzene Self-Assembled Monolayers." *Proc. Natl. Acad. Sci. U. S. A.* **104** (2007), 9937–9942. DOI: `10.1073/pnas.0703748104` (cit. on p. 10)

[17] M. Elbing, A. Blaszczyk, C. von Hänisch, M. Mayor, V. Ferri, C. Grave, M. A. Rampi, G. Pace, P. Samorì, A. Shaporenko, and M. Zharnikov. "Single Component Self-Assembled Monolayers of Aromatic Azo-Biphenyl: Influence of the Packing Tightness on the SAM Structure and Light-Induced Molecular Movements." *Adv. Funct. Mater.* **18** (2008), 2972–2983. DOI: `10.1002/adfm.200800652` (cit. on p. 10)

[18] C. Gahl, R. Schmidt, D. Brete, E. R. McNellis, W. Freyer, R. Carley, K. Reuter, and M. Weinelt. "Structure and Excitonic Coupling in Self-Assembled Monolayers of Azobenzene-Functionalized Alkanethiols." *J. Am. Chem. Soc.* **132** (2010), 1831–1838. DOI: `10.1021/ja903636q` (cit. on pp. 10–11, 22, 59, 61, 66, 69)

[19] N. Heinemann, J. Grunau, T. Leißner, O. Andreyev, S. Kuhn, U. Jung, D. Zargarani, R. Herges, O. Magnussen, and M. Bauer. "Reversible Switching in Self-Assembled Monolayers of Azobenzene Thiolates on Au (111) Probed by Threshold Photoemission." *Chem. Phys.* **402** (2012), 22–28. DOI: `10.1016/j.chemphys.2012.03.025` (cit. on pp. 10, 22)

[20] T. Nagahiro, H. Akiyama, M. Hara, and K. Tamada. "Photoisomerization of Azobenzene Containing Self-Assembled Monolayers Investigated by Kelvin Probe Work Function Measurements." *J. Electron Spectrosc. Relat. Phenom.* **172** (2009), 128–133. DOI: `10.1016/j.elspec.2009.02.009` (cit. on pp. 11, 22)

[21] B. Stiller, P. Karageorgiev, T. Jüngling, D. Prescher, T. Zetzsche, R. Dietel, G. Knochenhauer, and L. Brehmer. "Optically Induced Switching of Azobenzene Containing Self Assembling Monolayers Investigated by Kelvin Probe and Scanning Force Microscopy." *Mol. Cryst. Liq. Cryst.* **355** (2001), 401–411. DOI: `10.1080/10587250108023673` (cit. on pp. 11, 22)

[22] U. Jung, O. Filinova, S. Kuhn, D. Zargarani, C. Bornholdt, R. Herges, and O. Magnussen. "Photoswitching Behavior of Azobenzene-Containing Alkanethiol Self-Assembled Monolayers on Au Surfaces." *Langmuir* **26** (2010), 13913–13923. DOI: `10.1021/la1015109` (cit. on pp. 11, 22, 89–90)

[23] D. T. Valley, M. Onstott, S. Malyk, and A. V. Benderskii. "Steric Hindrance of Photoswitching in Self-Assembled Monolayers of Azobenzene and Alkane Thiols." *Langmuir* **29** (2013), 11623–11631. DOI: `10.1021/la402144g` (cit. on pp. 11, 22, 89, 92)

[24] B. K. Pathem, S. A. Claridge, Y. B. Zheng, and P. S. Weiss. "Molecular Switches and Motors on Surfaces." *Annu. Rev. Phys. Chem.* **64** (2013), 605–630. DOI: `10.1146/annurev-physchem-040412-110045` (cit. on p. 13)

[25] H. Fliegl, A. Köhn, C. Hättig, and R. Ahlrichs. "Ab Initio Calculation of the Vibrational and Electronic Spectra of *trans*- and *cis*-Azobenzene." *J. Am. Chem. Soc.* **125** (2003), 9821–9827. DOI: `10.1021/ja034433o` (cit. on p. 14)

[26] J. Griffiths. "Photochemistry of Azobenzene and its Derivatives." *Chem. Soc. Rev.* **1** (1972), 481–493. DOI: `10.1039/CS9720100481` (cit. on p. 14)

[27] I. Conti, M. Garavelli, and G. Orlandi. "The Different Photoisomerization Efficiency of Azobenzene in the Lowest nπ^* and $\pi\pi^*$ Singlets: The Role of a Phantom State." *J. Am. Chem. Soc.* **130** (2008), 5216–5230. DOI: `10.1021/ja710275e` (cit. on pp. 14, 16, 81–83)

[28] H. Rau. "Azo Compounds." In: *Photochromism*. Ed. by H. Dürr and H. Bouas-Laurent. Amsterdam: Elsevier Science, 2003. Chap. 4, 165–192. ISBN: 978-0-444-51322-9. DOI: `10.1016/B978-044451322-9/50008-7` (cit. on p. 14)

[29] D. Brete. "Azobenzenes and Imines as Molecular Switches on Gold(111): Structure, Excitonic Coupling, and Photoisomerization." PhD thesis. Fachbereich Physik der Freien Universität Berlin, 2016 (cit. on pp. 15, 36, 41–42, 44, 54)

[30] T. Nägele, R. Hoche, W. Zinth, and J. Wachtveitl. "Femtosecond Photoisomerization of cis-Azobenzene." *Chem. Phys. Lett.* **272** (1997), 489–495. DOI: `10.1016/S0009-2614(97)00531-9` (cit. on p. 17)

[31]   G. S. Hartley. "The *cis*-Form of Azobenzene and the Velocity of the Thermal *cis–trans*-Conversion of Azobenzene and some Derivatives." *J. Chem. Soc.* (1938), 633–642. DOI: 10.1039/JR9380000633 (cit. on pp. 16, 79)

[32]   R. J. W. Le Fèvre and J. Northcott. "The Effects of Substituents and Solvents on the *cis–trans* Change of Azobenzene." *J. Chem. Soc.* (1953), 867–870. DOI: 10.1039/JR9530000867 (cit. on pp. 16, 79, 88)

[33]   J. C. Love, L. A. Estroff, J. K. Kriebel, R. G. Nuzzo, and G. M. White-sides. "Self-Assembled Monolayers of Thiolates on Metals as a Form of Nanotechnology." *Chem. Rev.* **105** (2005), 1103–1169. DOI: 10.1021/cr0300789 (cit. on pp. 20–21)

[34]   L. H. Dubois and R. G. Nuzzo. "Synthesis, Structure and Properties of Model Organic Surfaces." *Annu. Rev. Phys. Chem.* **43** (1992), 437–463. DOI: 10.1146/annurev.pc.43.100192.002253 (cit. on p. 21)

[35]   S. Narasimhan and D. Vanderbilt. "Elastic Stress Domains and the Herringbone Reconstruction on Au(111)." *Phys. Rev. Lett.* **69** (1992), 1564–1567. DOI: 10.1103/PhysRevLett.69.1564 (cit. on p. 21)

[36]   F. Reinert and G. Nicolay. "Influence of the Herringbone Reconstruction on the Surface Electronic Structure of Au(111)." *Appl. Phys. A* **78** (2004), 817–821. DOI: 10.1007/s00339-003-2436-6 (cit. on p. 21)

[37]   W. Freyer, D. Brete, R. Schmidt, C. Gahl, R. Carley, and M. Weinelt. "Switching Behavior and Optical Absorbance of Azobenzene-Functionalized Alkanethiols in Different Environments." *J. Photochem. Photobiol., A* **204** (2009), 102–109. DOI: 10.1016/j.jphotochem.2009.02.018 (cit. on p. 22)

[38]   H. Wolf, H. Ringsdorf, E. Delamarche, T. Takami, H. Kang, B. Michel, C. Gerber, M. Jaschke, H.-J. Butt, and E. Bamberg. "End-Group-Dominated Molecular Order in Self-Assembled Monolayers." *J. Phys. Chem.* **99** (1995), 7102–7107. DOI: 10.1021/j100018a050 (cit. on pp. 22–23, 70)

[39]   M. Jaschke, H. Schönherr, H. Wolf, H.-J. Butt, E. Bamberg, M. K. Be-socke, and H. Ringsdorf. "Structure of Alkyl and Perfluoroalkyl Disul-fide and Azobenzenethiol Monolayers on Gold(111) Revealed by Atomic Force Microscopy." *J. Phys. Chem.* **100** (1996), 2290–2301. DOI: 10.1021/jp952355o (cit. on pp. 22–23, 70, 72, 94)

[40]   E. Titov, G. Granucci, J. P. Götze, M. Persico, and P. Saalfrank. "Dy-namics of Azobenzene Dimer Photoisomerization: Electronic and Steric Effects." *J. Phys. Chem. Lett.* **7** (2016), 3591–3596. DOI: 10.1021/acs.jpclett.6b01401 (cit. on p. 22)

[41]   M. J. Cook, A.-M. Nygard, Z. Wang, and D. A. Russel. "An Evanescent Field Driven Mono-Molecular Layer Photoswitch: Coordination and Re-lease of Metallated Macrocycles." *Chem. Commun.* (2002), 1056–1057. DOI: 10.1039/B201870P (cit. on p. 22)

[42] H. Akiyama, K. Tamada, J. Nagasawa, K. Abe, and T. Tamki. "Photoreactivity in Self-Assembled Monolayers Formed from Asymmetric Disulfides Having *para*-Substituted Azobenzenes." *J. Phys. Chem. B* **107** (2003), 130–135. DOI: 10.1021/jp026103g (cit. on p. 22)

[43] A. S. Kumar, T. Ye, T. Takami, B.-C. Yu, A. K. Flatt, J. M. Tour, and P. S. Weiss. "Reversible Photo-Switching of Single Azobenzene Molecules in Controlled Nanoscale Environments." *Nano Lett.* **8** (2008), 1644–1648. DOI: 10.1021/nl080323%2B (cit. on p. 22)

[44] Y. B. Zheng, J. L. Payton, C.-H. Chung, R. Liu, S. Cheunkar, B. K. Pathem, Y. Yang, L. Jensen, and P. S. Weiss. "Surface-Enhanced Raman Spectroscopy to Probe Reversibly Photoswitchable Azobenzene in Controlled Nanoscale Environments." *Nano Lett.* **11** (2011), 3447–3452. DOI: 10.1021/nl2019195 (cit. on p. 22)

[45] S. Imabayashi, N. Gon, T. Sasaki, D. Hobara, and T. Kakiuchi. "Effect of Nanometer-Scale Phase Separation on Wetting of Binary Self-Assembled Thiol Monolayers on Au(111)." *Langmuir* **14** (1998), 2348–2351. DOI: 10.1021/la971377u (cit. on p. 22)

[46] G. Pace, A. Petitjean, M.-N. Lalloz-Vogel, J. Harrowfield, J.-M. Lehn, and P. Samorì. "Subnanometer-Resolved Patterning of Bicomponent Self-Assembled Monolayers on Au(111)." *Angew. Chem., Int. Ed.* **47** (2008), 2484–2488. DOI: 10.1002/anie.200704731 (cit. on p. 22)

[47] S. Chen, L. Li, C. L. Boozer, and S. Jiang. "Controlled Chemical and Structural Properties of Mixed Self-Assembled Monolayers by Coadsorption of Symmetric and Asymmetric Disulfides on Au(111)." *J. Phys. Chem. B* **105** (2001), 2975–2980. DOI: 10.1021/jp0040650 (cit. on p. 22)

[48] T. Moldt, D. Brete, D. Przyrembel, S. Das, J. R. Goldman, P. K. Kundu, C. Gahl, R. Klajn, and M. Weinelt. "Tailoring the Properties of Surface-Immobilized Azobenzenes by Monolayer Dilution and Surface Curvature." *Langmuir* **31** (2015), 1048–1057. DOI: 10.1021/la504291n (cit. on pp. 22, 57, 60–62, 106)

[49] W. B. Caldwell, D. J. Campbell, K. Chen, B. R. Herr, C. A. Mirkin, A. Malik, M. K. Durbin, P. Dutta, and K. G. Huang. "A Highly Ordered Self-Assembled Monolayer Film of an Azobenzenealkanethiol on Au(111): Electrochemical Properties and Structural Characterization by Synchrotron In-Plane X-ray Diffraction, Atomic Force Microscopy, and Surface-Enhanced Raman Spectroscopy." *J. Am. Chem. Soc.* **117** (1995), 6071–6082. DOI: 10.1021/ja00127a021 (cit. on p. 23)

[50] H. Ibach and H. Lüth. *Festkörperphysik*. 7th ed. Springer Berlin Heidelberg, 2008. ISBN: 978-3-540-85794-5 (cit. on p. 24)

[51] A. S. Davydov. *Theory of Molecular Excitons*. Plenum Press, New York - London, 1971 (cit. on pp. 24, 28)

[52] M. Kasha. "Classification of Excitons." In: *Physical Processes in Radiation Biology*. Ed. by L. Augstein, R. Mason, and B. Rosenberg. 1964, 17–19. DOI: 10.1016/B978-1-4831-9824-8.50006-2 (cit. on p. 24)

[53] T. Förster. "Zwischenmolekulare Energiewanderung und Fluoreszenz."
      Ann. Phys. (Berlin, Ger.) **437** (1948), 55–75. DOI: `10.1002/andp.`
      `19484370105` (cit. on p. 24)

[54] M. Kasha. "Energy Transfer Mechanisms and the Molecular Exciton
      Model for Molecular Aggregates." English. *Radiat. Res.* **20** (1963), 55–
      70. DOI: `10.2307/3571331` (cit. on pp. 24–28)

[55] E. G. McRae and M. Kasha. "The Molecular Exciton Model." In: *Phys-
      ical Processes in Radiation Biology.* Ed. by L. Augstein, R. Mason,
      and B. Rosenberg. 1964, 23–42. DOI: `10.1016/B978-1-4831-9824-`
      `8.50007-4` (cit. on pp. 27, 67)

[56] W. T. Simpson and D. L. Peterson. "Coupling Strength for Resonance
      Force Transfer of Electronic Energy in Van der Waals Solids." *J. Chem.
      Phys.* **26** (1957), 588–593. DOI: `10.1063/1.1743351` (cit. on p. 27)

[57] M. Born and E. Wolf. *Principles of Optics.* 4th ed. Pergamon Press,
      1970 (cit. on pp. 28, 30, 32)

[58] H. Mayer. *Physik dünner Schichten.* Vol. 1. Wissenschaftliche Verlags-
      gesellschaft, 1950 (cit. on pp. 28, 31)

[59] T. Wakamatsu, S. Toyoshima, and K. Saito. "Optical Reflection Re-
      sponse of Dye-Aggregate Films in the Absorption Bands." *J. Opt. Soc.
      Am. B* **23** (2006), 1859–1866. DOI: `10.1364/JOSAB.23.001859` (cit. on
      pp. 30, 33)

[60] E. Hecht. *Optics.* Ed. by A. Black. 4th ed. Pearson Education, 2002.
      ISBN: 0-321-18878-0 (cit. on p. 31)

[61] R. Forker, M. Gruenewald, and T. Fritz. "Optical Differential Reflectance
      Spectroscopy on Thin Molecular Films." *Annu. Rep. Prog. Chem., Sect.
      C: Phys. Chem.* **108** (2012), 34–68. DOI: `10.1039/C2PC90002E` (cit. on
      pp. 32, 49, 52)

[62] J. D. Jackson. *Classical Electrodynamics.* 3rd ed. John Wiley and Sons
      Ltd, 1998. ISBN: 047130932X (cit. on p. 33)

[63] A. Nilsson. "Applications of Core Level Spectroscopy to Adsorbates."
      J. Electron Spectrosc. Relat. Phenom. **126** (2002), 3–42. DOI: `10.1016/`
      `S0368-2048(02)00141-X` (cit. on p. 35)

[64] M. P. Seah, I. S. Gilmore, and G. Beamson. "XPS: Binding Energy Cal-
      ibration of Electron Spectrometers 5—Re-evaluation of the Reference
      Energies." *Surf. Interface Anal.* **26** (1998), 642–649. DOI: `10.1002/`
      `(SICI)1096-9918(199808)26:9<642::AID-SIA408>3.0.CO;2-3`
      (cit. on pp. 36, 108)

[65] R. Schmidt. "Selbstorganisation und Photoisomerisation von Azoben-
      zolderivaten auf Au(111)-Oberflächen." PhD thesis. Fachbereich Physik
      der Freien Universität Berlin, 2011 (cit. on pp. 36, 40)

[66] D. A. Shirley. "High-Resolution X-ray Photoemission Spectrum of the
      Valence Bands of Gold." *Phys. Rev. B* **5** (1972), 4709–4714. DOI: `10.`
      `1103/PhysRevB.5.4709` (cit. on p. 37)

[67] P. Feulner, T. Niedermayer, K. Eberle, R. Schneider, D. Menzel, A. Baumer, E. Schmich, A. Shaporenko, Y. Tai, and M. Zharnikov. "Strong Temperature Dependence of Irradiation Effects in Organic Layers." *Phys. Rev. Lett.* **93** (2004), 178302. DOI: `10.1103/PhysRevLett.93.178302` (cit. on pp. 38, 59, 116).

[68] A. C. Thompson, D. T. Attwood, E. M. Gullikson, H. M. R., J. B. Kortright, R. A. L., U. J. H., K.-J. Kim, J. Kirz, I. Lindau, P. Pianetta, H. Winick, G. P. Williams, and J. H. Scofield. *X-ray Data Booklet.* Ed. by A. C. Thompson and D. Vaughan. 2nd ed. Lawrence Berkeley National Laboratory, 2001 (cit. on p. 38).

[69] J. Stöhr. *NEXAFS Spectroscopy.* 1st ed. Springer Series in Surface Sciences. Springer, Corrected Printing 1996 (cit. on pp. 38–39, 42).

[70] W. Bronsch. Private communication. Fachbereich Physik, Freie Universität Berlin, Germany (cit. on p. 39).

[71] P. E. Batson. "Carbon 1s Near-Edge-Absorption Fine Structure in Graphite." *Phys. Rev. B* **48** (1993), 2608–2610. DOI: `10.1103/PhysRevB.48.2608` (cit. on p. 42).

[72] C. T. Chen, Y. Ma, and F. Sette. "K-shell Photoabsorption of the N_2 Molecule." *Phys. Rev. A* **40** (1989), 6737–6740. DOI: `10.1103/PhysRevA.40.6737` (cit. on p. 42).

[73] J. Stöhr and D. A. Outka. "Determination of Molecular Orientation on Surfaces from the Angular Dependence of Near-Edge X-ray-Absorption Fine-Structure Spectra." *Phys. Rev. B* **36** (1987), 7891–7905. DOI: `10.1103/PhysRevB.36.7891` (cit. on p. 42).

[74] M. Hesse, H. Meier, and B. Zeeh. "UV/Vis-Spektren." In: *Spektroskopische Methoden in der organischen Chemie.* 6th ed. Thieme; Stuttgart, New York, 2002. Chap. 1, 1–30. ISBN: 3135761061 (cit. on p. 45).

[75] H. Gross, B. Dörband, and H. Müller. "Polarimetry." In: *Handbook of Optical Systems.* Vol. 5. Wiley-VCH Verlag GmbH & Co. KGaA, 2012. Chap. 51, 559–642. ISBN: 9783527699230. DOI: `10.1002/9783527699230.ch6` (cit. on pp. 47–48).

[76] J. D. E. McIntyre and D. E. Aspnes. "Differential Reflection Spectroscopy of Very Thin Surface Films." *Surf. Sci.* **24** (1971), 417–434. DOI: `10.1016/0039-6028(71)90272-X` (cit. on p. 49).

[77] P. B. Johnson and R. W. Christy. "Optical Constants of the Noble Metals." *Phys. Rev. B* **6** (1972), 4370–4379. DOI: `10.1103/PhysRevB.6.4370` (cit. on pp. 52, 69, 111).

[78] K. Heister, M. Zharnikov, M. Grunze, and L. S. O. Johansson. "Adsorption of Alkanethiols and Biphenylthiols on Au and Ag Substrates: A High-Resolution X-ray Photoelectron Spectroscopy Study." *J. Phys. Chem. B* **105** (2001), 4058–4061. DOI: `10.1021/jp010127q` (cit. on p. 54).

[79] G. Liu, J. A. Rodriguez, J. Dvorak, J. Hrbek, and T. Jirsak. "Chemistry of Sulfur-Containing Molecules on Au(1 1 1): Thiophene, Sulfur Dioxide, and Methanethiol Adsorption." *Surf. Sci.* **505** (2002), 295–307. DOI: `10.1016/S0039-6028(02)01377-8` (cit. on p. 55)

[80] A. Shaporenko, A. Terfort, M. Grunze, and M. Zharnikov. "A Detailed Analysis of the Photoemission Spectra of Basic Thioaromatic Monolayers on Noble Metal Substrates." *J. Electron Spectrosc. Relat. Phenom.* **151** (2006), 45–51. DOI: `10.1016/j.elspec.2005.10.008` (cit. on p. 54)

[81] P. Cyganik, M. Buck, T. Strunskus, A. Shaporenko, J. D. E. T. Wilton-Ely, M. Zharnikov, and C. Wöll. "Competition as a Design Concept: Polymorphism in Self-Assembled Monolayers of Biphenyl-Based Thiols." *J. Am. Chem. Soc.* **128** (2006), 13868–13878. DOI: `10.1021/ja0640647` (cit. on p. 54)

[82] D. G. Castner, K. Hinds, and D. W. Grainger. "X-ray Photoelectron Spectroscopy Sulfur 2p Study of Organic Thiol and Disulfide Binding Interactions with Gold Surfaces." *Langmuir* **12** (1996), 5083–5086. DOI: `10.1021/la960465w` (cit. on p. 54)

[83] R. Schmidt, E. McNellis, W. Freyer, D. Brete, T. Gießel, C. Gahl, K. Reuter, and M. Weinelt. "Azobenzene-Functionalized Alkanethiols in Self-Assembled Monolayers on Gold." *Appl. Phys. A* **92** (2008), 267–275. DOI: `10.1007/s00339-008-4829-z` (cit. on p. 56)

[84] G. Hähner, C. Wöll, M. Buck, and M. Grunze. "Investigation of Intermediate Steps in the Self-Assembly of n-Alkanethiols on Gold Surfaces by Soft X-ray Spectroscopy." *Langmuir* **9** (1993), 1955–1958. DOI: `10.1021/la00032a005` (cit. on p. 59)

[85] M. Shibuta, N. Hirata, R. Matsu, T. Eguchi, and A. Nakajima. "Charge Separation at the Molecular Monolayer Surface Observation and Control of the Dynamics." *J. Phys. Chem. Lett.* **3** (2012), 981–985. DOI: `10.1021/jz3002579` (cit. on p. 59)

[86] D. Brete, D. Przyrembel, C. Eickhoff, R. Carley, W. Freyer, K. Reuter, C. Gahl, and M. Weinelt. "Mixed Self-Assembled Monolayers of Azobenzene Photoswitches with Trifluoromethyl and Cyano end Groups." *J. Phys.: Condens. Matter* **24** (2012), 394015. DOI: `10.1088/0953-8984/24/39/394015` (cit. on pp. 62, 119)

[87] A. Eisfeld and J. S. Briggs. "The J- and H-Bands of Organic Dye Aggregates." *Chem. Phys.* **324** (2006), 376–384. DOI: `10.1016/j.chemphys.2005.11.015` (cit. on p. 67)

[88] W. M. Haynes, ed. *CRC Handbook of Chemistry and Physics*. 97th. CRC Press, 2016 (cit. on p. 69)

[89] J. Dokić, M. Gothe, J. Wirth, M. V. Peters, J. Schwarz, S. Hecht, and P. Saalfrank. "Quantum Chemical Investigation of Thermal Cis-to-Trans Isomerization of Azobenzene Derivatives: Substituent Effects, Solvent Effects, and Comparison to Experimental Data." *J. Phys. Chem. A* **113** (2009), 6763–6773. DOI: `10.1021/jp9021344` (cit. on pp. 79, 88)

[90] P. P. Birnbaum and D. W. G. Style. "The Photo-Isomerization of some Azobenzene Derivatives." *Trans. Faraday Soc.* **50** (1954), 1192. DOI: `10.1039/tf9545001192` (cit. on pp. 81–83).

[91] G. Gauglitz and S. Hubig. "Chemical Actinometry in the UV by Azobenzene in Concentrated Solution: A Convenient Method." *J. Photochem.* **30** (1985), 121–125. DOI: `10.1016/0047-2670(85)85018-8` (cit. on p. 81).

[92] H. Rau. "Further Evidence for Rotation in the π,π^* and Inversion in the n,π^* Photoisomerization of Azobenzenes." *J. Photochem.* **26** (1984), 221–225. DOI: `10.1016/0047-2670(84)80041-6` (cit. on p. 81).

[93] V. Ladányi, P. Dvořák, J. A. Anshori, Ľ. Vetráková, J. Wirz, and D. Heger. "Azobenzene Photoisomerization Quantum Yields in Methanol Redetermined." *Photochem. Photobiol. Sci.* **16** (2017), 1757–1761. DOI: `10.1039/c7pp00315c` (cit. on p. 81).

[94] P. P. Birnbaum, J. H. Linford, and D. W. G. Style. "The Absorption Spectra of Azobenzene and some Derivatives." *Trans. Faraday Soc.* **49** (1953), 735. DOI: `10.1039/tf9534900735` (cit. on pp. 81–82).

[95] M. Quick, A. L. Dobryakov, M. Gerecke, C. Richter, F. Berndt, I. N. Ioffe, A. A. Granovsky, R. Mahrwald, N. P. Ernsting, and S. A. Kovalenko. "Photoisomerization Dynamics and Pathways of trans- and cis-Azobenzene in Solution from Broadband Femtosecond Spectroscopies and Calculations." *J. Phys. Chem. B* **118** (2014), 8756–8771. DOI: `10.1021/jp504999f` (cit. on pp. 81, 83).

[96] M. Kasha. "Characterization of Electronic Transitions in Complex Molecules." *Discuss. Faraday Soc.* **9** (1950), 14. DOI: `10.1039/df9500900014` (cit. on p. 81).

[97] G. Zimmerman, L.-Y. Chow, and U.-J. Paik. "The Photochemical Isomerization of Azobenzene." *J. Am. Chem. Soc.* **80** (1958), 3528–3531. DOI: `10.1021/ja01547a010` (cit. on p. 83).

[98] M. G. A. Cembran F. Bernardi and L. Gagliardi. "On the Mechanism of the *cis–trans* Isomerization in the Lowest Electronic States of Azobenzene: S_0, S_1, and T_1." *J. Am. Chem. Soc.* **126** (2004), 3234–3243. DOI: `10.1021/ja038327y` (cit. on p. 83).

[99] T. Moldt, D. Przyrembel, M. Schulze, W. Bronsch, L. Boie, D. Brete, C. Gahl, R. Klajn, P. Tegeder, and M. Weinelt. "Differing Isomerization Kinetics of Azobenzene-Functionalized Self-Assembled Monolayers in Ambient Air and in Vacuum." *Langmuir* **32** (2016), 10795–10801. DOI: `10.1021/acs.langmuir.6b01690` (cit. on pp. 85, 91).

[100] D. Przyrembel. Private communication. Fachbereich Physik, Freie Universität Berlin, Germany (cit. on p. 85).

[101] G. Wedler. *Lehrbuch der physikalischen Chemie*. 4th ed. Weinheim: Wiley-VCH, 1997. ISBN: 3-527-29481-3 (cit. on p. 88).

[102] M. Schulze, M. Utecht, T. Moldt, D. Przyrembel, C. Gahl, M. Weinelt, P. Saalfrank, and P. Tegeder. "Nonlinear Optical Response of Photochromic Azobenzene-Functionalized Self-Assembled Monolayers." *Phys. Chem. Chem. Phys.* **17** (2015), 18079–18086. DOI: 10.1039/C5CP03093E (cit. on pp. 89–91)

[103] K. Tamada, H. Akiyama, and T. X. Wei. "Photoisomerization Reaction of Unsymmetrical Azobenzene Disulfide Self-Assembled Monolayers Studied by Surface Plasmon Spectroscopy: Influences of Side Chain Length and Contacting Medium." *Langmuir* **18** (2002), 5239–5246. DOI: 10.1021/la0157667 (cit. on p. 90)

[104] M. James, T. A. Darwish, S. Ciampi, S. O. Sylvester, Z. Zhang, A. Ng, J. J. Gooding, and T. L. Hanley. "Nanoscale Condensation of Water on Self-Assembled Monolayers." *Soft Matter* **7** (2011), 5309–5318. DOI: 10.1039/C1SM05096F (cit. on p. 91)

[105] L. F. N. Ah Qune, H. Akiyama, T. Nagahiro, K. Tamada, and A. T. S. Wee. "Reversible Work Function Changes Induced by Photoisomerization of Asymmetric Azobenzene Dithiol Self-Assembled Monolayers on Gold." *Appl. Phys. Lett.* **93** (2008), 083109. DOI: 10.1063/1.2969468 (cit. on p. 92)

[106] W. Bronsch, T. Moldt, L. Boie, C. Gahl, and M. Weinelt. "Delocalized Versus Localized Excitations in the Photoisomerization of Azobenzene-Functionalized Alkanethiolate SAMs." *J. Phys.: Condens. Matter* **29** (2017), 484002. DOI: 10.1088/1361-648x/aa9309 (cit. on p. 100)

[107] E. Benassi and S. Corni. "Exciton Transfer of Azobenzene Derivatives in Self-Assembled Monolayers." *J. Phys. Chem. C* **117** (2013), 25026–25041. DOI: 10.1021/jp405077w (cit. on p. 101)

[108] M. A. Van Hove, R. J. Koestner, P. C. Stair, J. P. Bibérian, L. L. Kesmodel, I. Bartoš, and G. A. Somorjai. "The Surface Reconstructions of the (100) Crystal Faces of Iridium, Platinum and Gold: I. Experimental Observations and Possible Structural Models." *Surf. Sci.* **103** (1981), 189–217. DOI: 10.1016/0039-6028(81)90107-2 (cit. on p. 105)

[109] F. Schreier. "The Voigt and Complex Error Function: A Comparison of Computational Methods." *J. Quant. Spectrosc. Radiat. Transfer* **48** (1992). Special Issue Conference on Molecular Spectroscopic Databases, 743–762. DOI: 10.1016/0022-4073(92)90139-U (cit. on p. 108)

[110] F. Schreier. "Optimized Implementations of Rational Approximations for the Voigt and Complex Error Function." *J. Quant. Spectrosc. Radiat. Transfer* **112** (2011), 1010–1025. DOI: 10.1016/j.jqsrt.2010.12.010 (cit. on p. 108)

[111] *Igor Technical Notes: #026: The Voigt Profile*. Part of the documentation of the data analysis software *Igor Pro*. WaveMetrics, Inc. Portland, OR USA, 2006 (cit. on pp. 108–109)

[112] D. R. Lide, ed. *CRC Handbook of Chemistry and Physics, Internet Version 2005*. 85th. CRC Press, 2005 (cit. on p. 111)

Publications

1. T. Moldt, D. Brete, D. Przyrembel, S. Das, J. R. Goldman, P. K. Kundu, C. Gahl, R. Klajn, and M. Weinelt. "Tailoring the Properties of Surface-Immobilized Azobenzenes by Monolayer Dilution and Surface Curvature." *Langmuir* **31** (2015), 1048–1057

   I prepared the samples for the UV/vis experiments, performed the UV/vis measurements, participated in the XPS and NEXAFS measurements, analyzed the UV/vis data and wrote most of the paper.

2. M. Schulze, M. Utecht, T. Moldt, D. Przyrembel, C. Gahl, M. Weinelt, P. Saalfrank, and P. Tegeder. "Nonlinear Optical Response of Photochromic Azobenzene-Functionalized Self-Assembled Monolayers." *Phys. Chem. Chem. Phys.* **17** (2015), 18079–18086

   I prepared some of the samples and participated in discussions.

3. C. Cocchi, T. Moldt, C. Gahl, M. Weinelt, and C. Draxl. "Optical Properties of Azobenzene-Functionalized Self-Assembled Monolayers: Intermolecular Coupling and Many-Body Interactions." *J. Chem. Phys.* **145** (2016), 234701

   I provided the experimental data and participated in discussions.

4. T. Moldt, D. Przyrembel, M. Schulze, W. Bronsch, L. Boie, D. Brete, C. Gahl, R. Klajn, P. Tegeder, and M. Weinelt. "Differing Isomerization Kinetics of Azobenzene-Functionalized Self-Assembled Monolayers in Ambient Air and in Vacuum." *Langmuir* **32** (2016), 10795–10801

   I prepared the samples for the UV/vis experiments, performed the UV/vis measurements, participated in the XPS and NEXAFS measurements, analyzed the UV/vis, XPS, and NEXAFS data, and wrote most of the paper.

5. W. Bronsch, T. Moldt, L. Boie, C. Gahl, and M. Weinelt. "Delocalized Versus Localized Excitations in the Photoisomerization of Azobenzene-Functionalized Alkanethiolate SAMs." *J. Phys.: Condens. Matter* **29** (2017), 484002

   I prepared the samples for the UV/vis experiments, designed the setup for UV/vis kinetics measurements on SAMs, performed these measurements, analyzed the data, wrote the respective part of the paper, and participated in discussions.

Selbstständigkeitserklärung

Ich habe alle Hilfsmittel und Hilfen angegeben und versichere auf dieser Grundlage die Arbeit selbstständig verfasst zu haben. Diese Arbeit wurde nicht schon einmal in einem früheren Promotionsverfahren angenommen oder als ungenügend beurteilt.

Thomas Moldt

Berlin, den

Danksagung

Zuallererst möchte ich Martin Weinelt danken. Er hat diese Doktorarbeit möglich gemacht. Ich danke ihm für seine Geduld und Unterstützung. Seine weite Übersicht über das Forschungsfeld sowie sein tiefes physikalisches Verständnis war eine große Hilfe. Zudem danke ich ihm für das Korrekturlesen dieser Dissertation.

Ebenso danke ich Ralph Ernstorfer für sein Interesse und die Begutachtung meiner Arbeit.

Cornelius Gahl danke ich für seine Ratschläge für die Labortätigkeit, für Diskussionen zur Datenauswertung und -Interpretation und dem Korrekturlesen meiner Dissertation. Er hatte jederzeit ein offenes Ohr für physikalische Fragen aller Art. Dies war ein wichtiger Baustein für meine Arbeit.

Meinen Dank möchte ich auch an alle Kollegen richten, die am SAM-Projekt beteiligt waren: Cornelius Gahl, Daniel Brete, Daniel Przyrembel, Wibke Bronsch, Nils Schuth und Larissa Boie. Wir waren ein gutes Team bei Messzeiten am Synchrotron, bei Diskussionen und gemeinsamen Veröffentllichungen. Insbesondere danke ich auch meinem Vorgänger Daniel Brete für die Einarbeitung zu Beginn meiner Arbeit, für die Unterstützung bei der Arbeit im Labor, sowie allgemein technischer Fragen aller Art. Daniel Przyrembel danke ich für die Präparation eines Teils der Proben und für durchgeführte XPS-Messungen. Der Arbeitsgruppe von Rafal Klajn danke ich für die Synthese des Az11-Moleküls.

Außerdem danke ich allen Mitarbeitern der AG Weinelt für ihre Unterstützung und die Kollegialität. Kristof Zielke danke ich für praktische Hilfe bei Problemen des Alltags im Büro und im Labor. Ebenso danke ich Martin Teichmann für die Einführung in die Welt der Skriptsprache Python.

Ganz besonders danke ich auch meiner Familie und meinen Freunden für ihre Geduld und ihre Unterstützung in dieser Zeit.